BIOORTHOGONAL CATALYSTS FOR THE REDUCTION OF ALDEHYDES BY TRANSFER HYDROGENATION

A Dissertation Presented to the Faculty of the Department of Chemistry

University of Houston

In Partial Fulfillment of the Requirements for the Degree Doctor of Philosophy

---

By

Sohini Bose

August 2019

BIOORTHOGONAL CATALYSTS FOR THE REDUCTION OF ALDEHYDES BY TRANSFER HYDROGENATION

Sohini Bose

APPROVED:

Dr. Loi H. Do, Chairman

Dr. Thomas S. Teets

Dr. Melissa L. Zastrow

Dr. Tai-Yen Chen

Dr. Frank Mckeon

Dr. Dan Wells, Dean, College of Natural Sciences and Mathematics

ACKNOWLEDGEMENTS

My acceptance into University of Houston towards earning a doctorate in Chemistry has indeed been an extraordinary learning opportunity. For starters, I'm extremely grateful to Dr. Loi Do for accepting me into his group in Fall 2014 and spending inordinate amounts of time guiding me through out my academic research. There has always been an opportunity to carry out innovative research in the Do group. I'd like to thank all my committee members, Dr. Teets, Dr. Zastrow, Dr. Halasyamani, Dr. Chen, and Dr. McKeon for helping me along the way. I am grateful to Dr. Teets and Dr. Chen for allowing me use their instruments.

I'd like to thank all the members of my group, both past, and present, as we have consistently worked as a team to help each other realize our goals as graduate students. Working in the lab and carrying out rational research wouldn't have been possible without the constant consultation with Do group members. Dr. Lu Yang, a former member of Do group, deserves a special mention for introducing me to cell culture. I would like to thank Dr. Alloysius Budi Utama from Rice University, who is a wonderful trainer of confocal microscope and has always provided with insightful suggestions. Finally, Dr. Siheng Li, a former member of Dr. Chengzhi Cai's group in University of Houston and Dr. Qi Fu, Assistant Professor in Department of Earth and Atmospheric Sciences in University of Houston, without whose support it was absolutely not possible to reach my research goal.

I would like to mention about all the amazing group members of Dr. Teets and Dr. Chen for always being so cooperative, especially Guangjie Yan from Dr. Chen's lab for spending enormous hours to help me get good images. I'd like to thank Dr. Mehmet

Sen from Department of Biology and Biochemistry in University of Houston for opening his cell culture lab doors to us when we needed it the most.

BIOORTHOGONAL CATALYSTS FOR THE REDUCTION OF ALDEHYDES BY TRANSFER HYDROGENATION

An Abstract of a Dissertation Presented to the Faculty of the Department of Chemistry University of Houston

---

In Partial Fulfillment of the Requirements for the Degree Doctor of Philosophy

---

By

Sohini Bose

August 2019

ABSTRACT

Bioorthogonal reactions catalyzed by inorganic complexes have useful applications in biology and medicine. These reactions could be used to mediate bioconjugations of fluorescent dyes to proteins, convert non-toxic precursor molecules to biologically active compounds, or neutralize chemical toxins to non-hazardous substances. Because of the heterogeneous nature of biological environments, developing catalysts that can operate inside living cells is challenging.

To expand the biocompatible reaction toolbox, we investigated intracellular transfer hydrogenation reactions catalyzed by organometallic iridium catalysts. Formation of hydrogenation products in cells was visualized by fluorescence microscopy using a fluorogenic bodipy substrate. No fluorescence was observed in cells that were not treated with iridium catalyst. We propose that the reduced cofactor nicotinamide adenine dinucleotide (NADH) is a possible hydride source inside the cell based on studies using pyruvate as a cellular redox modulator. To quantify the transfer hydrogenation efficiency in cells, we used liquid chromatography-mass spectrometry to measure the yield of alcohol products generated in live cell experiments. Differences in the intracellular activity of the catalysts were explained by the differences in their toxicity and cellular uptake. Additionally, we have synthesized a series of fluorogenic iridium catalysts to study the spatial distribution of the catalysts inside cells.

We also describe our efforts to prepare biocompatible transfer hydrogenation catalysts based on cobalt rather than iridium. Finally, we also present our work on developing off-on fluorescent probes to quantify transfer hydrogenation reactions in live cells. Some of the challenges that we encountered include poor substrate reactivity even

in the reaction flask, poor cellular uptake and cell retention of the substrate and the product.

This work is the first ever example of aldehyde reduction by iridium catalysts in live cells. We also showed that poor efficiency of iridium catalysts in live cells is related to their toxicity and cellular uptake. The detailed study on catalyst activity in live cells will help researchers modifying the ligands accordingly to achieve higher intracellular efficiency. This new type of bioorthogonal chemistry could be used as a new therapeutic tool in future to treat aldehyde toxicity.

TABLE OF CONTENTS

LIST OF ABBREVIATIONS

A	absorbance
CTCF	total corrected cell fluorescence
d	doublet
DCM	dichloromethane
DIC	differential interference contrast
DMEM	Dulbecco's modified eagle medium
DMF	dimethyl formamide
DMSO	dimethylsulfoxide
FBS	fetal bovine serum
GC-FID	gas chromatography-flame ionization detector
GC-MS	gas chromatography-mass spectroscopy
HEPES	(4-(2-hydroxyethyl)-1-piperazineethanesulfonic acid)
HRMS	high resolution mass spectroscopy
IC50	half maximal inhibitory concentration
ICP-MS	inductive coupled plasma-mass spectroscopy
IR	infrared (spectroscopy)
J	coupling constant
LC-ESI-MS	liquid chromatography-electrospray ionization-mass spectroscopy
m	multiplate or mili
MTS	3-(4,5-dimethylthiazol-2-yl)-5-(3-carboxymethoxyphenyl)-2-(4-sulfophenyl)-2H-Tetrazolium
m/z	mass to charge ratio

NADH	reduced cofactor nicotinamide adenine dinucleotide
NAD(P)H	phosphorylated analogue of NADH
NMR	nuclear magnetic resonance (spectroscopy)
PCC	Pearson's correlation coefficient
PEG	polyethylene glycol
Ph	phenyl
Py	pyridine
RCM	ring closing metathesis
ROMP	ring opening metathesis polymerization
RT	room temperature
s	singlet
t	triplet
td	triplet of doublet
THF	tetrahydrofuran
TON	turn over number
UV-Vis	ultraviolet-visible (spectroscopy)
λ_{ex}	excitation wavelength
λ_{em}	emission wavelength
μ	micro

CHAPTER 1. Bioorthogonal Organometallic Chemistry

Portions of this work have been previously published.

Reproduced with permission from Ngo, A. H.; Bose, S.; Do, L. H. *Chem.–Eur. J.*, **2018**, *24*, 10584-10594. DOI: 10.1002/chem.201800504. *(Ngo and Bose contributed equally).*

1.1. Introduction to Bioorthogonal Reactions

Bioorthogonal reactions are chemical transformations that occur in the presence of biological components using synthetic agents. Tools that enable selective chemical reactions inside cells could be useful for elucidating biological processes or engineering novel interactions. Bertozzi's landmark work in the early 2000s demonstrated that synthetic chemistry and biological chemistry could take place within the same physical space, and yet do not interfere with each other.[1,2] These bioorthogonal reactions could also be catalyzed by light[3-5] or transition metals. Organometallic catalysts have been used to carry out a variety of bioorthogonal reactions, including deprotection of alloc/allyl-protected substrates[6], olefin metathesis,[7] C–C bond cross coupling,[8] azide-alkyne cycloaddition,[9] and transfer hydrogenation.[10]

These bioorganometallic reactions could be promoted by homogeneous or heterogeneous metal catalysts. For example, deprotection of allylcarbamate groups in human cell was first reported by Streu and Meggers by a homogeneous ruthenium catalyst in 2006.[6a] Similar in-cellulo allylcarbamate bond cleavage reaction was carried out by Bradley and coworkers in 2011 using Pd^0 nanoparticles trapped within polystyrene microspheres.[11] This Pd^0 heterogeneous catalyst can enter cells and mediate chemical reactions without affecting cell viability. Pd^0 nanoparticles have also been employed in zebrafish for selective activation of the prodrug 5-fluorouracil, the inactive form of an anti-cancer drug.[12] Unlike conventional prodrugs, which relies on metabolic activation,[13] selective cleavage can be achieved only when the Pd^0 catalysts is present. Both heterogeneous and homogeneous Pd catalysts have been shown to catalyze Suzuki-Miyara cross coupling reaction in cell.[12] For example, the homogeneous Palladium(II)

compound $[Pd(OAc)_2(ADHP)_2]$ (ADHP = 2-amino-4,6-dihydroxypyrimidine), was used to label iodophenyl modified proteins on cell surfaces with fluorescent tags bearing boronic acid groups in *E. coli*[14-16] (Scheme 1).

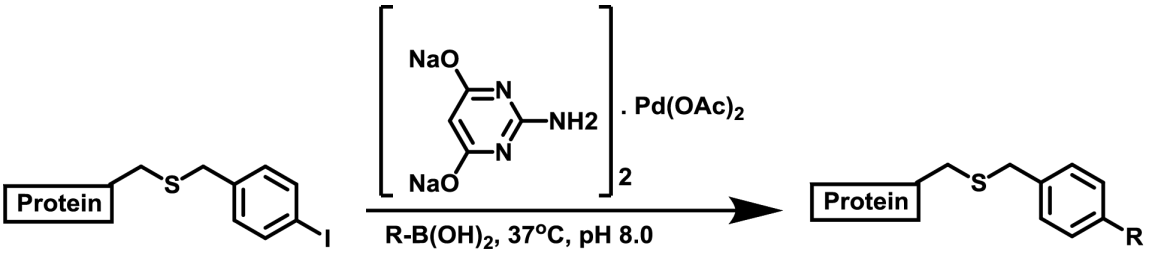

Scheme 1. Suzuki-Miyara coupling reaction catalyzed by homogeneous Pd(II) catalyst in *E. coli* cells.

1.2. Challenges in Designing Biocompatible Catalysts

An ideal catalyst should be inexpensive, easy to use, and promote reactions that are fast, efficient, and selective. To minimize waste, it should also be recyclable. To apply these catalysts inside living systems, additional parameters must also be considered relating to their biocompatibility. For example, catalysts must also be non-toxic, air/water stable, tolerant of biological nucleophiles, have good cellular retention, and are active under physiological conditions. Unlike metalloenzymes, small molecule homogeneous metal complexes do not have protein matrices to provide substrate specificity or prevent catalyst poisoning. Satisfying these stringent criteria make designing biocompatible metal catalysts exceedingly challenging.

Because synthetic catalysts could be chemically modified, their characteristics such as, cytotoxicity, biodistribution, and lifetime are tunable. For example, studies have

shown that the 50% growth inhibition concentrations (IC_{50}) of some inorganic compounds in mammalian cells can be greater than 500 μM[17] and tends to correlate with lipophilicity.[18] Interestingly, it has been demonstrated that modification of a metal complex's ligand periphery could significantly improve both its biocompatibility and catalytic performance.[9a] To direct metal catalysts to specific biological organs or cellular compartments, a variety of established targeting strategies could be used.[19]

1.3. Examples of Systematic Optimization of Biocompatible Catalysts

Copper catalyzed azide-alkyne cycloaddition (CuAAC) is one of the most extensively studied bioorthogonal reactions. In 2002, the research groups of Fokin/Sharpless[20] and Meldal[21] independently reported on the regioselective synthesis of 1,4-disubstituted triazoles from organic azides and alkynes using copper(I) catalysts. This discovery had a profound influence in many areas of scientific research, including chemical synthesis, drug development, and materials science.[22] Just a year after its report, CuAAC was used successfully to label the surfaces of intact bacterial cells[4b] and to profile enzyme activities in whole proteosomes.[9c] In 2005, Tirrell and coworkers were able to track the synthesis of a model protein barstar containing unnatural alkynyl amino acids in auxotrophic *E. coli* by tagging it with coumarin azides using a CuAAC ligation method (Scheme 2).[9d] This was the first example of applying CuAAC reaction in live cell. Similarly, Schultz and coworker selectively incorporated propargyloxyphenylalanine into intracellular proteins and used CuAAC to conjugate them with dansyl or fluorescein azide probes.[9e] A drawback of using these copper catalysts is that copper is toxic to living

systems. However, it was found that the cytotoxic effects of copper ions could be mitigated by chelating them using multidentate supporting ligands.

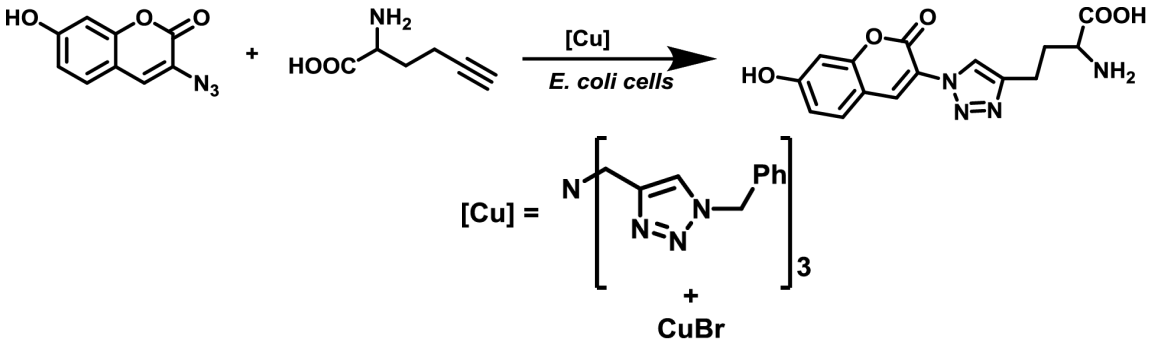

Scheme 2. Early example of CuAAC reaction in live cells by Tirrell and coworkers.

In 2007, Wong and coworkers demonstrated that fucose and sialic acid analogs containing terminal alkynes could be fused with cellular glycans using copper tris(triazole)amine (ligand **1**, Chart 1) as the CuAAC catalyst.[23] Because aberrant glycosylation has been closely linked to cancer, this work may have important implications for the identification of glycan-related biomarkers and targets for therapeutic intervention. A drawback of this work, however, was that the CuAAC reaction had to be performed on fixed rather than live cells due to copper toxicity. In 2010, a significant advance was made by Wu and coworkers in the development of more biocompatible copper complexes.[9a] After screening a library of 14 tris(triazole)amine ligand derivatives, they identified a bulky sulfonated variant (ligand **2**, Chart 1) that, when ligated to copper, achieved the ideal balance between reactivity and solubility. Using this Cu/**2** catalyst, the Wu group was able to fluorescently label alkyne-bearing guanosine diphosphate (GDP)-

fucose inside zebrafish embryos. Remarkably, the emissive fucosylated glycans in the enveloping layer of zebrafish could be visualized in real time by confocal microscopy.

In another study, Zhao/Wu/Chen and coworkers showed that a biocompatible copper complex similar to Cu/**2** allowed the intracellular conjugation of an environment-sensitive fluorophore to an acid-stress chaperone protein called HdeA.[24] This HdeA-probe hybrid enabled pH measurements in both the periplasm and cytoplasm of *E. coli* without any apparent cytotoxicity. Application of ligand **2** lowered the cytotoxic effect of copper ion. In 2012, Ting and coworkers showed that azide substrate chelation enhanced cell labeling efficiency by as much as 25-fold compared to CuAAC reactions performed using conventional non-chelating substrates[25] and also allowed relatively low concentrations (10-100 μM) of copper to be used for intracellular studies.

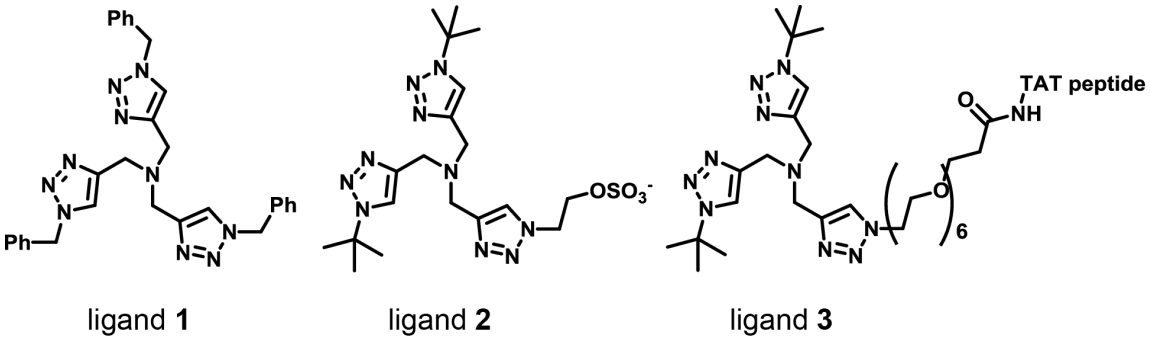

Chart 1. Evolution of tris(triazole)amine ligands used in CuAAC reactions.

Most recently, in 2017, Cai and coworkers reported a method using mass spectrometry to quantify the product yields in biological CuAAC reactions.[9f] This capability allowed them to compare the catalytic efficiencies between a variety of copper complexes. The Cai group found that modification of the tris(triazole)amine ligand with a

cell-penetrating peptide (ligand **3**, Chart 1) increased its uptake in human OVCAR5 cancer cells by up to ~15-fold compared to that using conventional ligands. Using 163 μM copper and 1.3 μM of azide concentration in cell, around 18% and 0.8% of product were formed on the cell membrane and in the cytosol, respectively. About 75% of the cells remained viable after 10 min of reaction. Upon reducing the biothiol concentration by treating cells with *N*-ethylmlemide, the reaction yield in the cytosol was increased upto 14%, whereas no change was observed in the reaction yield on the membrane. These results suggest that biothiol deactivation of copper catalyst in one of the major reasons for lower intracellular efficiency (~ 0.8% yield) of CuAAC reactions.

1.4. Applications of Small Molecule Biocompatible Metal Complexes

Although, recent advances in medicine have improved the quality of life for people everywhere, we still do not have solutions for many health-related challenges. For example, the ten-year survival rates for cancers of the brain, lung, or pancreas are estimated to be less than 15%.[26] Also, there is no cure for diseases like Alzheimer's[27] or Parkinson's diseases,[28] only treatment for some of their associated symptoms. Many drugs available in the market can have severe side effects or become ineffective due to drug resistance.[29] For example, although the platinum anticancer complex cisplatin [$PtCl_2(NH_3)_2$] is used in the treatment of more than 50% of chemotherapeutic treatments,[30,31] it can cause nephrotoxicity, ototoxicity, low blood counts etc.

To discover new types of drugs, recent research has focused on metal catalysts. Metal catalysts are attractive as new therapeutic agents because they could be used to alter metabolic pathways or induce other physiological change that would prevent

disease, they could be administered in lower doses because of their catalytic turn over abilities, and they might be able to combat drug resistance through novel mechanism of action. Ruthenium,[32] iridium,[33] and osmium[34] complexes have attracted attention for their anti-cancer activity in recent years. These complexes can selectively kill cancer cells by altering their redox balance.[35]

1.5. Future of Small Molecule Metal Complex Catalyzed Bioorthogonal Reactions

A promising area for bioorthogonal reaction development is olefin metathesis, a transformation that involves the cleavage of C-C double bonds followed by reassembly to generate products with new C-C double bonds.[36] Olefin metathesis reactions include cross metathesis, ring-opening metathesis polymerization (ROMP), and ring-closing metathesis (RCM). Many creative applications of olefin metathesis have been pursued in chemical biology,[37] such as its use in the synthesis of cyclic peptides, construction of polysaccharide mimics, or site selective modification of protein residues. These achievements were made possible by metal catalysts that are tolerant of strong sigma donors such as amines and thiols and have good water solubility. For example, Grubbs and coworkers reported in 2006 that the installation of polyethylene glycol (PEG) chains to a carbene ligand provided ruthenium complexes that are highly active for cross-metathesis in water at 45°C.[38] Further catalyst improvements made by Davis and coworkers led to ruthenium complexes that could be used in open air and were not inhibited by thioether functionalities[39] (Scheme 3). To the best of our knowledge, the study of Ru complexes for intracellular metathesis reactions have not yet been reported.

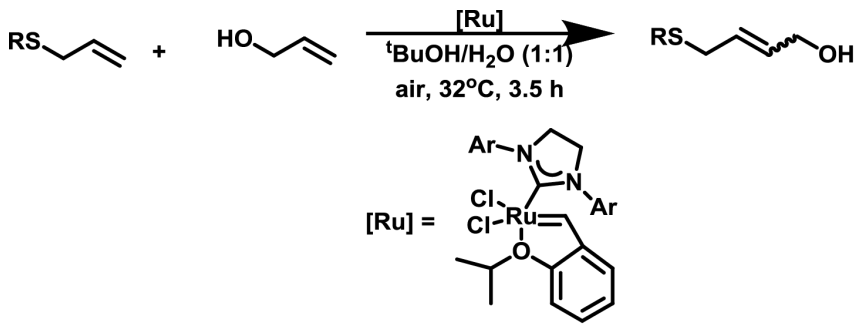

Scheme 3. Olefin metathesis reaction in air catalyzed by ruthenium complex.

Another useful organometallic reaction that is being explored in chemical biology is carbene transfer.[40,41] This reaction entails first the generation of metal-carbene species by reacting diazoester compounds with various metal precursors, followed by insertion of the carbene into olefins (cyclopropanation) or heteroatom-hydrogen bonds (X-H insertion, where X = C, O, B, Si, etc.) (Scheme 4). Balskus and coworker successfully demonstrated the application of cyclopropanation catalysts with living microorganisms in 2015 (Scheme 5).[42] They found that ferric phthalocyanine complexes promote efficiently carbene transfer to styrene in the presence of *E. coli*. Because the microbes were engineered to produce styrene directly from D-glucose, this example was the first to show that non-biological carbene-transfer reactivity could be coupled to cellular metabolism for small molecule production. The use of designer micelles was later reported to accelerate styrene accumulation by *E. coli* and enhance catalytic efficiency.[43] These reactions were determined to occur extracellularly. On the basis of these findings, however, it seems likely that biocompatible small molecule catalysts for carbene transfer reactions are well within our reach.

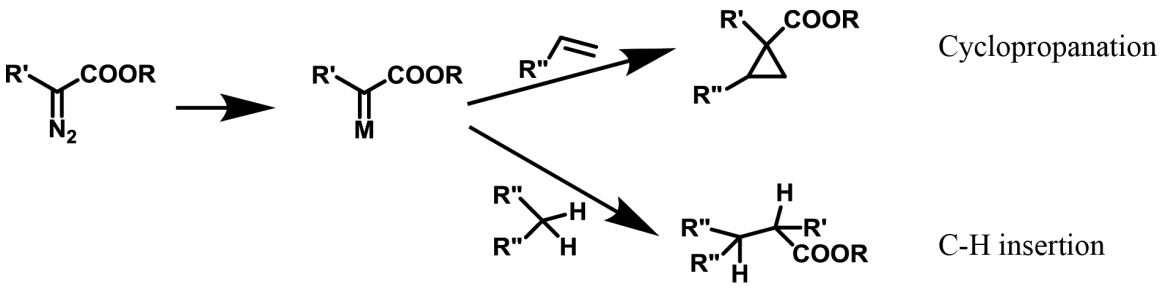

Scheme 4. Schematic display of carbene transfer reaction.

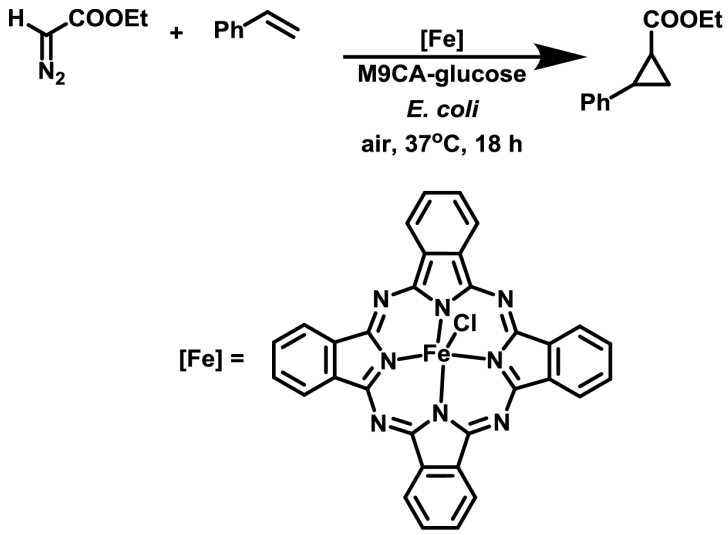

Scheme 5. Example of carbene transfer reaction in presence of growth media and *E. coli*. Cells.

Hydrofunctionalization catalysis is another potential area for future bioorthogonal reaction development (Scheme 6).[44,45] The functionalization of alkenes or alkynes by E-Nuc species (E = H, BR_2, etc.; Nuc = halogen, CN, CHO, OH, CO, COOR, NR_2, etc.) is a popular method used in organic synthesis and industrial processes. In many cases, there

are transition metal catalysts that could provide either the Markovnikov (Nuc adds to more substituted carbon) or anti-Markovnikov (Nuc adds to less substituted carbon) regioisomer starting from unsymmetrical alkenes/alkynes. Despite the extensive amount of research devoted to hydrofunctionalization chemistry (i.e. hydroamination, hydroalkoxylation, hydration, etc.), the adaptation of such processes for *in-vivo* catalysis has been largely unexplored. Campagne/Prim and coworkers used iron(III) chloride salts to promote the intermolecular hydroamination of styrene derivatives using *p*-toluenesulfonamide in 1,4-dioxane at room temperature (Scheme 7).[46] This reaction is notable because iron(III) is air stable and a biologically compatible metal ion. Although this reaction uses organic solvent, which prohibits this reaction to be carried out in living environments, we expect that they could be overcome through reaction optimization and/or catalyst modifications.

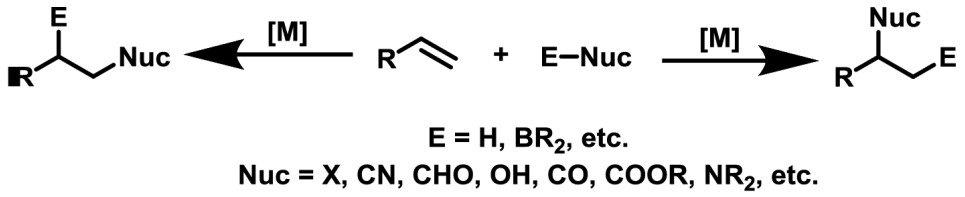

Scheme 6. Hydrofunctionalization reactions resulting in Markovnikov or anti-Markovnikov products.

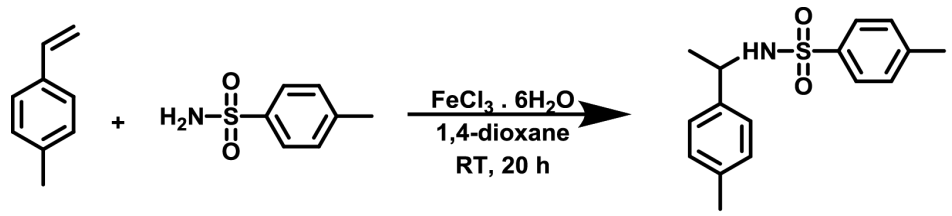

Scheme 7. Iron(III) catalyzed hydroamination of styrene derivative in 1,4-dioxane at RT.

In the following chapters, we will describe our work on developing biocompatible transfer hydrogenation reactions using organometallic complexes. Chapter two will demonstrate that the conversion of aldehydes to alcohols can be achieved using unprotected iridium transfer hydrogenation catalysts inside living cells. The reactions were observed in real time by confocal fluorescence microscopy using a Bodipy fluorogenic substrate. We proposed that the reduced cofactor nicotinamide adenine dinucleotide (NADH) is a possible hydride source inside the cell based on studies using pyruvate as a cellular redox modulator. We expected that this biocompatible reductive chemistry would be broadly useful to practitioners working at the interface of chemistry and the life sciences.

In Chapter three, a series of fluorogenic iridium (III) transfer hydrogenation catalysts were synthesized to be used for cell tracking experiments. These new catalyst-probe conjugates show similar catalytic activity as their parent iridium complexes in reducing aldehyde to alcohol. Detailed comparative studies were performed to assess what parameters are important to their intracellular activity. The intracellular catalytic activity of these new catalyst-probe conjugates and their parent catalysts were studied by quantifying their reaction products in cell lysate using liquid chromatography coupled

with high-resolution mass spectrometry (LC-ESI-MS). The cellular uptake of the catalysts was also determined to calculate their activity. The difference in in-cellulo catalytic activities of these catalysts was explained in terms of their cytotoxicity and cellular uptake.

Because iridium is an “unnatural” metal and is expensive, attempts were made to develop transfer hydrogenation catalysts based on biological metals. Chapter four describes the design of inexpensive, earth abundant, and more biocompatible transfer hydrogenation catalysts using cobalt(III). Unfortunately, the Co(III) complexes were not stable in aqueous solutions. Possible modification of the ligand moiety will be discussed on how to stabilize the Co metal. The evaluation of a fluorogenic probe for real time monitoring of transfer hydrogenation reactions in living system is also described.

1.6. References

1. Saxon, E.; Bertozzi, C. R. *Science* **2000**, *287*, 2007-2010.
2. Agard, N. J.; Prescher, J.; Bertozzi, C. R. *J. Am. Chem. Soc.* **2004**, *126*, 15046-15047.
3. Lim, R. K.; Lin, Q. *Acc. Chem. Res.* **2011**, *44*, 828-839.
4. Klán, P.; Šolomek, T.; Bochet, C. G.; Blanc, A.; Givens, R.; Rubina, M.; Popik, V.; Kostikov, A.; Wirz, J. *Chem. Rev*. **2013**, *113*, 119-191.
5. Sánchez, M. I.; Martínez-Costas, J.; Gonzalez, F.; Bermudez, M. A.; Vázquez, M. E.; Mascareñas, J. L. *ACS Chem. Biol*. **2012**, *7*, 1276-1280.
6. a) Streu, C.; Meggers, E. *Angew. Chem. Int. Ed.* **2006**, *45*, 5645-5648. b) Völker, T., Dempwolff, F., Graumann, P. L.; Meggers, E. *Angew. Chem. Int. Ed.* **2014**, *53*, 10536-10540. c) Ritter, C.; Nett, N.; Acevedo-Rocha, C. G.; Lonsdale, R.; Kraling, K.; Dempwolff, F.; Hoebenreich, S.; Graumann, P. L.; Reetz, M. T.; Meggers, E. *Angew. Chem., Int. Ed.* **2015**, *54*, 13440-13443. d) Tomás-Gamasa, M., Martínez-Calvo, M., Couceiro, J. R.; Mascareñas, J. L. *Nat. Commun.* **2016**, *7*, 12538. e) Hsu, H.-T., Trantow, B. M., Waymouth, R. M.; Wender, P. A. *Bioconjugate Chem.* **2016**, *27*, 376-382.
7. Jeschek, M.; Reuter, R.; Heinisch, T.; Trindler, C.; Klehr, J.; Panke, S.; Ward, T. R. *Nature* **2016**, *537*, 661-665.
8. a) Li, N.; Lim, R. K. V.; Edwardraja, S.; Lin, Q. *J. Am. Chem. Soc.* **2011**, *133*, 15316-15319. b) Chalker, J. M.; Wood, C. S. C.; Davis, B. G. *J. Am. Chem. Soc.* **2009**, *131*, 16346-16347. c) Spicer, C. D.; Triemer, T.; Davis, B. G. *J. Am. Chem. Soc.* **2011**, *134,* 800-803. d) Davis, L.; Chin, J. W. *Nat. Rev. Mol. Cell. Biol.* **2012**, *13,* 168-182.
9. a) Soriano del Amo, D.; Wang, W.; Jiang, H.; Besanceney, C.; Yan, A. C.; Levy, M.; Liu, Y.; Marlow, F. L.; Wu, P. *J. Am. Chem. Soc.* **2010**, *132*, 16893-16899. b) Link, A. J.; Tirrell, D. A. *J. Am. Chem. Soc.* **2003**, *125*, 11164-11165. c) Speers, A. E.; Adam, G. C.; Cravatt, B. F. *J. Am. Chem. Soc.* **2003**, *125*, 4686-4687. d) Beatty, K. E.; Xie, F.; Wang, Q.; Tirrell, D. A. *J. Am. Chem. Soc.* **2005**, *127*, 14150-14151. e) Deiters, A.; Schultz, P. G. *Bioorg. Med. Chem. Lett.* **2005**, *15*, 1521-1524. f) Li, S.; Wang, L.; Yu, F.; Zhu, Z.; Shobaki, D.; Chen, H.; Wang, M.; Wang, J.; Qin, G.; Erasquin, U. J.; Ren, L.; Wang, Y.; Cai, C. *Chem. Sci.* **2017**, *8*, 2107-2114.
10. a) Bose, S.; Ngo, A. H.; Do, L. H. *J. Am. Chem. Soc.* **2017**, *139*, 8792-8795. b) Zhao, J.; Rebelein, J. G.; Mallin, H.; Trindler, C.; Pellizzoni, M. M.; Ward, T. R. *J. Am. Chem. Soc.* **2018**, *140*, 13171-13175.

11. Yusop, R. M.; Unciti-Broceta, A.; Johansson, E. M. V.; Sa´nchez-Martı´n, R. M.; Bradley, M. *Nat. Chem.* **2011**, *3*, 239-243.

12. Unciti-Broceta, A.; Johansson, E. M. V.; Yusop, R. M.; Sa´nchez-Martı´n, R. M.; Bradley, M. *Nat. Protoc.* **2012**, *7*, 1207-1218.

13. Rautio, J.; Kumpulainen, H.; Heimbach, T.; Oliyai, R.; Oh, D.; Järvinen, T.; Savolainen, J. *Nat. Rev. Drug Discov*. **2008**, *7*, 255-270.

14. Chalker, J. M.; Wood, C. S. C.; Davis, B. G. *J. Am. Chem. Soc.* **2009**, *131*, 16346-16347.

15. Spicer, C. D.; Triemer, T.; Davis, B. G. *J. Am. Chem. Soc.* **2011**, *134*, 800-803.

16. Davis, L.; Chin, J. W. *Nat. Rev. Mol. Cell Biol.* **2012**, *13*, 168-182.

17. Yang, L.; Bose, S.; Ngo, A. H.; Do, L. H. *ChemMedChem* **2017**, *12*, 292-299.

18. Liu, Z.; Sadler, P. J. *Acc. Chem. Res.* **2014**, *47*, 1174-1185.

19. Qiu, K.; Chen, Y.; Rees, T. W.; Ji, L.; Chao, H. *Coord. Chem. Rev.* **2019**, *378*, 66-86.

20. Rostovtsev, V. V.; Green, L. G.; Fokin, V. V.; Sharpless, K. B. *Angew. Chem. Int. Ed.* **2002**, *41*, 2596-2599.

21. Tornøe, C. W.; Christensen, C.; Meldal, M. *J. Org. Chem.* **2002**, *67*, 3057-3064.

22. Meldal, M.; Tornøe, C. W. *Chem. Rev.* **2008**, *108*, 2952-3015.

23. Hsu, T.-L.; Hanson, S. R.; Kishikawa, K.; Wang, S.-K.; Sawa, M.; Wong, C.-H. *Proc. Natl. Acad. Sci. U.S.A.* **2007**, *104*, 2614-2619.

24. Yang, M.; Jalloh, A. S.; Wei, W.; Zhao, J.; Wu, P.; Chen, P. R. *Nature Commun.* **2014**, *5*, 4981.

25. Uttamapinant, C.; Tangpeerachaikul, A.; Grecian, S.; Clarke, S.; Singh, U.; Slade, P.; Gee, K. R.; Ting, A. Y. *Angew. Chem. Int. Ed.* **2012**, *51*, 5852-5856.

26. Cancer Research UK: Statistics by Cancer Type. https://www.cancerresearchuk.org/health-professional/cancer-statistics/statistics-by-cancer-type (accessed May 31st, 2019).

27. Hung, S.-Y.; Fu, W.-M. *J. Biomed. Sci*. **2017**, *24*, 47-47.

28. Kiser, A. V.; Pronovost, P. J. *JAMA* **2009**, *301*, 1708–1709.

29. Avendaño, C.; Menéndez, J. C. Medicinal Chemistry of Anticancer Drugs; Elsevier: Amsterdam, The Netherlands, **2008**.

30. Mjos, K. D.; Orvig, C. *Chem. Rev*. **2014**, *114*, 4540-4563.

31. Florea, A.-M.; Büsselberg, D. *Cancers* **2011**, *3*, 1351-1371.

32. a) Ward, T. R. *Acc. Chem. Res*. **2011**, *44*, 47-57. b) Dougan, S. J.; Habtemariam, A.; McHale, S. E.; Parsons, S.; Sadler, P. J. *Proc. Natl Acad. Sci. USA* **2008**, *105*, 11628-11633. c) Soldevila-Barreda, J. J.; Romero-Canelón, I.; Habtemariam, A.; Sadler, P. J. *Nat. Commun*. **2015**, *6*, 6582.

33. Liu, Z.; Romero-Canelon, I.; Qamar, B.; Hearn, J. M.; Habtemariam, A.; Barry, N. P. E.; Pizarro, A. M.; Clarkson, G. J.; Sadler, P. J. *Angew. Chem. Int. Ed.* **2014**, *53*, 3941-3946.

34. Fu, Y.; Romero, M. J.; Habtemariam, A.; Snowden, M. E.; Song, L.; Clarkson, G. J.; Qamar, B.; Pizarro, A. M.; Unwin, P. R.; Sadler, P. J *Chem. Sci.* **2012**, *3*, 2485-2494.

35. Sasmal, P. K.; Streu, C. N.; Meggers, E. *Chem. Commun.* **2013**, *49*, 1581-1587.

36. Astruc, D. *New J. Chem.* **2005**, *29*, 42-56.

37. Binder, J. B.; Raines, R. T. *Curr. Opin. Chem. Biol.* **2008**, *12*, 767-773.

38. Hong, S. H.; Grubbs, R. H. *J. Am. Chem. Soc.* **2006**, *128*, 3508-3509.

39. Lin, Y. A.; Chalker, J. M.; Floyd, N.; Bernardes, G. J. L.; Davis, B. G. *J. Am. Chem. Soc.* **2008**, *130*, 9642-9643.

40. Deng, Y.; Qiu, H.; Srinivas, H. D.; Doyle, M. P. *Current Organic Chemistry* **2016**, *20*, 61-81.

41. Zhang, X. P.; Cui, X. *Comprehensive Organic Synthesis* **2014**, *7*, 86-120.

42. Wallace, S.; Balskus, E. P. *Angew. Chem. Int. Ed.* **2015**, *54*, 7106-7109.

43. Wallace, S.; Balskus, E. P. *Angew. Chem. Int. Ed.* **2016**, *55*, 6023-6027.

44. Beller, M.; Seayad, J.; Tillack, A.; Jiao, H. *Angew. Chem. Int. Ed.* **2004**, *43*, 3368-3398.

45. Crossley, S. W. M.; Obradors, C.; Martinez, R. M.; Shenvi, R. A. *Chem. Rev.* **2016**, *116*, 8912-9000.

46. Zotto, C. D.; Michaux, J.; Zarate-Ruiz, A.; Gayon, E.; Virieux, D.; Campagne, J.-M.; Terrasson, V.; Pieters, G.; Gaucher, A.; Prim, D. *J. Organomet. Chem.* **2011**, *696*, 296-304.

CHAPTER 2. Intracellular Transfer Hydrogenation Mediated By Unprotected Organoiridium Complexes

This work has been previously published.

Reproduced with permission from Bose, S.; Ngo, A. H.; Do, L. H. *J. Am. Chem. Soc.*, **2017**, *139*, 8792-8795. DOI: 10.1021/jacs.7b03872.

2.1. Introduction

Transfer hydrogenation catalysis is a process in which a hydride is transferred from a donor to an acceptor and has been studied for several decades.[1,2] Iridium, ruthenium[3] and rhodium[4-6] small molecule complexes have been shown to be active homogeneous transfer hydrogenation catalysts in aqueous media. $Ir(Cp^*)(H_2O)_3^{2+}$ (pentamethylcyclopentadienyl) was reported to catalyze reduction of aldehyde and ketone in acidic water in 1999 by Ogo/Watanabe and coworkers.[7] Xiao and coworkers found that that transfer hydrogenation could be carried out in neutral pH by Ir(Cp*)(Ts-en)(Cl) (Ts-en = *N*-(*p*-tosyl)ethylenediamine) (**IrTs(en)**) in 2006.[8] These Rh, Ru and Ir complexes have also been known to transfer hydride to/from nicotinamide adenine dinucleotide (NAD^+ = oxidized form, NADH = reduced form), which is a biological cofactor present in all living systems. Given the importance of NAD^+/NADH, transfer hydrogenation catalysts that can utilize this cofactor are expected to influence the cellular redox balance.

In 1988, Steckhan and coworkers showed that $Rh(Cp^*)(2, 2'\text{-bipyridine})(H_2O)_2^+$ can transfer hydride from formate to NAD^+ in 1,4-regioselective manner to yield NADH in aqueous media.[9] In 2012, Sadler and coworkers[10] and Fukuzumi and coworkers[11] showed that Ir and Ru complexes can transfer hydride from NADH to proton to yield NAD^+ and hydrogen gas in aqueous media. Iridium complexes can also transfer hydride from NADH to dioxygen forming reactive oxygen species in aqueous media.[12] Do and coworkers showed that hydride can be transferred from NADH to organic electrophiles, thereby reducing organic molecule under physiological condition.[13] Organometallic Ru,[10,14] Rh,[5] and Ir[11,15,16] complexes are substitutionally inert and thus, are attractive as

biofriendly catalysts due to their water and air stability. They have been employed in diverse applications ranging from enzyme cascade processes[17-19] to protein functionalization,[20] and fluorescent detection.[21] Herein, it has been demonstrated for the first time that unprotected organoiridium complexes can catalyze the reduction of aldehyde to alcohol by Ir(III) catalyst in living cells using intracellular NADH.

Prior to this work, Sadler and coworkers[22] showed that iridium complexes can catalyze oxygen reduction in living cells and Komatsu/Ariga and coworkers reported that Ir(Cp*)(1,10-phenanthroline)$(H_2O)^+$ complexes could be used in living cells to catalyze the reduction of fluorescein-quinone conjugate using NAD(P)H (NADPH is the phosphorylated analogue of NADH).[23] To the best of our knowledge, the reduction of carbonyl compound by Ir(III) catalysts in living cells was not described previously in the literature. The work in this chapter will take advantage of fluorescence microscopy to study reactions in cell because it is a sensitive and non-invasive technique.

2.2. Results and Discussion

2.2.1. *Ex-vivo* Transfer Hydrogenation Reactions

Pentamethylcyclopentadienyl iridium complexes that are ligated by N-phenyl-2-pyridinecarboxamidate (**Ir1**) shows very high activity in reducing aldehyde to alcohol compared to pentamethylcyclopentadienyl iridium complexes that are ligated by 2,2'-bipyridine (**Ir2**) and its derivatives under physiological conditions.[13] **Ir1** also shows similar activity to that of the commonly studied **IrTs(en)** (Figure 1). Because of the favorable catalytic activity of **Ir1**, all subsequent experiments have been carried out using this complex. **Ir3** is a precursor for the synthesis of all of the iridium catalysts described

here.

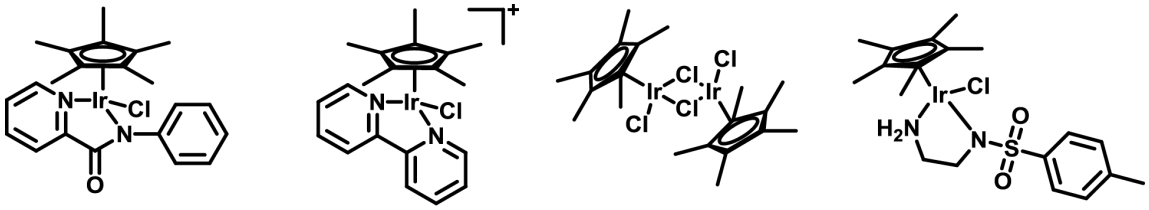

Ir1 **Ir2** **Ir3** **IrTs(en)**

Chart 1. Structures of **Ir1**, **Ir2**, **Ir3** and **IrTs(en)**

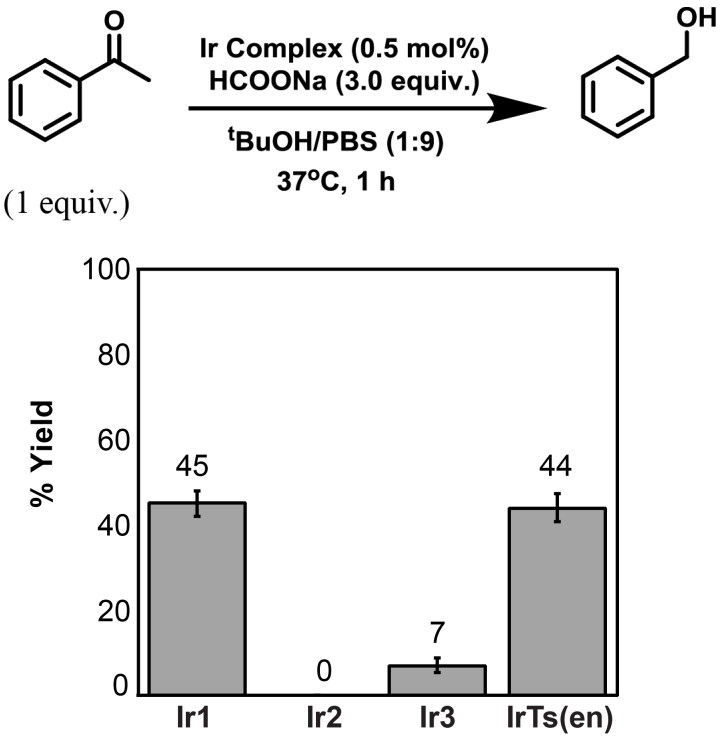

Figure 1. Hydrogenation of benzaldehyde by complexes **Ir1**, **Ir2**, **Ir3,** and **IrTs(en)** using HCOONa as the hydride donor. Reaction conditions: benzaldehyde (18 μmol), HCOONa (54 μmol), Ir complex (0.09 μmol, 30 μM for **Ir1**/**Ir2**/**IrTs(en)** or 0.045 μmol, 15 μM for **Ir3**), ^{t}BuOH/PBS (1:9, 3 mL), 37 °C, 1 h. The reaction yields were determined by gas chromatography analysis using biphenyl as an internal standard. The % yields shown are the average values from three separate runs.

2.2.2. Evaluation of Fluorogenic Substrates

To demonstrate transfer hydrogenation by **Ir1** in living cells, a fluorescent reporter strategy has been adopted to visualize the intracellular reaction in real time. Cells that are treated with a fluorescent probe functionalized with an aldehyde, are expected to exhibit distinct change in fluorescence upon reduction to an alcohol by iridium catalyst and intracellular NADH (Scheme 1). The change in fluorescence associated with the formation of the product alcohol would be monitored over time by fluorescence microscopy.

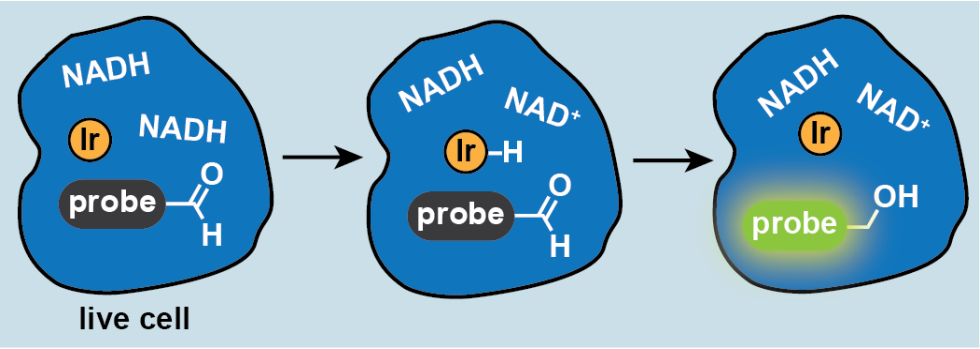

Scheme 1. Proposed reaction of fluorogenic probes containing aldehyde groups inside cells treated with iridium catalyst.

Several aldehyde-containing probe molecules were screened to determine a substrate with the desired photophysical properties and reactivity. Three main criteria were taken into consideration to select the ideal probe, 1) can be readily reduced; 2) show difference in photophysical properties between the substrate and product, and 3) exhibit low energy excitation. Several probes were tested as substrates in transfer hydrogenation

using **Ir1** in the presence of NADH in aqueous solution at 37°C for 24 h. As shown in Table 1, **Bodipy-CHO**, **Probe-1** and **Probe-4** showed probable yield of their corresponding alcohol (20%, (Figure 2) 13%, and 100%, respectively), whereas the other probes were not reduced. Unfortunately, most of the probes that we screened required high energy excitation, which damaging to live cells. Although, **Bodipy-CHO** is not the most active substrate, it had several desirable properties, including having excitation wavelength in the visible region (λ_{ex} = 480 nm) (Table 1) and its reduced form **Bodipy-OH** is five times more emissive (Figure 3a).

Table 1. Evaluation of catalytic transfer hydrogenation efficiency of various fluorophore-aldehyde probes and their photophysical properties

Compound Name	Aldehyde Structure	$\lambda_{ex}/\lambda_{em}$ (nm)	Photophysical Changes Upon Reduction	Reaction Yield
Bodipy-CHO	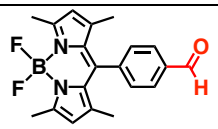	480/518	Alcohol is ~5x more emissive than aldehyde	~20%[a]
Probe-1	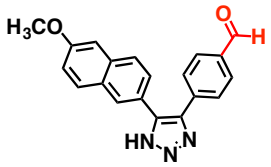	300/359	Alcohol is ~10x more emissive than aldehyde	~13%[b]
Probe-2	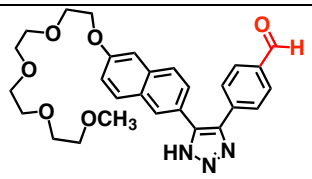	N/A	N/A	<2%[c]
Probe-3	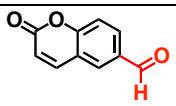	240/405	N/A	0%[d] (over-reduction)
Probe-4	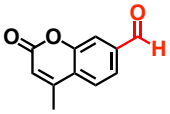	290/389	Alcohol is dimly emissive	100%[e] (in 3 h)
Probe-5	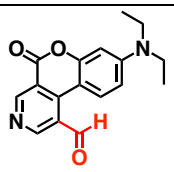	450/508[3]	N/A	0%[f]
Probe-6	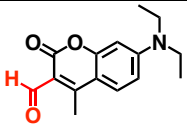	430/490[3]	N/A	0%[g]
Probe-7	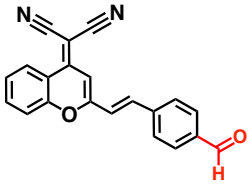	405/625	Non-fluorescent	N/A

[a]Conditions: 19 μM of **Ir1** (2 mol%) with 2.0 equiv. of NADH in 63:36:1 H_2O/^{t}BuOH/DMSO. [b]Conditions: 60 μM of **Ir1** (6 mol%) with 1.5 equiv. of HCOONa in 1:2 ethylene glycol/RPMI. [c]Conditions:100 μM of **Ir1** (2 mol%) with 1.1 equiv. of NADH in 1:4 ^{t}BuOH/H_2O. [d]Conditions: 214 μM of **Ir1** (1.86 mol%) with 1.05 equiv. of NADH in 1:4 ^{t}BuOH/H_2O. [e]Conditions: 90 μM of **Ir1** (1.9 mol%) with 1.8 equiv. of NADH in 1:4 ^{t}BuOH/H_2O. [f]Conditions: 40 μM **Ir1** (2 mol%) with 1.2 equiv. of NADH in 1:2 ^{t}BuOH/H_2O. [g]Conditions: 40 μM of **Ir1** (2 mol%) with 1.2 equiv. of NADH in 1:2 ^{t}BuOH/H_2O.

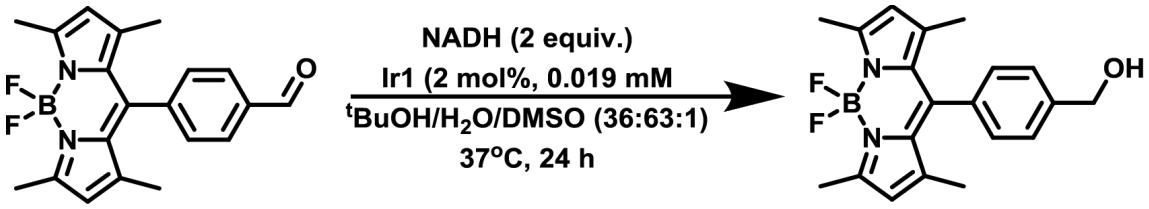

Scheme 2. Reaction of **Bodipy-CHO** with NADH using **Ir1** as catalyst.

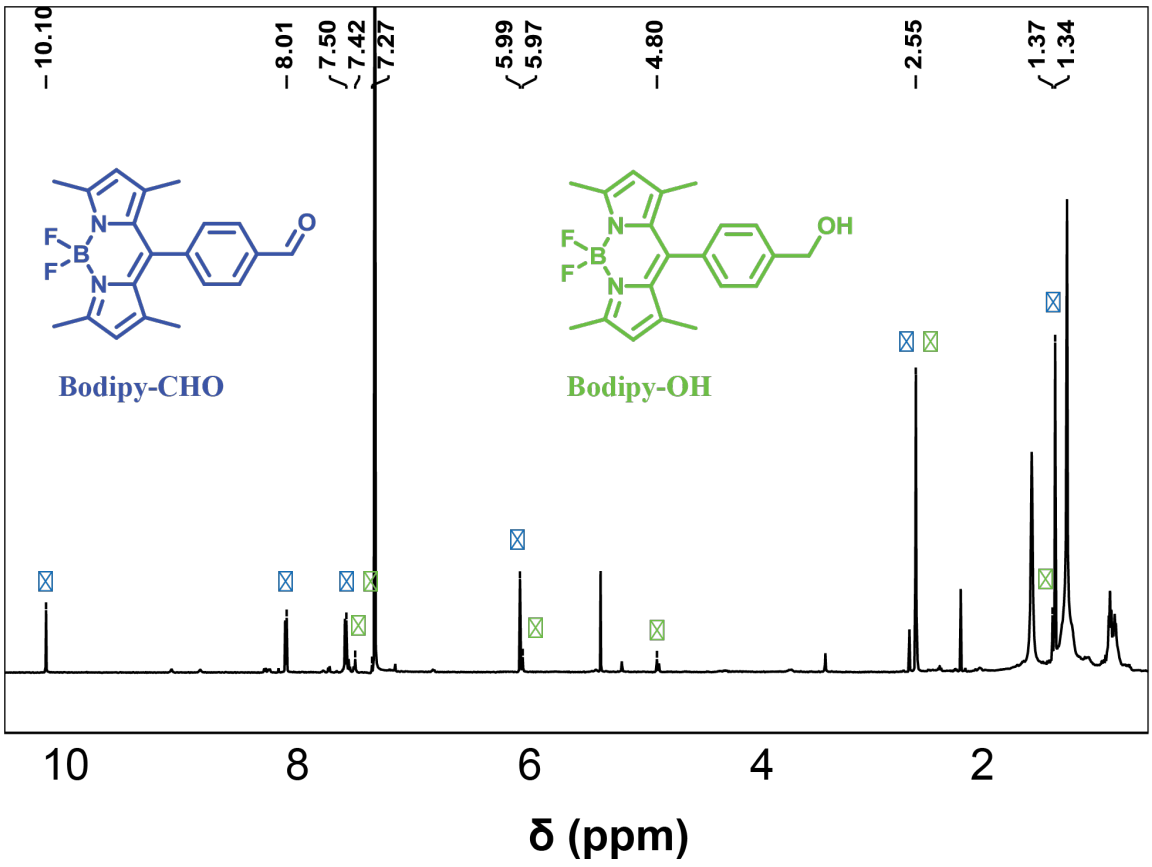

Figure 2. ^{1}H NMR spectrum (600 MHz, $CDCl_3$) of the organic extract from the reaction of **Bodipy-CHO** (0.5 mg, 1.53 μmol) with NADH (2.5 mg, 3.28 μmol) in the presence of **Ir1** (16.8 μg, 0.03 μmol) in 1.6 mL of H_2O/^{t}BuOH/DMSO (63:36:1). The yield of **Bodipy-OH** was estimated to be ~20% based on ^{1}H NMR signal integration. The peak assignments for **Bodipy-CHO** are shown as blue squares and the peak assignments for **Bodipy-OH** are shown as green squares.

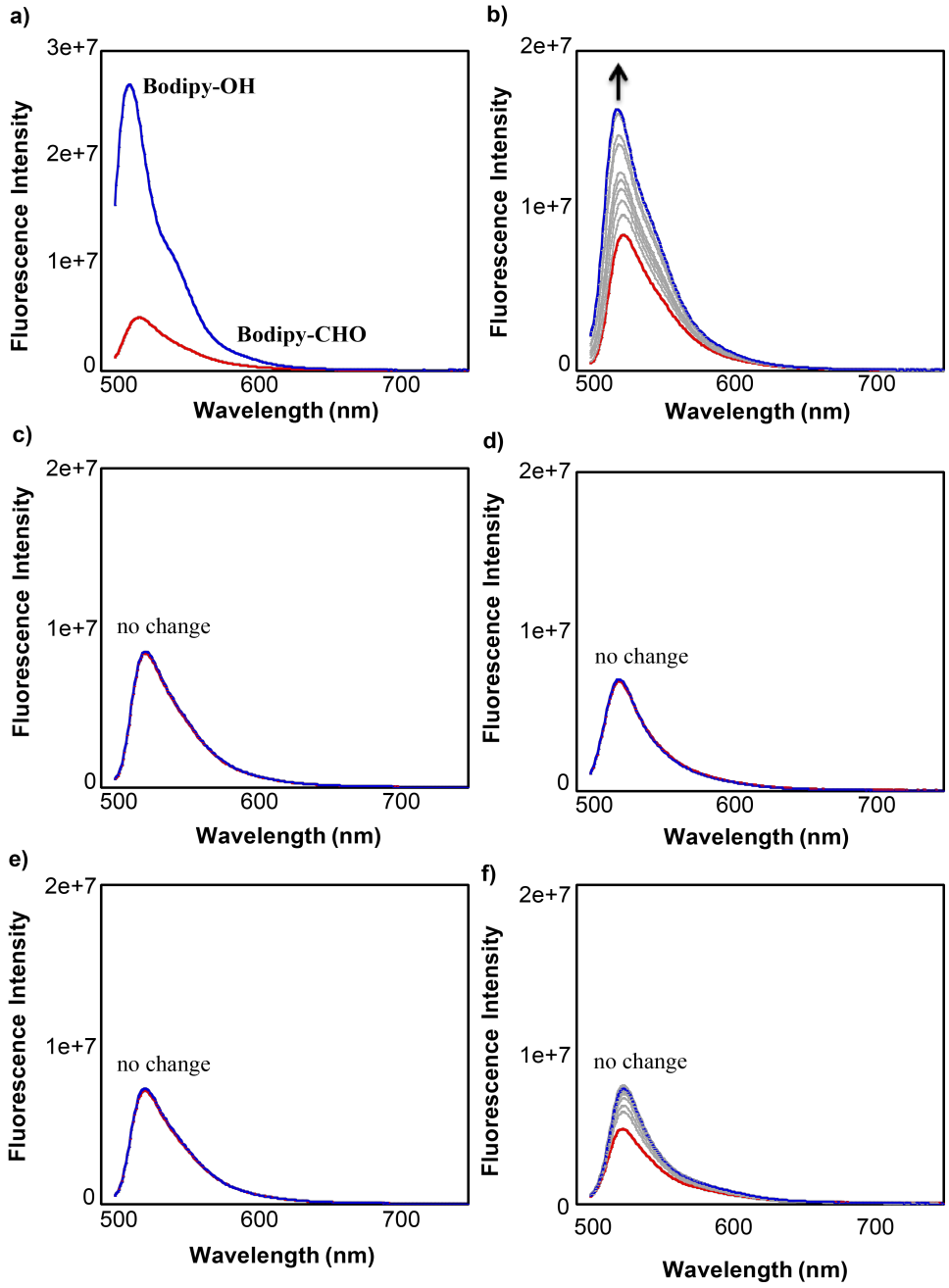

Figure 3. a) Fluorescence spectra of **Bodipy-CHO** (8.5 μM, blue trace) and **Bodipy-OH** (8.5 μM, green trace) recorded in ^{t}BuOH/H_2O (1:4) at RT in air. The fluorescence changes were monitored for the reaction of b) **Bodipy-CHO** (30 μM) + NADH (100 μM) + **Ir1** (30 μM) in ^{t}BuOH/H_2O (1:4) for 4 h; c) **Bodipy-CHO** (30 μM) + NADH (100 μM) in ^{t}BuOH/H_2O (1:4) for 15 h; d) **Bodipy-CHO** (30 μM) + NADH (100 μM) + **Ir2** (30 μM) in ^{t}BuOH/H_2O (1:4) for 4 h; e) **Bodipy-CHO** (30 μM) + NADH (100 μM) + **Ir3** (30 μM) in ^{t}BuOH/H_2O (1:4) for 5.5 h; f) **Bodipy-CHO** (30 μM) + NADH (100 μM) + **Ir3** (30 μM) in ^{t}BuOH/DMEM (1:4) for 15 h.

The reaction of **Bodipy-CHO** (30 μM) and **Ir1** (30 μM) /NADH (100 μM) in the cuvette led to an ~1.9-fold increase in fluorescence emission at 520 nm over the course of 4 h due to the formation of **Bodipy-OH** (Figure 3b). In contrast, no fluorescence increase was observed in control reactions without catalyst (Figure 3c). For comparison, the reaction of **Bodipy-CHO** (30 μM) with **Ir2** (30 μM) / NADH (100 μM) under similar reaction conditions did not result in any fluorescence enhancement (Figure 3d), which is consistent with our previous finding that **Ir1** is a more active transfer hydrogenation catalyst than **Ir2**.[13] The iridium precursor **Ir3**, without a supporting bidentate ligand, was inactive as a catalyst in both water and DMEM (Dulbecco's Modified Eagle Medium, Figure 3e & 3f). Although **Bodipy-CHO** has been shown to turn-on in the presence of cysteine and homocysteine,[24] we found that in the presence of biologically relevant concentrations of these sulfur containing amino acids (the concentrations of free cysteine and homocysteine in cells are approximately 400[25] and 15[26] μM, respectively), the fluorescence increase was negligible (Figure 4). These results indicated that the **Bodipy-CHO** compound would be a suitable reaction probe for our cell experiments.

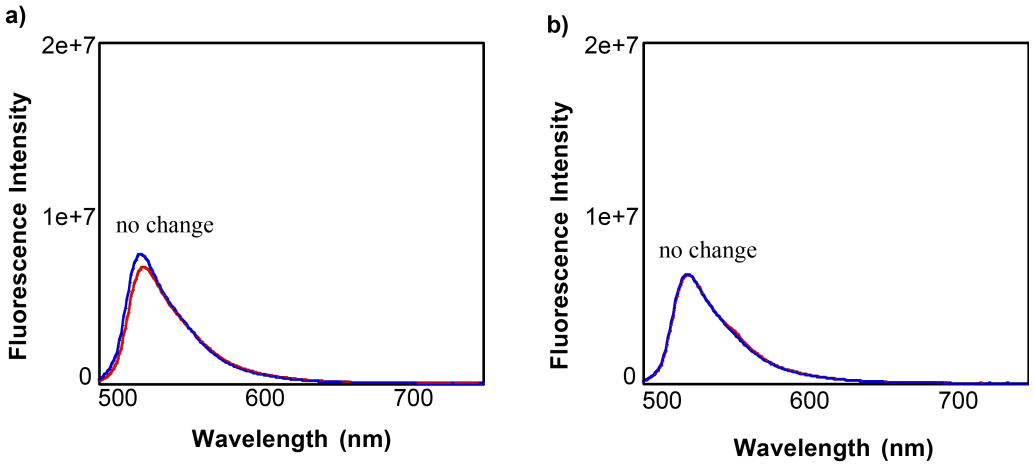

Figure 4. Fluorescence spectra obtained from the reaction of **Bodipy-CHO** (30 μM) with either a) cysteine (400 μM) or b) homocysteine (15 μM) in ^{t}BuOH/0.1 M HEPES buffer (1:4) for 6 h at RT in air. The starting spectra are shown in red, whereas the final spectra are shown in blue. The concentrations of free cysteine and homocysteine in cells are approximately 400[25] and 15[26] μM, respectively.

2.2.3. Intracellular Transfer Hydrogenation Reactions

Imaging studies using live NIH-3T3 mouse embryo fibroblast cells were carried out next using eight-well slides. As controls cells were incubated with 30 μM of **Bodipy-CHO** or **Bodipy-OH** for 4 h and then images were acquired using a confocal fluorescence microscope (40× lens air objective, 488 nm excitation). The relative integrated fluorescence intensities of the cell images were quantified using the program ImageJ and reported as the fold-change relative to that of the **Bodipy-CHO** treated cells for comparison (Figure 5). Cells that were treated with **Bodipy-CHO** showed weak fluorescence (Figure 6, 1.0×) whereas cells that were treated with **Bodipy-OH** showed more intense fluorescence (Figure 6, 2.2×). Interestingly, when the cells were incubated with 30 μM of **Bodipy-CHO**, washed with fresh media, and then exposed to a solution containing 20 μM of **Ir1**, increasing fluorescence signals in the interior of the cells were

observed over time (Figure 6). An integrated fluorescence enhancement of 1.6-fold was obtained after 2 h compared to that of the **Bodipy-CHO** control wells, suggesting that the reduction of **Bodipy-CHO** to **Bodipy-OH** had occurred. Importantly, the bright-field images of the cells show that they are healthy and were not adversely affected by the presence of the probes or catalysts during the length of the imaging experiments (Figures 6-9). This observation was further confirmed by cytotoxicity measurements (Figure 10). When analogous studies were performed using **Ir2**, **Ir3**, or $IrCl_3$ salt as the iridium source, no significant increase in fluorescence was detected (Figures 7 and 8), which indicated that the conversion of **Bodipy-CHO** to **Bodipy-OH** required a sufficiently active transfer hydrogenation catalyst (e.g., **Ir1**) to proceed. Similar results were obtained when imaging studies were performed using A549 human epithelial cancer cell lines (Figure 9).

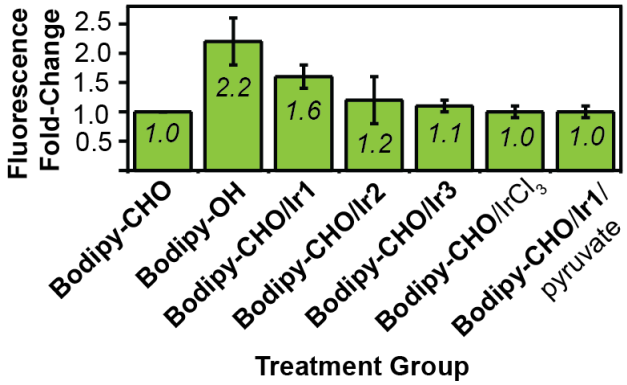

Figure 5. The fold-change in fluorescence of cells in different treatment groups relative to that observed in the **Bodipy-CHO** only treated cells. The fold-change values are the average measurements obtained from triplicate of duplicate experiments, and the error bars show the standard deviation from the mean.

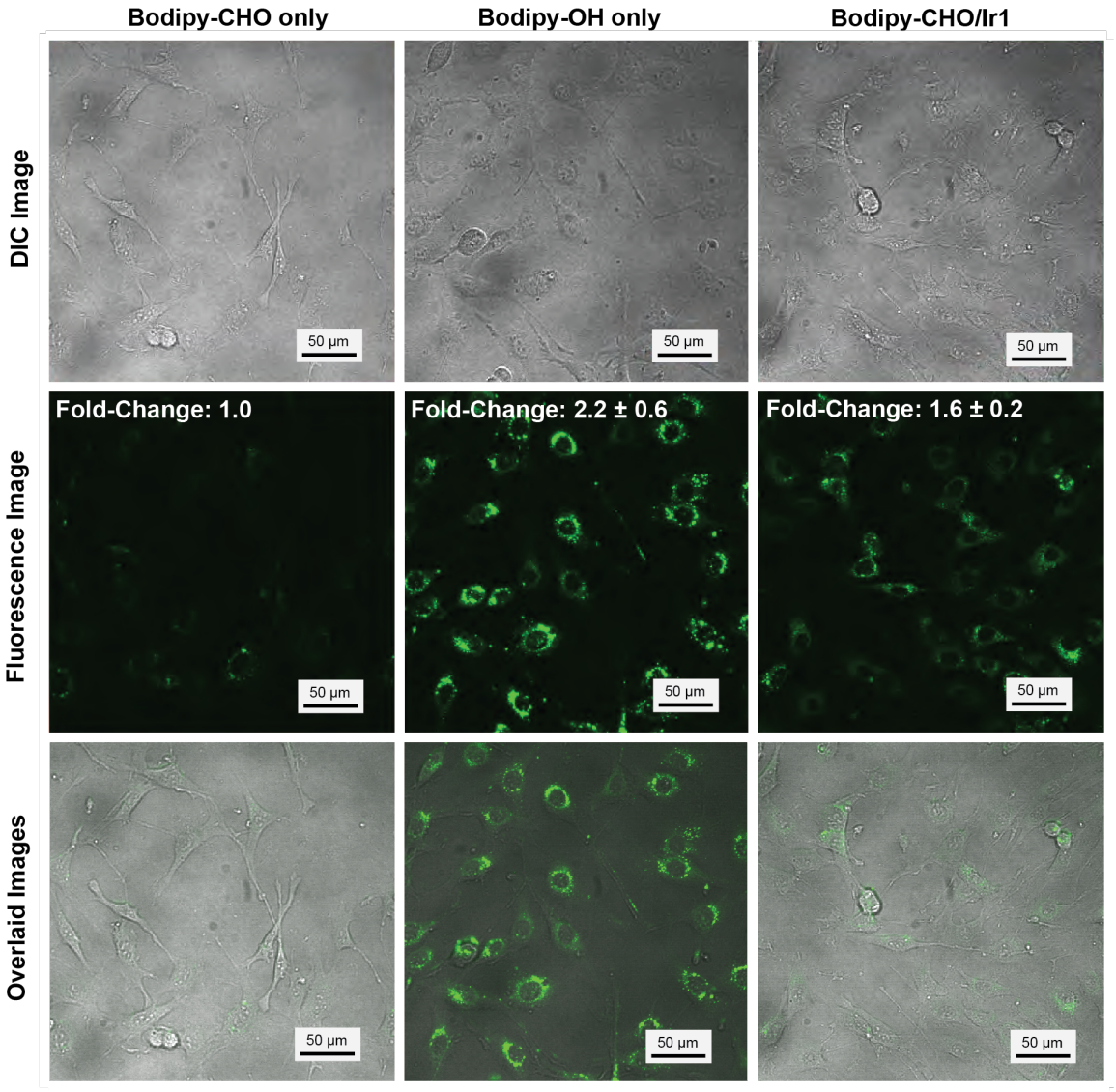

Figure 6. Representative fluorescence confocal microscope images (40× objective) of NIH-3T3 cells treated with **Bodipy-CHO** (30 µM) (left column), **Bodipy-OH** (30 µM) (middle column), and **Bodipy-CHO** (30 µM)/**Ir1** (20 µM) (right column). The cells were treated with **Bodipy** for 4 h followed by either Ir or DMSO for 2 h before their images were acquired. The fluorescence fold-change values indicated are determined based on the relationship: [corrected total cell fluorescence of treated cells]/[corrected total cell fluorescence of **Bodipy-CHO** treated cells]. The fold-change values are the average acquired from three separate experiments each performed in duplicate. The top row shows differential interference contrast (DIC) images, the middle row shows fluorescence images, and the bottom row shows an overlay of both the DIC and fluorescence images.

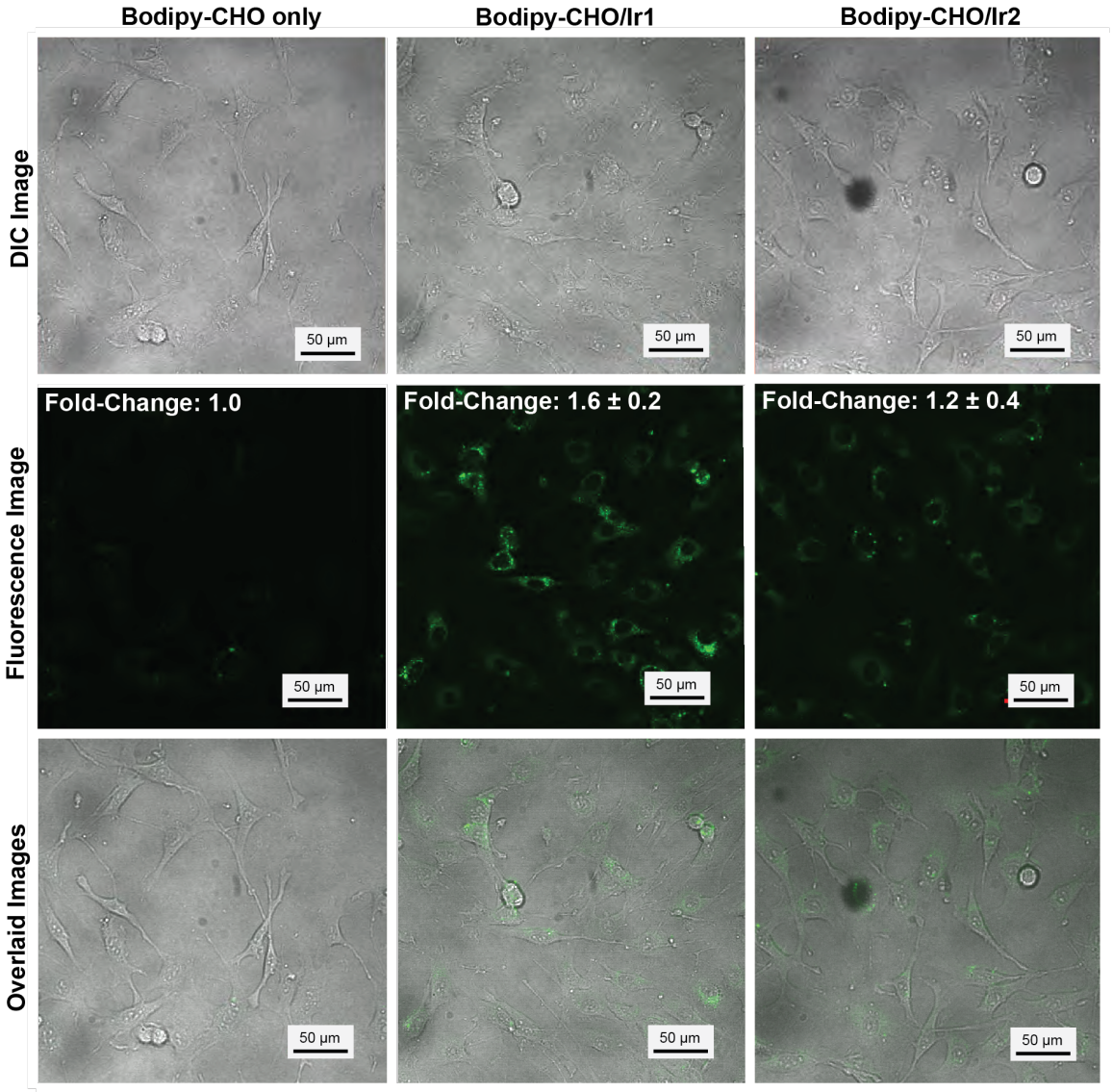

Figure 7. Representative fluorescence confocal microscope images (40× objective) of NIH-3T3 cells treated with **Bodipy-CHO** (30 µM) only (left column), **Bodipy-CHO** (30 µM)/**Ir1** (20 µM) (middle column), and **Bodipy-CHO** (30 µM)/**Ir2** (20 µM) (right column). The cells were treated with **Bodipy** for 4 h followed by either Ir or DMSO for 2 h before their images were acquired. The fluorescence fold-change values indicated are determined based on the relationship: [corrected total cell fluorescence of treated cells]/[corrected total cell fluorescence of **Bodipy-CHO** treated cells]. The fold-change values are the average acquired from three separate experiments each performed in duplicate. The top row shows differential interference contrast (DIC) images, the middle row shows fluorescence images, and the bottom row shows an overlay of both the DIC and fluorescence images.

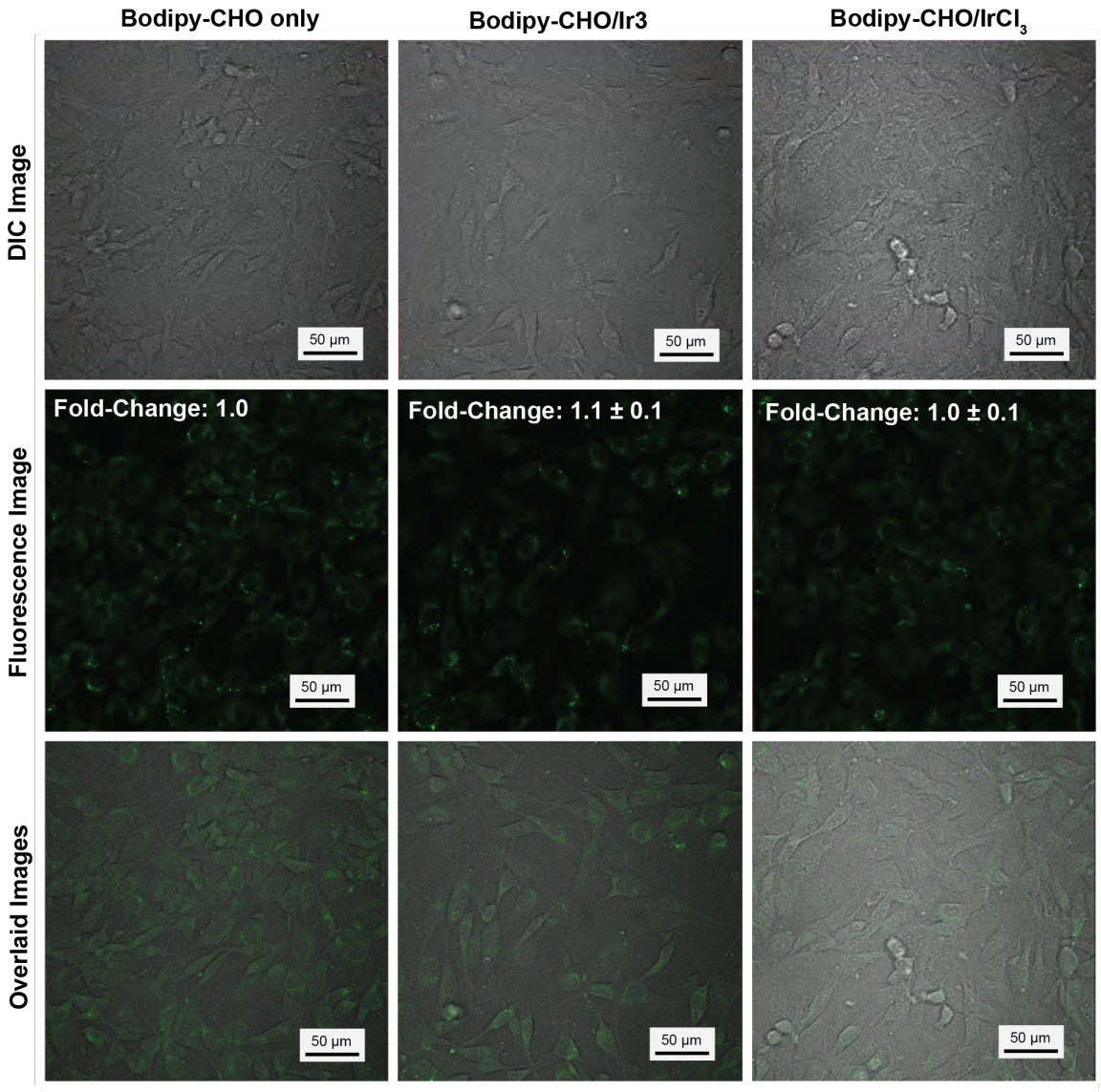

Figure 8. Representative fluorescence confocal microscope images (40× objective) of NIH-3T3 cells treated with **Bodipy-CHO** (30 µM) (left column) only, **Bodipy-CHO** (30 µM)/**Ir3** (10 µM) (middle column), and **Bodipy-CHO** (30 µM)/$IrCl_3$ salt (20 µM) (right column). The cells were treated with **Bodipy** for 4 h followed by either Ir or DMSO for 2 h before their images were acquired. The fluorescence fold-change values indicated are determined based on the relationship: [corrected total cell fluorescence of treated cells]/[corrected total cell fluorescence of **Bodipy-CHO** treated cells]. The fold-change values are the average acquired from three separate experiments each performed in duplicate. The top row shows differential interference contrast (DIC) images, the middle row shows fluorescence images, and the bottom row shows an overlay of both the DIC and fluorescence images.

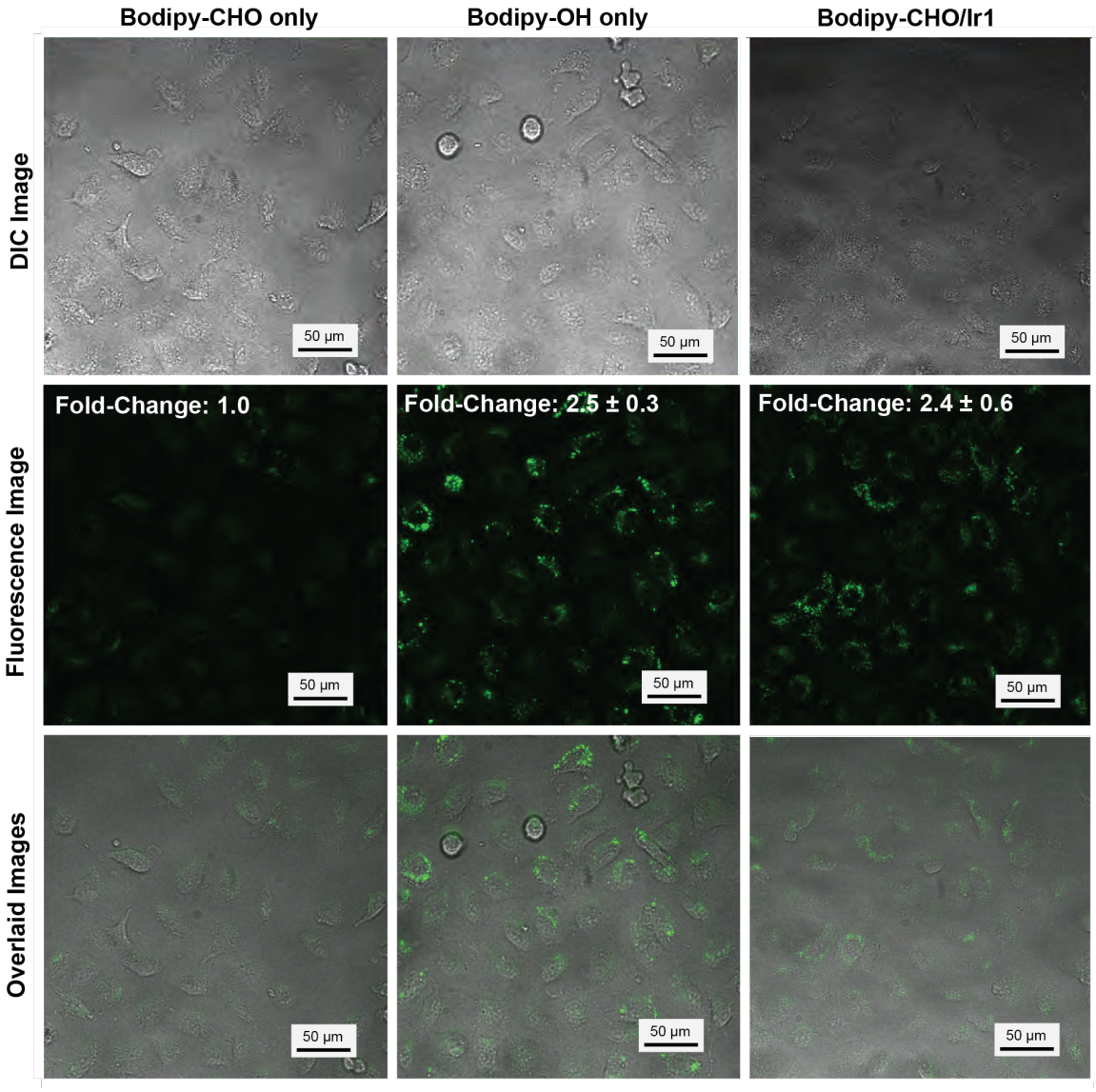

Figure 9. Representative fluorescence confocal microscope images (40× objective) of A549 human epithelial cells treated with **Bodipy-CHO** (30 µM) only (left column), **Bodipy-OH** (30 µM) (middle column), and **Bodipy-CHO** (30 µM)/**Ir1** (20 µM) (right column). The cells were treated with **Bodipy** for 4 h followed by either Ir or DMSO for 2 h before their images were acquired. The fluorescence fold-change values indicated are determined based on the relationship: [corrected total cell fluorescence of treated cells]/[corrected total cell fluorescence of **Bodipy-CHO** treated cells]. The fold-change values are the average acquired from three separate experiments each performed in duplicate. The top row shows differential interference contrast (DIC) images, the middle row shows fluorescence images, and the bottom row shows an overlay of both the DIC and fluorescence images.

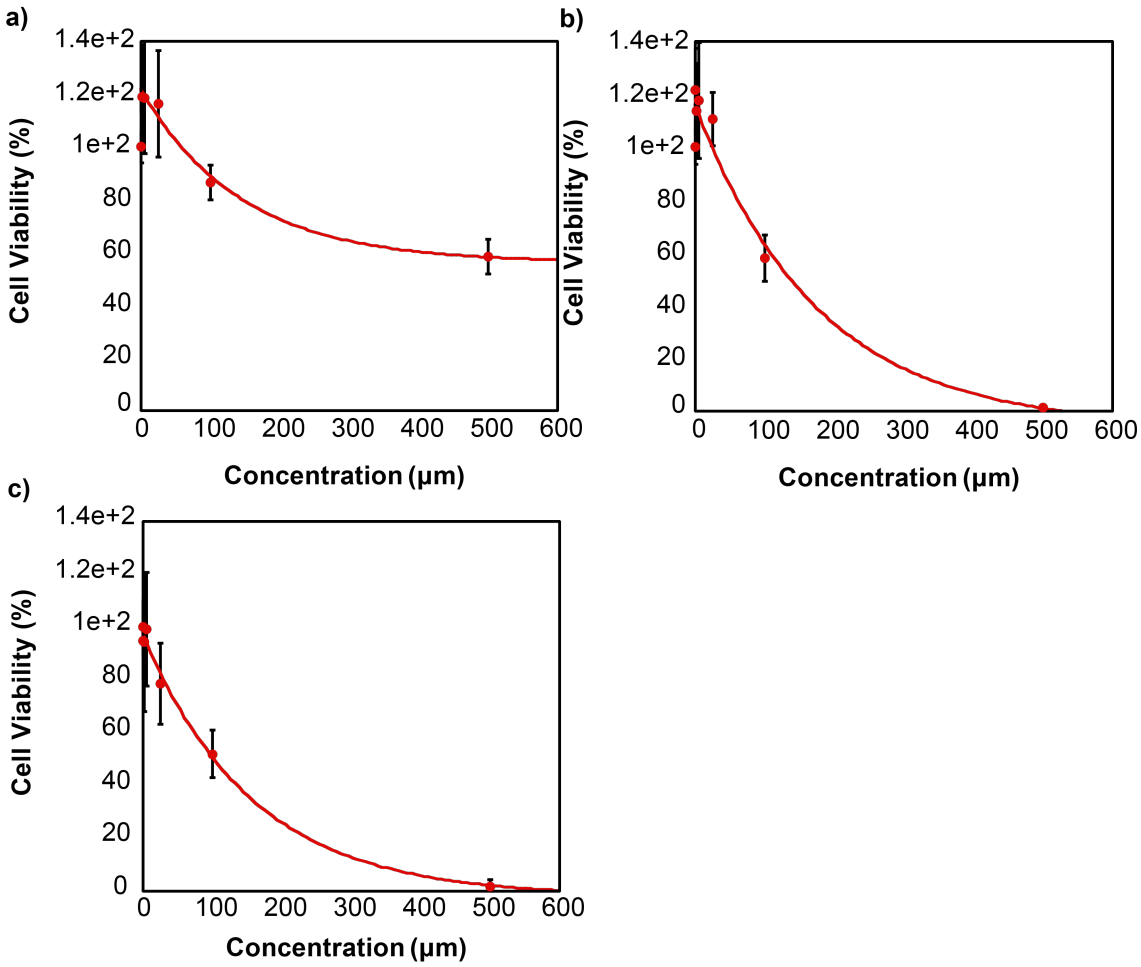

Figure 10. Cytotoxicity data obtained from the treatment of NIH-3T3 mouse fibroblast cells with a) **Bodipy-CHO**, b) **Bodipy-OH**, and c) **Ir1** for 3 h (+1 h incubation with MTS). The cell viability percentage was determined using a colorimetric MTS assay. The IC_{50} values for **Bodipy- CHO**, **Bodipy-OH**, and **Ir1** were determined to be >500, 79 ± 20, and 108 ± 3 μM, respectively.

To independently verify the results of the imaging studies, the cell lysate from the different cell treatment groups were analyzed using fluorescence spectroscopy. For these experiments, NIH-3T3 cells were grown in tissue culture plates and then exposed to either **Bodipy-CHO** (30 μM), **Bodipy-OH** (30 μM), or **Bodipy-CHO** (30 μM)/**Ir1** (20

μM) for 2 h. The cells were then detached, concentrated, and then lysed in a water/ acetonitrile/methanol (1:2:2) mixture. The fluorescence spectra of the cell lysates were then recorded. The integrated fluorescence from 490-650 nm was normalized based on the cell density of each culture plate. It was determined that the **Bodipy-OH** and **Bodipy-CHO/Ir1** treatment groups exhibited a 3.4× and 2.4× increase in fluorescence, respectively, relative to that of the **Bodipy-CHO** control (1.0×) (Table 2). Once again, these data suggested that the **Ir1** complex was responsible for catalyzing the formation of **Bodipy-OH** from **Bodipy-CHO** inside the NIH-3T3 cells.

We proposed that the intracellular reduction of the aldehyde probe occurs through transfer hydrogenation between NADH and **Bodipy-CHO** catalyzed by **Ir1**. It has been shown, in previous studies, that organoiridium complexes increase the $[NAD^+]/[NADH]$ ratio in mammalian cells,[22,27] presumably due to their reaction with NADH to generate iridium-hydride species that can react further with dioxygen,[12] protons,[28] or organic acceptors.[29] We reasoned that if the NADH levels inside the cell could be artificially lowered, then fewer endogenous hydride sources are available to perform reductive chemistry (Scheme 3). To test this hypothesis, NIH-3T3 cells were treated with 10 mM of sodium pyruvate, which is a natural metabolite that signals the slowdown of glycolysis to reduce the generation of NADH.[30] As seen in Figure 11, the pyruvate-treated cells did not show an increase in fluorescence in the presence of **Bodipy-CHO/Ir1** compared to those treated with only **Bodipy-CHO**, suggesting that transfer hydrogenation to the probe was effectively suppressed. Although Sadler and co-workers have reported that pyruvate itself can serve as a substrate for transfer hydrogenation,[10] which would neutralize its intended role as a metabolic redox modulator. It was found that only about 4% of the reduced

product lactate was formed from the reaction of pyruvate/NADH in presence of **Ir1** after 4.5 h (Figure 12). Reactions in the cuvette showed that **Bodipy-CHO** could still be reduced by **Ir1**/NADH in the presence of pyruvate at up to 10 mM (Figure 13). Thus, we propose that reduction in cellular fluorescence in the presence of pyruvate is due to a decrease in the intracellular NADH concentration. However, additional experiments are needed to determine whether there is a correlation between the amounts of NADH in the cell with transfer hydrogenation efficiency.

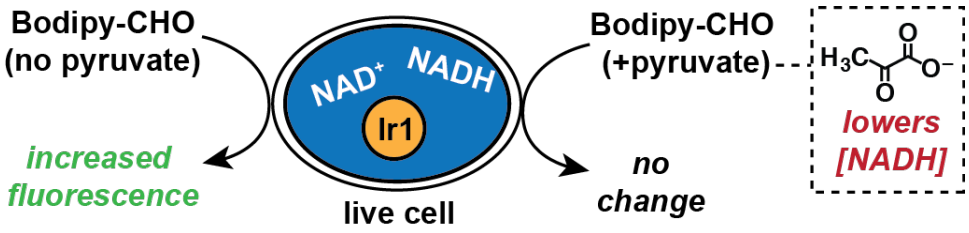

Scheme 3. Effect of pyruvate on cell fluorescence.

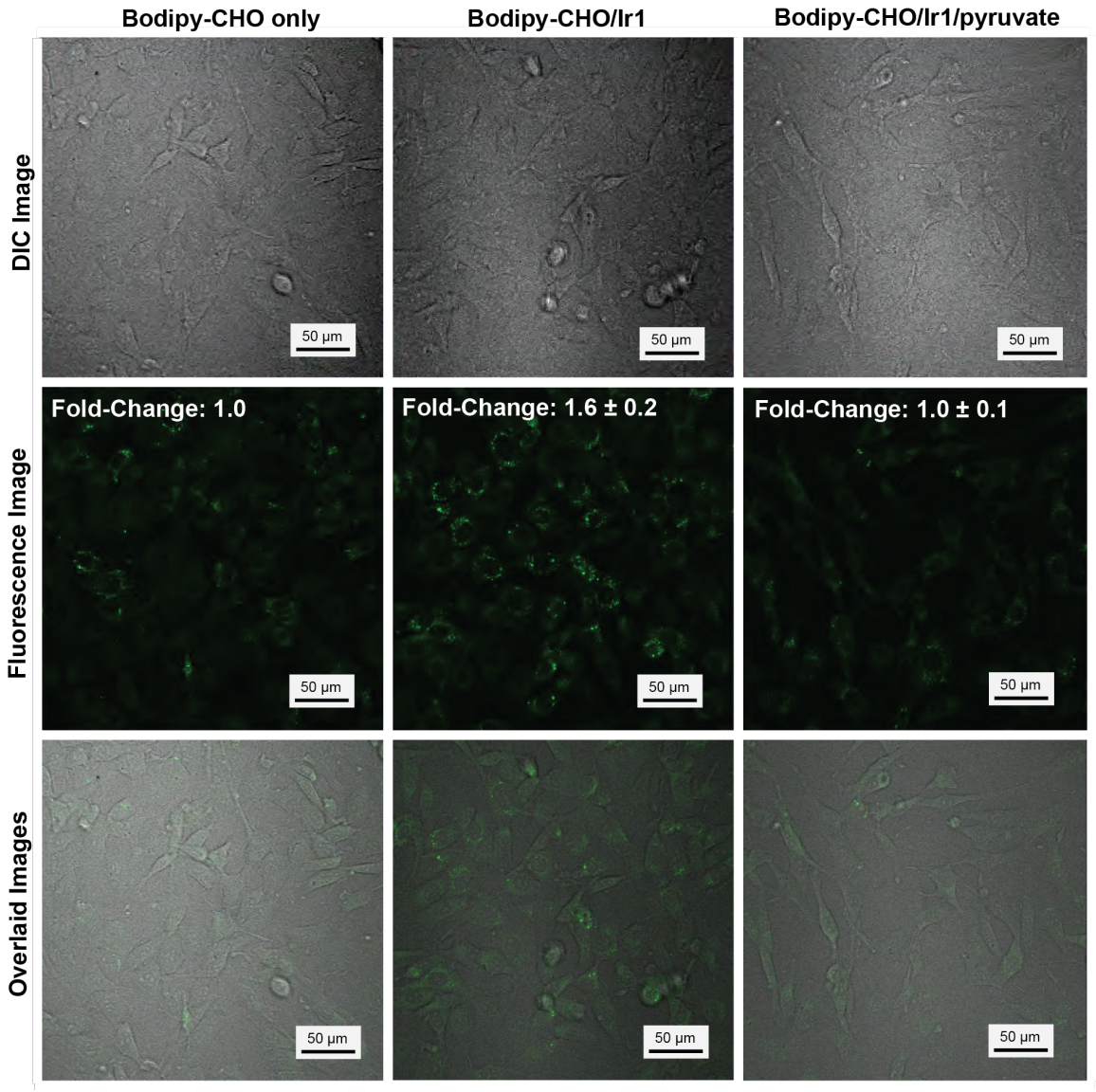

Figure 11. Representative fluorescence confocal microscope images (40× objective) of NIH-3T3 cells treated with **Bodipy-CHO** (30 µM) only (left column), **Bodipy-CHO** (30 µM)/**Ir1** (20 µM) (middle column), and **Bodipy-CHO** (30 µM)/**Ir1** (20 µM)/pyruvate (10 mM) (right column). The cells were treated with **Bodipy** for 4 h followed by DMSO, **Ir1**, or **Ir1**/pyruvate for 2 h before their images were acquired. The fluorescence fold-change values indicated are determined based on the relationship: [corrected total cell fluorescence of treated cells]/[corrected total cell fluorescence of **Bodipy-CHO** treated cells]. The fold-change values are the average acquired from three separate experiments each performed in duplicate. The top row shows differential interference contrast (DIC) images, the middle row shows fluorescence images, and the bottom row shows an overlay of both the DIC and fluorescence images.

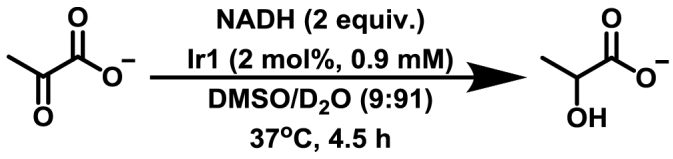

Pyruvate
(1 equiv.)

Lactate

Scheme 4. Reaction of pyruvate with NADH using **Ir1** as catalyst.

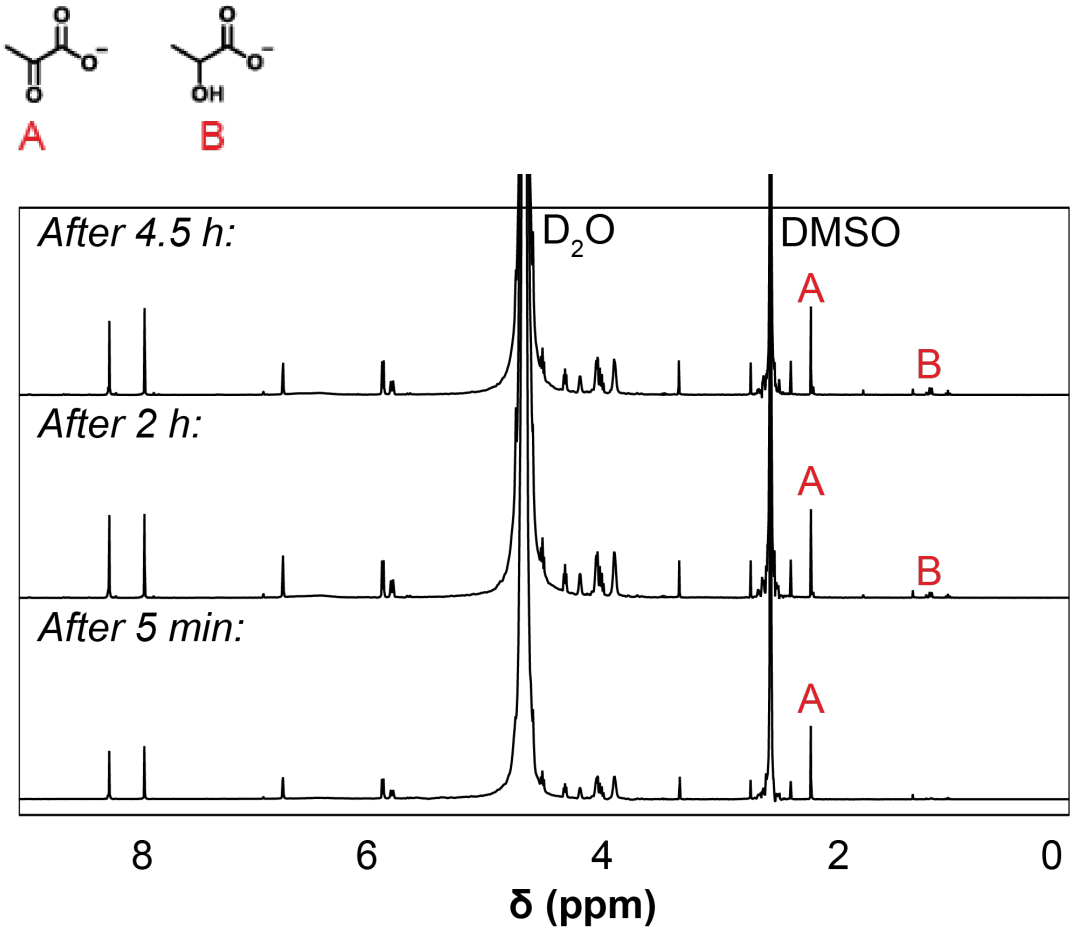

Figure 12. ^{1}H NMR spectra (600 MHz, D_2O) from the reaction of pyruvate (0.5 mL of 100 mM, 5.5 mg, 0.05 mmol) with NADH (76.3 mg, 0.1 mmol, 91 mM) in the presence of **Ir1** (0.5 mg, 0.99 μmol, 2 mol%, 0.9 mM) in 0.5 mL of D_2O after 15 min (bottom), 2 h (middle), and 4.5 h (top). After reaction for 4.5 h, only about ~4% of lactate has formed. The signals corresponding to the methyl groups of pyruvate and lactate are labeled with letters A and B, respectively. The unlabeled peaks are derived from NADH, NAD^+, and the iridium complex.

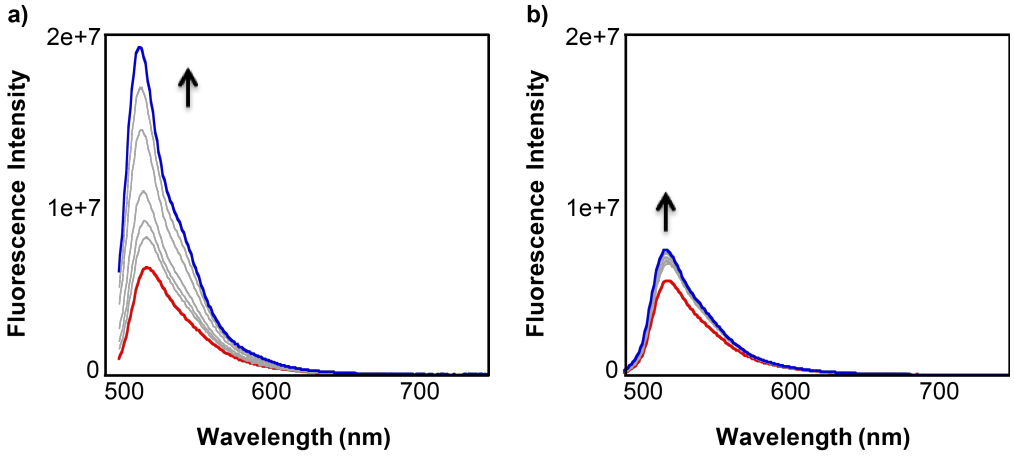

Figure 13. Fluorescence spectra obtained from the reaction of a) **Bodipy-CHO** (30 μM) + NADH (100 μM) + **Ir1** (30 μM) + pyruvate (30 μM) in ^{t}BuOH/H_2O (1:4) for 4 h; and b) **Bodipy-CHO** (30 μM) + NADH (100 μM) + **Ir1** (30 μM) + pyruvate (10 mM) in ^{t}BuOH/H_2O (1:4) for 4 h.

Lastly, to confirm that the organoiridium complexes can cross the membrane bilayers of NIH-3T3 cells, their Ir concentrations were measured by inductively coupled plasma mass spectrometry (ICP-MS). Because Ir is not a biologically abundant metal ion, the presence of Ir inside cells that were treated with an organoiridium complex would indicate their successful cellular entry. It was found that cells that were exposed to 20 μM of **Ir1**, **Ir2**, or **Ir3** for 2 h on average retained about 530, 40, and 2 ng of iridium per 10^6 cells, respectively. Although **Ir1** accumulates more in cells compared to the other Ir species, we hypothesize that it promotes greater fluorescence enhancement in the cell studies above (Figure 5) due to its increased activity rather than cellular uptake. Experiments to quantify the catalyst's turnover numbers are required to obtain further support.

2.3. Conclusions

Using a fluorogenic aldehyde-containing probe, we have demonstrated that unprotected organoiridium complexes can promote transfer hydrogenation inside living cells. Several lines of evidence provide support that the reactions take place intracellularly rather than extracellularly, including the observations that the fluorescence of the **Bodipy-OH** compound develops within the cytoplasm of the cell, the iridium catalyst is retained in the cell interior, and endogenous NADH (or NADPH) is required for aldehyde reduction to occur. We will investigate further this intracellular transfer hydrogenation chemistry, including possible cellular localization of the Ir catalysts, their catalytic efficiency, and ways to improve their catalytic performance. Our method of using an additive-free nontoxic catalyst system is simple to implement, is amenable to scale-up, and provides a versatile new tool for the chemical biology toolbox. Most importantly, this advance will enable novel biotechnologies to be developed, such as the detoxification of cytotoxic aldehydes implicated in neurodegenerative disorders[13] or the creation of new intracellular bioconjugation methods.[31]

2.4. Experimental Section

2.4.1. General Procedures

Commercial reagents were used as received without further purification. All air- and water-sensitive manipulations were performed using standard Schlenk techniques or under a nitrogen atmosphere using a glovebox. Anhydrous solvents were obtained from an Innovative Technology solvent drying system saturated with Argon. **Bodipy-CHO** and **Bodipy-OH** were synthesized according to literature procedures.[24] Coumarin-6-

carboxaldehyde (**Probe-3**) and 4-methyl-2- oxo-2H-chromene-7-carbaldehyde (**Probe-4**) were purchased from Sigma Aldrich and VWR, respectively. The compounds 4-[5-(6-methoxynaphthalen-2-yl)-1H-[1,2,3]triazol-4-yl]benzaldehyde (**Probe-1**),[32] 1-formyl-8-diethylamino-5-H-[1]benzopyrano[3,4-c]pyridin-5-one (**Probe-5**),[33] 3- formyl-4-methyl-7-diethylamino-2-H-benzopyran-2-one (**Probe-6**)[33] were synthesized according to literature procedures. The iridium complexes **Ir1**[34], **Ir2**[35], and **Ir3**[36] were prepared as previously described. NIH-3T3 mouse fibroblast and A549 human epithelial cells were obtained from ATCC.

Physical Methods. NMR spectra were acquired using JEOL spectrometers (ECA-400, 500, and 600) at room temperature and referenced using residual solvent peaks. A Horiba Fluoromax 4 fluorometer was used to record emission spectra. A Varian 810 instrument was used to acquire inductively coupled plasma-mass spectrometry (ICP-MS) analyses. All biological cell images were obtained using a Nikon A1-Rsi inverted confocal microscope equipped with a 40× air objective at the BioScience Research Collaborative (BRC) imaging core at Rice University (Houston, TX).

2.4.2. Synthesis

Compound 2a. Sodium hydride (1.19 g, 29.81 mmol, 2.5 equiv., 60% dispersion) was added to 6-bromo-2-napthol (2.66 g, 11.92 mmol, 1.0 equiv.) in dry THF (20 mL) at 0°C under N_2 and stirred for two hours at RT. Tetra(ethylene glycol) methyl ether tosylate (4.32 g, 11. 92 mmol, 1.0 equiv.) was added to the reaction mixture and then stirred overnight under N_2. The reaction was quenched by the slow addition of water and the product was extracted into diethyl ether (3×30 mL). The organic layer was separated,

dried over anhydrous Na_2SO_4, filtered, and then the solvent was removed by rotatory evaporation. The crude product was purified by silica gel column chromatography (1:4 ethyl acetate/hexane) to yield a brown-colored oil (96%, 4.76 g, 11.51 mmol). ^{1}H NMR (600 MHz, $CDCl_3$): 7.67 (s, 1H), 7.40 (d, J = 6 Hz, 1H), 7.34 (d, J = 6 Hz, 1H), 7.28 (d, J = 6 Hz, 1H), 7.00 (d, J= 6 Hz, 1H), 6.85 (s, 1H), 3.97 (t, J= 6 Hz, 2H), 3.69 (t, J= 6 Hz, 2H), 3.55(m, 2H), 3.47 (m, 9H) 3.34 (m, 2H), 3.18 (s, 3H) ppm. ^{13}C NMR (125 MHz, $CDCl_3$): δ = 157.02, 132.93, 129.93, 129.43, 128.40, 120.05, 116.94, 106.52, 71.85, 70.75, 70.54, 70.41, 69.53, 67.38, 58.88 ppm. IR: ν (cm^{-1}) = 2870, 1625, 1589, 1500, 1451, 1388, 1350, 1259, 1206, 1101, 1062, 972, 928, 875, 849, 798, 737, 647, 591, 547.

Compound 2b. Solid 4-ethynylbenzaldehyde (0.133 g, 1.02 mmol, 1.1 equiv.) and compound **2a** (0.383 g, 0.93 mmol, 1.0 equiv.) were dissolved in dry THF (30 mL) at RT. The mixture was then charged with tetrakis(triphenylphosphine)palladium(0) (0.05 g, 0.047 mmol, 0.05 equiv.), copper(I) iodide (0.04 g, 0.19 mmol, 0.20 equiv.), and triethylamine (2 mL) and then stirred under reflux for about 20 h. The reaction was then cooled to RT, filtered, and the solvent was removed by rotatory evaporation. The crude product was purified by silica gel column chromatography (ethyl acetate/hexane, solvent gradient used from 3:2 to 9:1) and subsequent recrystallization from ethyl acetate/hexane to yield a light brown solid (30%, 0.14g). ^{1}H NMR (600 MHz, $CDCl_3$): 10.01 (s, 1H), 7.99 (s, 1H), 7.87 (d, J = 12 Hz, 2H),

7.68 (m, 4H), 7.52 (d, J = 12 Hz, 1H), 7.19 (d, J = 12 Hz, 1H), 7.11 (s, 1H), 4.25 (t, J = 6 Hz, 2H), 3.92 (t, J = 6 Hz, 2H), 3.75 (t, J = 6 Hz, 2H), 3.65 (m, 9H), 3.52 (t, J = 6 Hz, 2H), 3.35 (s, 3H) ppm. ^{13}C NMR (125 MHz, $CDCl_3$): 191.57, 157.90, 135.33, 134.51, 132.13, 131.89, 129.95, 129.72, 129.54, 128.91, 128.55, 127.12, 120.02, 117.44, 106.83, 94.36, 88.42, 72.01, 70.97, 70.74, 70.70, 70.61, 69.73, 67.60, 59.14 ppm. IR: ν (cm^{-1}) = 2875, 1697, 1621, 1603, 1559, 1495, 1471, 1451, 1408, 1393, 1363, 1345, 1298, 1282, 1268, 1257, 1239, 1208, 1202, 1172, 1158, 1125, 1105, 1052, 1028, 975, 955, 898, 858, 845, 825, 815, 806, 768, 664, 616.

Compound Probe-2. Compound **2b** (0.97 g, 2.1 mmol, 1.0 equiv.) and NaN_3 (0.55 g, 8.39 mmol, 4.0 equiv.) were dissolved in 35 mL of DMF and 12 mL of H_2O. The reaction was stirred at 100°C for 6 h. The mixture was then concentrated under vacuum. Water was added and the organic products were extracted into ethyl acetate (3×30 mL). The organic layers were combined and dried over Na_2SO_4, filtered, and then the solution was evaporated to dryness. The crude material was purified by silica gel column chromatography (1:99 methanol/DCM) to afford the desired product as a brown oil (43%, 0.43 g). ^{1}H NMR (600 MHz, $CDCl_3$): δ = 9.94 (s, 1H), 7.86 (s, 1H), 7.73 (m, 4H), 7.58 (m, 2H), 7.43 (d, J = 6 Hz, 1H), 7.09 (d, J = 6 Hz, 1H), 7.03 (s, 1H), 4.18 (br, 2H), 3.88 (br, 2H), 3.66 (m, 12H), 3.51 (br, 2H), 3.31 (s, 3H) ppm. ^{13}C NMR (125 MHz, $CDCl_3$): δ = 192.02, 157.41, 141.28, 137.17, 135.55, 134.41, 129.97, 129.65,

128.69, 128.35, 127.53, 127.33, 126.37, 124.76, 119.68, 106.55, 71.74, 70.66, 70.46, 70.29, 69.55, 69.19, 67.34, 58.82 ppm. IR: ν (cm^{-1}) = 2874, 1698, 1630, 1607, 1498, 1452, 1388, 1364, 1302, 1258, 1207, 1168, 1094, 1001, 972, 908, 835, 809, 727, 691, 646, 596, 529. HRMS-ESI(+): Calc = 506.2286 $[M+H]^+$, Found = 506.2297 ($C_{28}H_{31}N_3O_6$).

Compound Probe-7. Compound **7a** was prepared according to the literature procedure.[37]

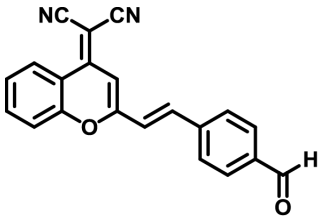

Compound **7a** (0.12 g, 0.57 mmol, 1.0 equiv.) and 4-hydroxymethylbenzaldehyde[38] (0.09 g, 0.62 mmol, 1.1 equiv.) were dissolved in 6 mL of acetonitrile. A 170 μL solution of piperidine was added and the mixture refluxed under air for 16 h. The reaction was then cooled to RT and the organic products were extracted into CH_2Cl_2 (3×20 mL). The organic layers were combined and washed with 1 N HCl and brine. The organic layer was then dried over Na_2SO_4, filtered, and the solution was evaporated to dryness. The crude product **7b** (0.08 g, 0.23 mmol, 1 equiv.) was oxidized by stirring with Dess Martin reagent (0.20 g, 0.47 mmol, 2 equiv.) at RT for 2 h in CH_2Cl_2. The reaction was quenched by the addition of saturated sodium thiosulfate solution and the organic products were extracted into CH_2Cl_2 (3×20 mL). The organic layers were combined and washed with saturated sodium bicarbonate solution and brine. The organic layer was then dried over Na_2SO_4, filtered, and then the solution was evaporated to dryness. The crude material was purified by silica gel column chromatography (100% CH_2Cl_2) to afford the desired product as a yellow solid (43%,

0.03 g). ^{1}H NMR (600 MHz, $CDCl_3$): 10.05 (s, 1H), 8.91 (d, J = 12 Hz, 1H), 7.94 (d, J = 12 Hz, 2H), 7.75 (m, 3H), 7.64 (d, J = 12 Hz, 1H), 7.56 (d, J = 12 Hz, 1H), 7.47 (t, J = 6 Hz, 1H), 6.96 (s, 1H), 6.94 (s, 1H) ppm. *Note: Compound **Probe-7** is too insoluble in organic solvents to obtain its ^{13}C NMR spectrum.* IR: ν (cm^{-1}) = 3073, 2823, 2720, 2211, 2199, 1695, 1633, 1600, 1557, 1512, 1481, 1455, 1409, 1390, 1341, 1323, 1303, 1266, 1227, 1209, 1140, 1128, 975, 953, 933, 867, 846, 812, 796, 771, 745, 707, 693, 676, 667, 547, 531. HRMS-CI(+): Calc = 324.0899 $[M]^+$, Found = 324.0900 ($C_{21}H_{12}N_2O_2$).

2.4.3. Procedure for Non-Biological Transfer Hydrogenation Studies

Bodipy-CHO (0.02 mL from 76.6 mM stock in DMSO, 1.53 μmol, 1.0 equiv.), NADH (2.5 mg, 3.28 μmol, 2.1 equiv.), and iridium catalyst **Ir1** (0.05 mL from 0.6 mM stock solution in ^{t}BuOH, 0.03 μmol, 2 mol%.) were combined in total 1.6 mL of H_2O/^{t}BuOH/DMSO (63:36:1) in a 20 mL scintillation vial. The final concentration of the **Ir1** was 18.8 μM. The vial was sealed with a screw cap and the reaction mixture was stirred at 37°C for 24 h. After 24 h, the organic products were extracted into DCM. The organic layer was separated, dried over Na_2SO_4, filtered, and then evaporated to dryness under vacuum. The NMR spectrum of the isolated material shows that approximately 20% of **Bodipy-CHO** had converted to **Bodipy-OH** (Figure 2).

2.4.4. Procedure for Fluorescence Studies in the Cuvette

A stock solution containing 30 μM of **Bodipy-CHO** and 100 μM of NADH was prepared in ^{t}BuOH/H_2O (1:4). A 3.0 mL aliquot of this solution was transferred to a quartz cuvette and the initial fluorescence spectrum was recorded at RT. A 20 μL solution of 4.5 mM iridium catalyst in ^{t}BuOH was added to the cuvette to yield a final catalyst concentration

of 30 μM. This solution was left unstirred at RT under air and the fluorescence spectra were recorded every fifteen minutes for the first hour and then every hour for an additional five hours. The quantum yield for **Bodipy-OH** was determined to be 0.61, whereas the quantum yield for **Bodipy-CHO** was reported to be 0.26.[24]

2.4.5. Cell Cytotoxicity Studies

Fluorescent probes (**Bodipy-CHO** and **Bodipy-OH**): NIH-3T3 mouse fibroblast cells (10000 cells/well) were seeded in a 96-well plate and allowed to attach overnight in a 5% CO_2 humidified incubator. Solid **Bodipy-CHO** or **Bodipy-OH** was pre-dissolved in 1.5 mL of DMSO to give a 10 mM stock solution and then diluted using commercial cell growth media (Dulbecco's Modified Eagle Medium (DMEM) supplemented with 5% fetal bovine serum (FBS) and 1% anti- biotic/anti-mycotic solution (100×)) to give a series of different concentrations (0.1, 1, 5, 25, 100, and 500 μM). The cells were then treated with the **Bodipy** solutions (6 wells per concentration) for 3 h. The solutions were removed by pipette and the cells were washed with fresh DMEM twice before adding DMEM containing 3-(4,5-dimethylthiazol-2-yl)-5-(3-carboxymethoxyphenyl)-2-(4-sulfophenyl)-2H-tetrazolium (MTS) (2 mL MTS/8 mL DMEM).

After 1 h, the absorbance of the 96-well plate was measured at 490 nm to determine the amount of purple formazan complex formed. Cell viability was considered to be proportional to the absorbance of the wells. Control measurements show that the **Bodipy** probes have negligible absorption at 490 nm. The absorbance value of the wells containing solutions of MTS (background) was subtracted from those of the wells containing treated and control cells. Percentage cell viability was calculated using the

following equation: ($A_{conc}/A_{control}$)×100%, where A_{conc} is the absorbance at a specific probe concentration and $A_{control}$ is the absorbance of the untreated cells sample. The cell viability data were fit to a single exponential decay function and the IC_{50} value was extracted from this fit at 50% cell viability.

Iridium Complexes (**Ir1**): NIH-3T3 mouse fibroblast cells (10000 cells/well) were seeded in a 96-well plate and allowed to attach overnight in a 5% CO_2 incubator. The iridium complex was pre-dissolved in 1.5 mL of DMSO to give a 10 mM stock solution and then diluted using commercial cell growth media (Dulbecco's Modified Eagle Medium (DMEM) supplemented with 5% fetal bovine serum (FBS) and 1% anti-biotic/anti-mycotic solution (100×) to give a series of different concentrations (0.1, 1, 5, 25, 100, 500 μM). The cells were then treated with the **Ir1** solutions (6 wells per concentration) for 3 h. The solutions were removed by pipette and the cells were washed with fresh DMEM twice before adding DMEM containing 3-(4,5-dimethylthiazol-2- yl)-5-(3-carboxymethoxyphenyl)-2-(4-sulfophenyl)-2H-tetrazolium (MTS) (2 mL MTS /8 mL DMEM).

After 1 h, the absorbance of the 96-well plate was measured at 490 nm to determine the amount of purple formazan complex formed. Cell viability was considered to be proportional to the absorbance of the wells. Control measurements show that the iridium complexes do not absorb at 490 nm. The absorbance value of the wells containing solutions of MTS (background) was subtracted from those of the wells containing treated and control cells. Percentage cell viability was calculated using the following equation: ($A_{conc}/A_{control}$)×100%, where A_{conc} is, the absorbance at a specific Ir complex concentration

and $A_{control}$ is the absorbance of the untreated cells sample. The cell viability data were fit to a single exponential decay function and the IC_{50} value was extracted from this fit at 50% cell viability.

2.4.6. Fluorescence Confocal Microscopy Imaging Studies

Iridium Catalyst Activity: NIH-3T3 cells were cultured at 37°C under a 5% CO_2 humidified atmosphere in Dulbecco's Modified Eagle Medium (DMEM) supplemented with 10% fetal bovine serum (FBS) and 1% anti-biotic/anti-mycotic solution (100×). For live cell imaging, cells were plated in μ-Slide 8-well plates (IBIDI) in 200 μL of DMEM in each well. After overnight cell growth, the medium was removed and two of the eight wells (#1–2) were replaced with 30 μM **Bodipy-OH** solution in DMEM (diluted from 10 mM stock in DMSO). The other six wells (#3–8) were replaced with 30 μM **Bodipy-CHO** solution in DMEM (diluted from 10 mM stock in DMSO). After an incubation time of 4 h (37 °C, 5% CO_2), the growth solutions were removed. All of the cells were rinsed with fresh DMEM (2×200 μL each well). 200 μL DMEM solutions containing 20 μM of DMSO were added to each of the **Bodipy-OH** treated wells (#1–2) and two of the **Bodipy-CHO** (#3–4) treated wells as controls. Two of the **Bodipy-CHO** treated wells (#5–6) were then incubated with 200 μL of 20 μM catalyst **Ir1** and two of the **Bodipy-CHO** treated wells (#7–8) were incubated with 200 μL of 20 μM catalyst **Ir2** solution in DMEM (diluted from 10 mM stock solution in DMSO) for 2 h before images were acquired. Similar procedures were used for cell imaging studies using the **Ir3** complex and $IrCl_3$ salt.

All microscope operations and image processing were conducted using Nikon's NIS-

Elements software. The gain value for the laser was determined using the **Bodipy-OH** treated sample and was kept fixed for the acquisition of all images (other acquisition parameters: 512×512 pixel image size, 2.2 μs scan rate**,** optimized z-stack size). Fluorescence image quantification was performed using the program ImageJ by using the formula: corrected total cell fluorescence (CTCF) = [integrated fluorescence density] – [area of selected cell × mean fluorescence of background]. The background fluorescence was calculated by taking the average of four different background regions in a single image. The CTCF was measured for six cells per well. Each set of imaging experiments was performed in triplicate, giving a total of six fluorescence measurements (3 independent experiments × 2 identically treated wells per experiment). The final fold-change in fluorescence is the average value obtained from the three independent experiments relative to that of the **Bodipy-CHO**-only treated cell groups.

Iridium Catalyst Activity in the Presence of Pyruvate: NIH-3T3 cells were cultured at 37°C under a 5% $_{CO2}$ humidified atmosphere in Dulbecco's Modified Eagle Medium (DMEM) supplemented with 10% fetal bovine serum (FBS) and 1% anti-biotic/anti-mycotic solution (100×). For live cell imaging, cells were plated in μ-Slide 8-well plates (IBIDI) in 200 μL of DMEM in each well. After incubation overnight, the cell growth medium was removed and two of the wells (#1–2) were replaced with 30 μM **Bodipy-OH** solution in DMEM (diluted from 10 mM stock solution in DMSO) and six of the wells (#3–8) were replaced with 30 μM **Bodipy-CHO** solution in DMEM (diluted from 10 mM stock solution in DMSO). After an incubation time of 4 h (37 °C, 5% CO_2), the cell growth solutions were removed and all of the cells were rinsed with fresh DMEM

(2×200 μL for each well). DMEM containing 20 μM of DMSO were added (200 μL/well) to the **Bodipy-OH** treated wells (#1–2) and two the **Bodipy-CHO** treated wells (#3–4) as controls. Two of the **Bodipy-CHO** treated wells (#5–6) were then charged with 20 μM **Ir1** (diluted from 10 mM stock solution in DMSO) and the other two **Bodipy-CHO** treated wells (#7– 8) were charged with 20 μM catalyst **Ir1** *and* 10 mM sodium pyruvate solution in DMEM (diluted from 100 mM stock solution, commercially available) for 2 h before images were acquired. The same imaging procedures were used as described in the section above.

2.4.7. Inductively Coupled Plasma-Mass Spectrometry (ICP-MS) Iridium Analysis

NIH-3T3 cells were cultured in 100 mm tissue culture plates (Corning) at 37°C under a 5% CO_2 atmosphere. After 100% confluence was achieved, the cells were incubated with 20 μM of **Ir1** or **Ir2** for 2 h in DMEM (diluted from 10 mM stock solution in DMSO). After 2 h of incubation the catalyst solutions were removed and the cells were rinsed twice with DMEM. The adhered cells were detached by treatment with trypsin and counted using a BIO-RAD TC10 automated cell counter. The sample was then centrifuged and the supernatant was removed. The cell pellet was washed an additional time with phosphate buffered saline (PBS), centrifuged, and then the supernatant was removed. The samples were digested with 0.5 mL of 60% HNO_3 at RT overnight. Each sample was diluted with 6.5 mL of H_2O to obtain 5% HNO_3 sample solutions. The cloudy solutions were centrifuged and the clear supernatant was separated and used for analysis by ICP- MS. The total iridium content per cell was calculated using the solution volume and cell density from each sample preparation.

2.4.8. NMR Spectroscopic Studies: Conversion of Pyruvate to Lactate

Solid NADH (76.3 mg, 0.1 mmol, 2 equiv.) was added to sodium pyruvate (0.5 mL of 100 mM, 1 equiv.) in D_2O (0.5 mL). A 99 μL solution of 10 mM **Ir1** in DMSO was added to the mixture to achieve a final 0.9 mM concentration of the iridium complex. The NMR spectra of the reaction mixture were recorded immediately after mixing and then at 2.0 and 4.5 h. The reaction mixture was stirred at 37°C. In a separate control experiment, 0.23 mL of 10 mM **Ir1** (1.29 mg, 2.3 μmol, 0.02 equiv.) was added to a 0.12 M solution of sodium lactate (0.77 mL) and the NMR spectra were recorded immediately after mixing and then 2.0 and 4.5 h after to determine if there is coordination of lactate to the iridium center. The reaction mixture was stirred at 37°C.

2.4.9. Fluorescence Analysis of Lysate from Cell Experiments

NIH-3T3 cells were cultured in three separate 100 mm tissue culture plates (Corning) at 37°C under a 5% CO_2 humidified atmosphere and allowed to reach 100% confluence. One of the dish (#1) was treated with 30 μM of **Bodipy-OH** and the other two (#2–3) were incubated with 30 μM of **Bodipy-CHO** for 4 h in DMEM. After an incubation time of 4 h (37 °C, 5% CO_2), the solutions were removed and the adhered cells were rinsed twice with DMEM. A solution of 20 μM DMSO in DMEM was added to dishes #1 and #2 as blank controls. To dish #3, a solution containing 20 μM of complex **Ir1** (diluted from 10 mM stock solution in DMSO) was added. After a 2 h incubation period, the cell growth media were removed and the adhered cells were washed once with DMEM followed by detachment using trypsin. The cell density of each group (dishes #1–3) was determined by treating the cells with Trypan Blue and then counted using a BIO-RAD TC10 automated cell counter. Finally, the cells were washed with PBS, centrifuged, and

then the supernatant was removed by pipette. A 1.0 mL solution of ice-cold water/acetonitrile/methanol (1:2:2) was added to the cell pellets. The cell suspension was transferred to a glass autosampler vial and vortex for 5 min. The samples were snap frozen by immersing in liquid nitrogen and then thawing to RT (3 times per sample). Each sample was transferred to a 1.5 mL centrifuge tube and centrifuged at 16000 xg for 15 min at 4°C. A 800 μL solution of the supernatant was collected and diluted to a total volume of 3.0 mL with water/acetonitrile/methanol (1:2:2). The fluorescence spectrum of each lysate solution was then measured (λ_{ex} = 480 nm). The integrated fluorescence at 490–650 nm was normalized by dividing it by the corresponding cell density.

Table 2. Fluorescence quantification of cell lysate.

		Cell Density[a] (cell/mL)	Total Cells[b]	Integrated Fluorescence (490-650 nm)	Fluorescence Per Cell[c]	Fold-Change[d]
Exp. 1	**Bodipy-CHO**	3.20E+05	3.04E+05	1.05E+08	3.45E+02	1.00
	Bodipy-OH	6.58E+04	6.25E+04	7.63E+07	1.22E+03	3.53
	Bodipy-CHO/Ir1	1.40E+05	1.33E+05	8.46E+07	6.36E+02	1.84
Exp. 2	**Bodipy-CHO**	8.60E+04	8.17E+04	8.94E+06	1.09E+02	1.00
	Bodipy-OH	9.11E+04	8.65E+04	2.98E+07	3.44E+02	3.15
	Bodipy-CHO/Ir1	5.23E+04	4.97E+04	9.99E+06	2.01E+02	1.84
Exp. 3	**Bodipy-CHO**	4.36E+05	4.14E+05	5.86E+06	1.42E+01	1.00
	Bodipy-OH	2.58E+05	2.45E+05	1.26E+07	5.14E+01	3.63
	Bodipy-CHO/Ir1	1.54E+05	1.46E+05	6.95E+06	4.76E+01	3.36
				Average	**Bodipy-CHO**	1.00
					Bodipy-OH	3.44±0.21
					Bodipy-CHO/Ir1	2.35±0.72

[a]Cell density was measured using a Bio-RAD TC10 automated cell counter and trypan blue. [b]Total cells was calculated using [cell density x total volume]. [c]Fluorescence per cell was calculated using [fluorescence (490–650 nm)/total cells]. [d]Fold change was calculated using [fluorescence per cell of a particular treatment group/fluorescence per cell for **Bodipy-CHO**].

2.5. References

1. Dobereiner, G. E.; Crabtree, R. H. *Chem. Rev.* **2010**, *110*, 681-703.
2. Wang, D.; Astruc, D. *Chem. Rev.* **2015**, *115*, 6621-6686.
3. Robertson, A.; Matsumoto, T.; Ogo, S. *Dalton Trans.* **2011**, *40*, 10304-10310.
4. Leiva, C.; Lo, H. C.; Fish, R. H. *J. Organomet. Chem.* **2010**, *695*, 145-150.
5. Lo, H. C.; Fish, R. H. *Angew. Chem. Int. Ed.* **2002**, *41*, 478-481.
6. Lo, H. C.; Leiva, C.; Buriez, O.; Kerr, J. B.; Olmstead, M. M.; Fish, R. H. *Inorg. Chem.* **2001**, *40*, 6705-6716.
7. Ogo, S.; Makihara, N.; Watanabe, Y. *Organometallics* **1999**, *18*, 5470-5474.
8. Wu, X.; Liu, J.; Li, X.; Zanotti-Gerosa, A.; Hancock, F.; Vinci, D.; Ruan, J.; Xiao, J. *Angew. Chem. Int. Ed.* **2006**, *45*, 6718-6722.
9. Ruppert, R.; Herrmann, S.; Steckhan, E. *J. Chem. Soc., Chem. Commun.* **1988**, 1150-1151.
10. Betanzos-Lara, S.; Liu, Z.; Habtemariam, A.; Pizarro, A. M.; Qamar, B.; Sadler, P. J. *Angew. Chem. Int. Ed.* **2012**, *51*, 3897-3900.
11. Maenaka, Y.; Suenobu, T.; Fukuzumi, S. *J. Am. Chem. Soc.* **2012**, *134*, 367-374.
12. Heiden, Z. M.; Rauchfuss, T. B. *J. Am. Chem. Soc.* **2007**, *129*, 14303-14310.
13. Ngo, A. H.; Ibañez, M.; Do, L. H. *ACS Catal.* **2016**, *6*, 2637-2641.
14. Sasmal, P. K.; Carregal-Romero, S.; Parak, W. J.; Meggers, E. *Organometallics* **2012**, *31*, 5968-5970.
15. Letko, C. S.; Heiden, Z. M.; Rauchfuss, T. B. *Eur. J. Inorg. Chem.* **2009**, *2009*, 4927-4930.
16. Abura, T.; Ogo, S.; Watanabe, Y.; Fukuzumi, S. *J. Am. Chem. Soc.* **2003**, *125*, 4149-4154.
17. Okamoto, Y.; Köhler, V.; Ward, T. R. *J. Am. Chem. Soc*. **2016**, *138*, 5781-5784.
18. Liu, S.; Rebros, M.; Stephens, G.; Marr, A. C. *Chem. Commun*. **2009**, 2308-2310.
19. Köhler, V.; Wilson, Y. M.; Dürrenberger, M.; Ghislieri, D.; Churakova, E.; Quinto, T.; Knörr, L.; Haüssinger, D.; Hollmann, F.; Turner, N. J.; Ward, T. R. *Nat. Chem*. **2013**, *5*, 93-99.
20. McFarland, J. M.; Francis, M. B. *J. Am. Chem. Soc*. **2005**, *127*, 13490-13491.
21. Hsu, H.-T.; Trantow, B. M.; Waymouth, R. M.; Wender, P. A. *Bioconjugate Chem.*

2016, *27*, 376-382.

22. Liu, Z.; Romero-Canelón, I.; Qamar, B.; Hearn, J. M.; Habtemariam, A.; Barry, N. P. E.; Pizarro, A. M.; Clarkson, G. J.; Sadler, P. J. *Angew. Chem. Int. Ed.* **2014**, *53*, 3941-3946.
23. Komatsu, H.; Shindo, Y.; Oka, K.; Hill, J. P.; Ariga, K. *Angew. Chem. Int. Ed.* **2014**, *53*, 3993-3995.
24. Yue, Y.; Guo, Y.; Xu, J.; Shao, S. *New J. Chem*. **2011**, *35*, 61-64.
25. Pastore, A.; Alisi, A.; di Giovamberardino, G.; Crudele, A.; Ceccarelli, S.; Panera, N.; Dionisi-Vici, C.; Nobili, V. *Int. J. Mol. Sci.* **2014**, *15*, 21202-21214.
26. Seshadri, S.; Beiser, A.; Selhub, J.; Jacques, P. F.; Rosenberg, I. H.; D'Agostino, R. B.; Wilson, P. W. F.; Wolf, P. A. *New Engl. J. Med.* **2002**, *346*, 476-483.
27. Yang, L.; Bose, S.; Ngo, A. H.; Do, L. H. *ChemMedChem* **2017**, *12*, 292-299.
28. Barrett, S. M.; Pitman, C. L.; Walden, A. G.; Miller, A. J. M. *J. Am. Chem. Soc*. **2014**, *136*, 14718-14721.
29. Murata, K.; Ikariya, T.; Noyori, R. *J. Org. Chem.* **1999**, *64*, 2186-2187.
30. Zhao, Y.; Wang, A.; Zou, Y.; Su, N.; Loscalzo, J.; Yang, Y. *Nat. Protoc*. **2016**, *11*, 1345-1359.
31. McFarland, J. M.; Francis, M. B. *J. Am. Chem. Soc.* **2005**, *127*, 13490-13491.
32. Guo, H.-M.; Tanaka, F. *J. Org. Chem.* **2009**, *74*, 2417-2424.
33. Kirpichënok, M. A.; Baukulev, V. M.; Karandashova, L. A.; Grandberg, I. I. *Chem. Heterocycl. Compd.* **1991**, *27*, 1193-1199.
34. Almodares, Z.; Lucas, S. J.; Crossley, B. D.; Basri, A. M.; Pask, C. M.; Hebden, A. J.; Phillips, R. M.; McGowan, P. C. *Inorg. Chem.* **2014**, *53*, 727-736.
35. Youinou, M.-T.; Ziessel, R. *J. Organomet. Chem.* **1989**, *363*, 197-208.
36. Kang, J. W.; Moseley, K.; Maitlis, P. M. *J. Am. Chem. Soc.* **1969**, *91*, 5970-5977.
37. Zhang, X.; Zhang, L.; Liu, Y.; Bao, B.; Zang, Y.; Li, J.; Lu, W. *Tetrahedron* **2015**, *71*, 4842-4845.
38. Loim, N. M.; Kelbyscheva, E. S. *Russ. Chem. Bull.* **2004**, *53*, 2080-2085.

Chapter 2 Appendix

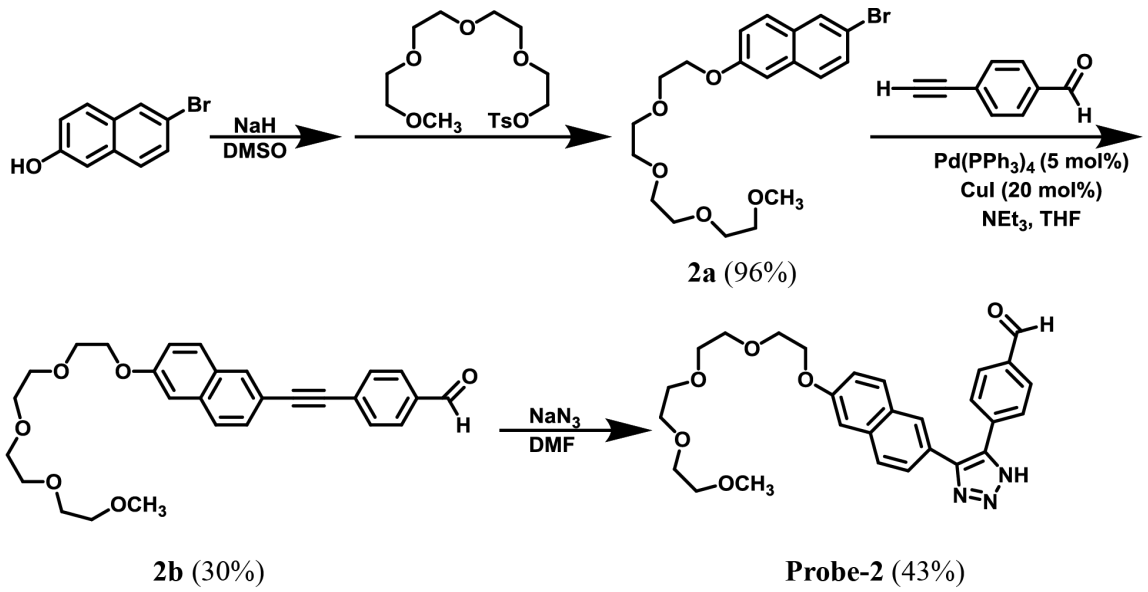

Scheme S1. Synthetic procedure for the preparation of **Probe-2**.

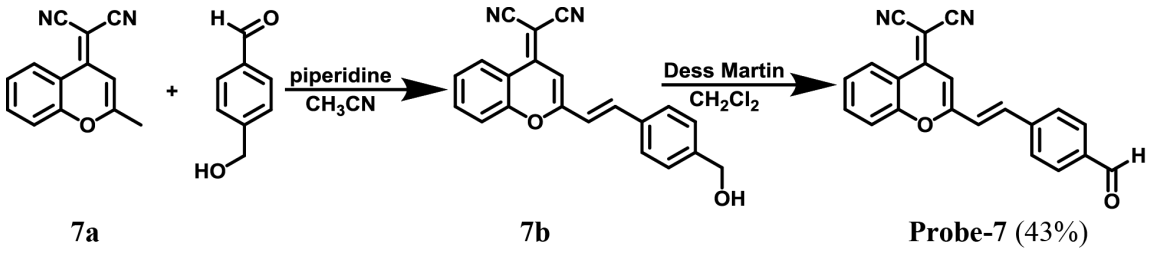

Scheme S2. Synthetic procedure for the preparation of **Probe-7**.

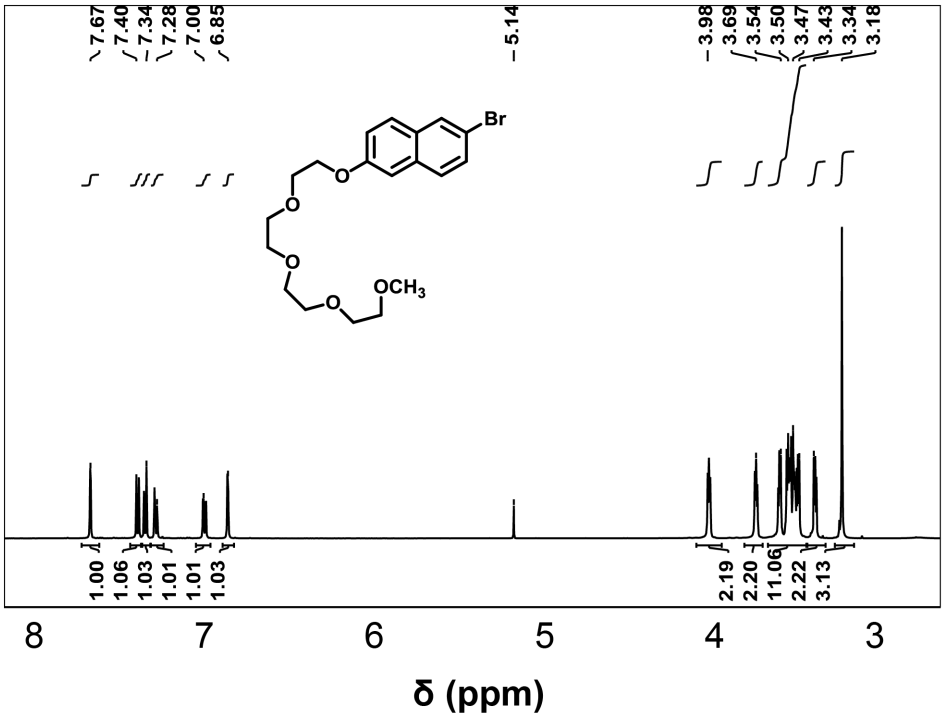

Figure S1. ^{1}H NMR spectrum (600 MHz, $CDCl_3$) of **2a**.

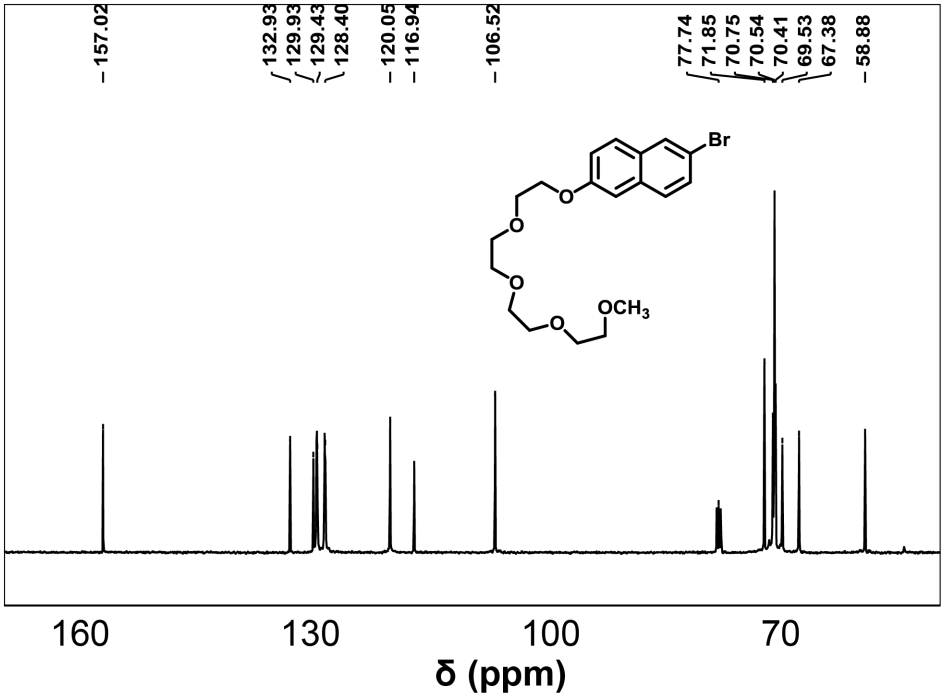

Figure S2. ^{13}C NMR spectrum (125 MHz, $CDCl_3$) of **2a**.

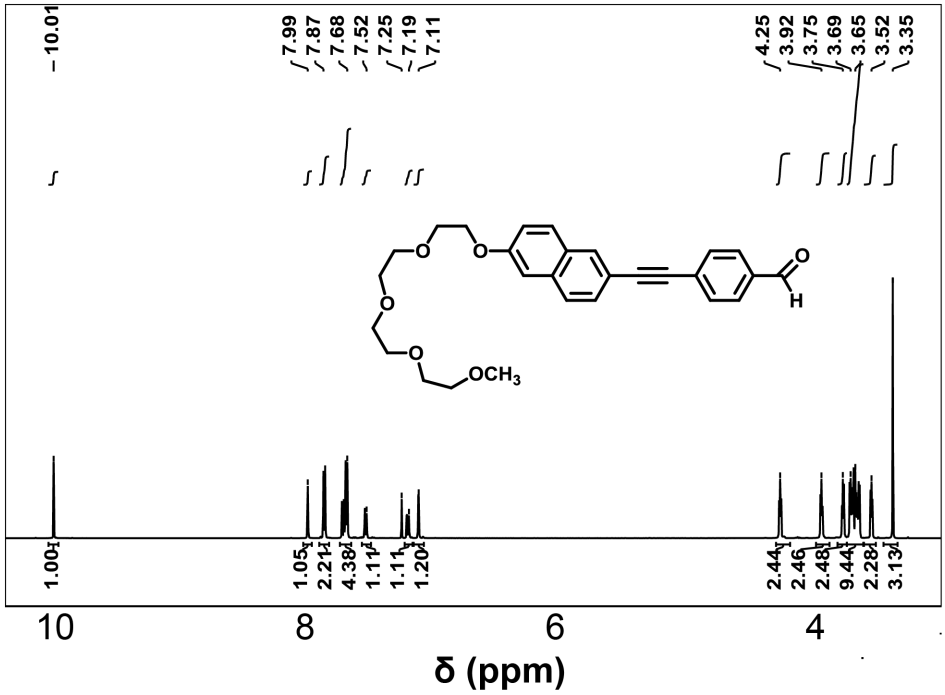

Figure S3. ^{1}H NMR spectrum (600 MHz, $CDCl_3$) of **2b**.

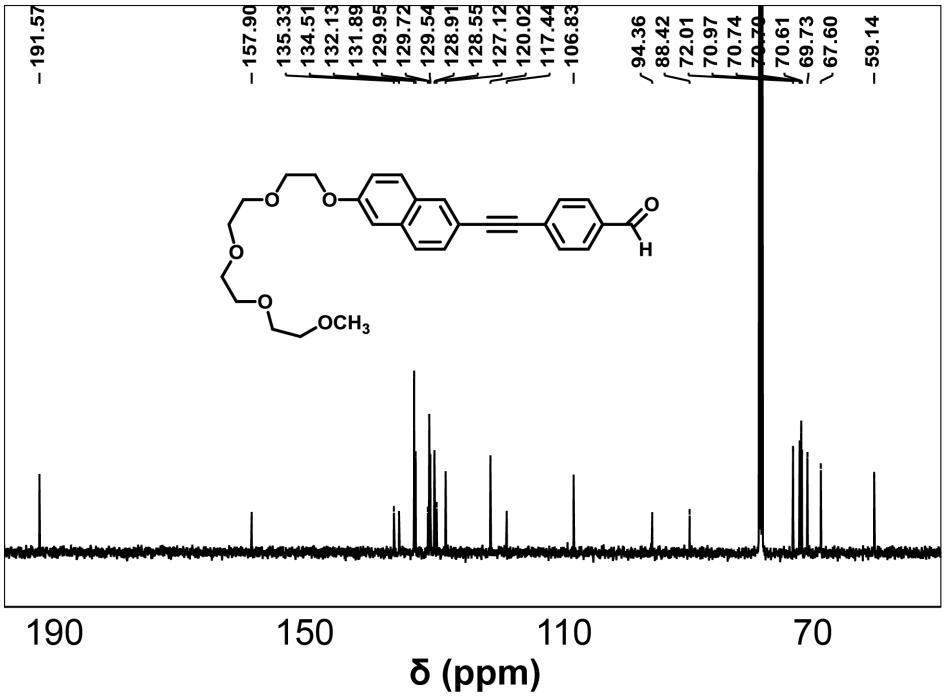

Figure S4. ^{13}C NMR spectrum (125 MHz, $CDCl_3$) of **2b**.

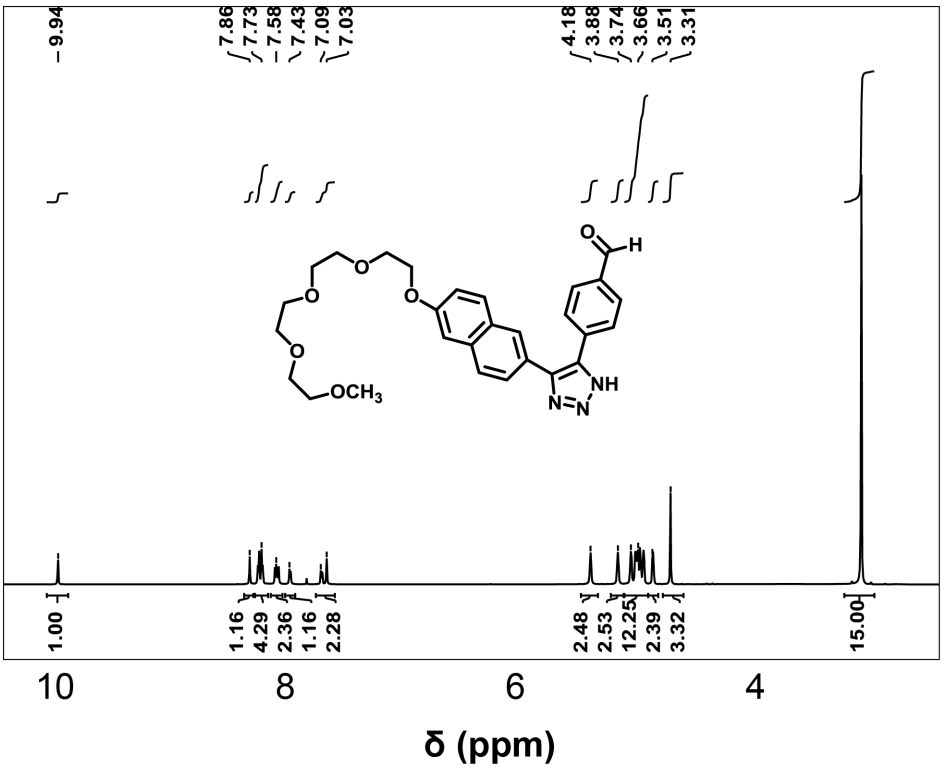

Figure S5. ^{1}H NMR spectrum (600 MHz, $CDCl_3$) of **Probe-2**.

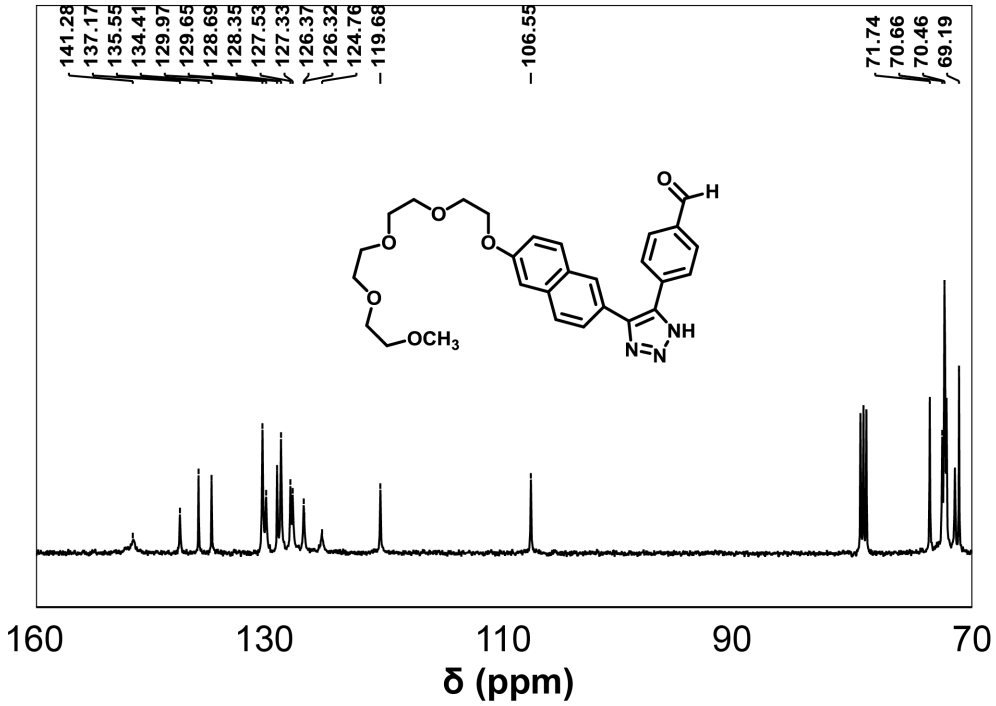

Figure S6. ^{13}C NMR spectrum (125 MHz, $CDCl_3$) of **Probe-2**.

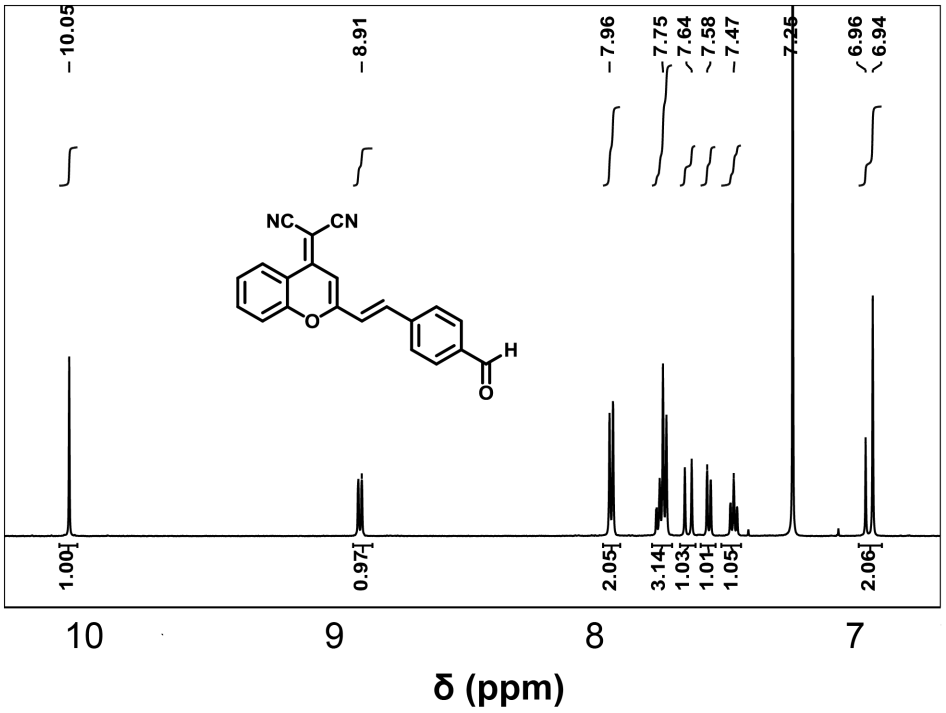

Figure S7. ^{1}H NMR spectrum (600 MHz, $CDCl_3$) of **Probe-7**.

CHAPTER 3. Visualization and Quantification of Intracellular Iridium Transfer Hydrogenation Catalysis in Living Cells

3.1. Introduction

Catalytic efficiency of small molecule intracellular metal catalysts is difficult to quantify inside living cells. Unprotected metal catalysts tend to get deactivated in biological matrix, since they are not protected within protein cavities,[1] thus, in-cellulo catalytic activity is expected to be different from *in-vitro* activity. One of the challenges in quantifying the efficiency of metal catalysts in cells that the chemical analytes of interest are present in very low concentration (< 1 μM), which requires very sensitive analytical instrument to detect.

Mass spectrometry is a common analytical method used to identify small amounts of chemical species because of its low detection limit. Cai and coworkers reported the intracellular efficiency of copper catalyzed azide-alkyne cycloaddition reaction for the first time using LC-ESI-MS.[2] The researchers found that around 18% and 0.8% product were formed on the cell membrane and in the cytosol, respectively, and 75% of cells remained viable after 10 min of reaction. Upon reducing the biothiol concentration by treating cells with *N*-ethylmlamide, the reaction yield in the cytosol was increased to 14%, whereas no change was observed in the reaction yield on the membrane. These results suggest that biothiol deactivation of copper catalyst in one of the major reasons for lower intracellular yield.

Fluorescnece imaging is another powerful method used to detect molecules at low concentrations. Ward and coworkers reported TON for Ir catalyzed transfer hydrogenation reaction in *E. coli* by using a self-immolative substrate (Scheme 1). Their substrate comprises a quinoline group that is attached to an umblliferone fluorophore.

Upon reduction, the non-emissive substrate releases the fluorescent umbelliferone.[3] The intensity of fluorescence from umbelliferone was considered to be proportional to the amount of product formed.

Sadler and coworkers used commercial assay kits to quantify intracellular catalysis. They provided the first example of the enantioselective reduction of pyruvate to D-lactate in cells by osmium catalysts in the presence of external formate.[4] Unlike platinum-based cancer therapies that target DNA, the authors proposed that the Os catalysts could disrupt metabolism in cancer cells. Because glycolysis is upregulated in cancer cells,[5] lactate dehydrogenases (LDH) that catalyze the conversion between pyruvate and lactate using reduced nicotinamide adenine dinucleotide (NADH),[6] is overexpressed in cancer cells.[7,8] The catalytic conversion of pyrivate to lactate using external formate and the Os catalyst was proposed to lower the ability of cancer cells to harness more NAD^+. Since, cancer cells are already under redox stress due to their rapid proliferation, disturbing the delicate redox balance in cancer cells could provide a select way to kill them.[9]

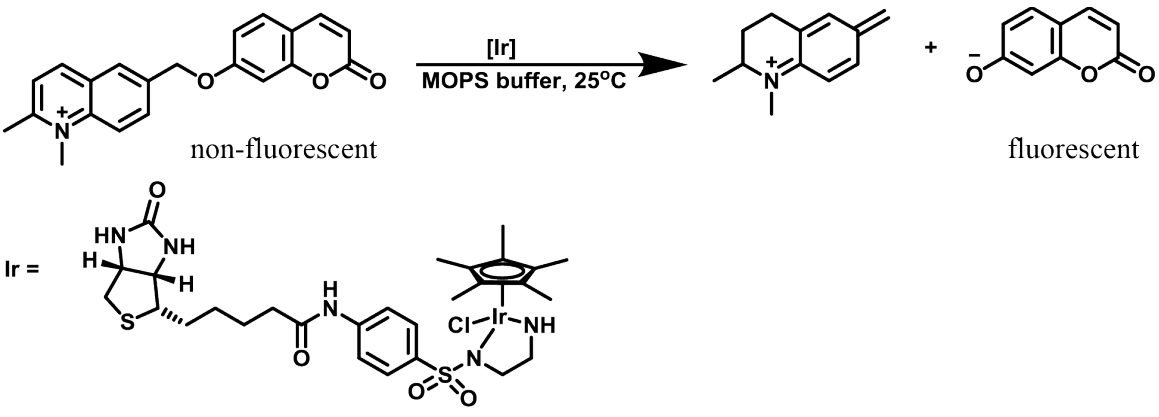

Scheme 1. Transfer hydrogenation of self-immolative substrate by iridium catalyst.

Our research group had reported that reduction of aromatic aldehyde to corresponding alcohol could be achieved in live cells by pentamethylcyclopentadienyl (Cp*) Ir(III) complexes supported by *N*-phenyl-2-pyridinecarboxamidate ligands (**Ir1**).[10] In the present chapter, we describe the preparation of new fluorescent Ir complexes using Bodipy fluorophore. We will use these iridium-probe conjugates to visualize their distribution and accumulation in live cells. The intracellular reaction yields obtained using both fluorescent and non-fluorescent Ir complexes were investigated after carrying out transfer hydrogenation reactions in NIH3T3 cells. LC-ESI-MS was used to quantify the analytes in cell lysate. Several other parameters, such as IC_{50} and cellular uptake, were measured and then the different catalysts were compared.

3.2. Results and Discussion

3.2.1. Synthesis of Fluorogenic Iridium Catalysts

A series of iridium complexes (**Ir1, Ir4, Ir5**) were found to be active as transfer hydrogenation catalysts under physiologically relevant condition.[11] A series of new Ir(III) catalysts (**Ir1'**, **Ir4'**, **Ir5'**), which are the fluorescent analogues of parent catalysts (**Ir1**, **Ir4**, **Ir5**) (Chart 1) were synthesized (Scheme 2). All three new catalysts were characterized by ^{1}H, ^{13}C NMR (Figure S11-S15), and HRMS. These fluorescent catalysts (**Ir1'**, **Ir4'**, **Ir5'**) emit at 520 ± 5 nm upon excitation with 480 nm (Figure 1). The quantum yields of these fluorescent complexes **Ir1'**, **Ir4'**, **Ir5'** were found to be 4.03, 1.52, 2.10%, respectively, when measured relative to a fluorescein standard. The extracellular catalyst activities of these new iridium-bodipy conjugates were tested for the reduction of benzaldehyde to benzyl alcohol using formate and 1 mol% catalyst loading

in THF/H_2O at 37°C for 24 h. We found that **Ir1'**, **Ir4'** and **Ir5'** retained similar *in-vitro* catalytic activity as **Ir1**, **Ir4**, **Ir5**, respectively (Figure 2). **Ir4'** showed the highest activity among the fluorogenic Ir catalysts, which is consistent with our results from studies of the non-fluorescent catalysts.[11] However, the intracellular activities of these iridium complexes are expected to be different from those in the reaction flask since additional factors, such as, cellular uptake, cytotoxicity, and catalyst poisoning, could impact catalyst performance.

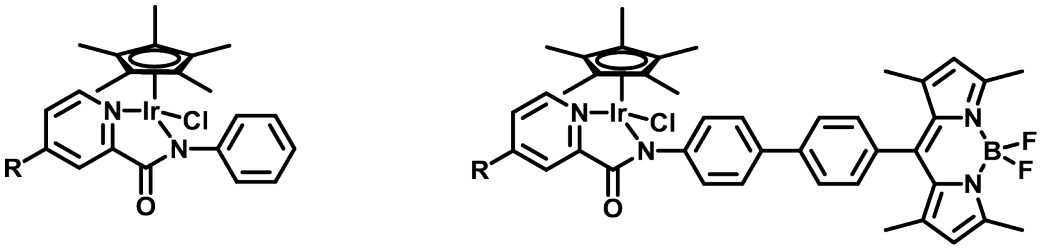

R = H (**Ir1**)
R = NMe_2 (**Ir4**)
R = CF_3 (**Ir5**)

R = H (**Ir1'**)
R = NMe_2 (**Ir4'**)
R = CF_3 (**Ir5'**)

Chart 1. Structure of iridium complexes used in this study.

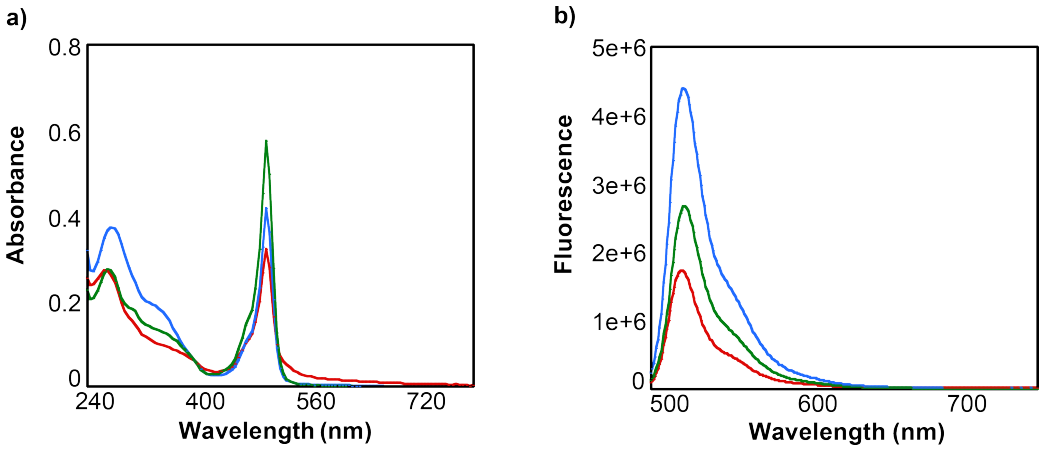

Figure 1. a) UV-Vis and b) Fluorescence Spectra (λ_{ex} = 480 nm, collection: 490-750 nm, no filter) of **Ir1'** (10 μM, red), **Ir4'** (10 μM, blue), and **Ir5'** (10 μM, green) in 1:4 $^tBuOH/H_2O$.

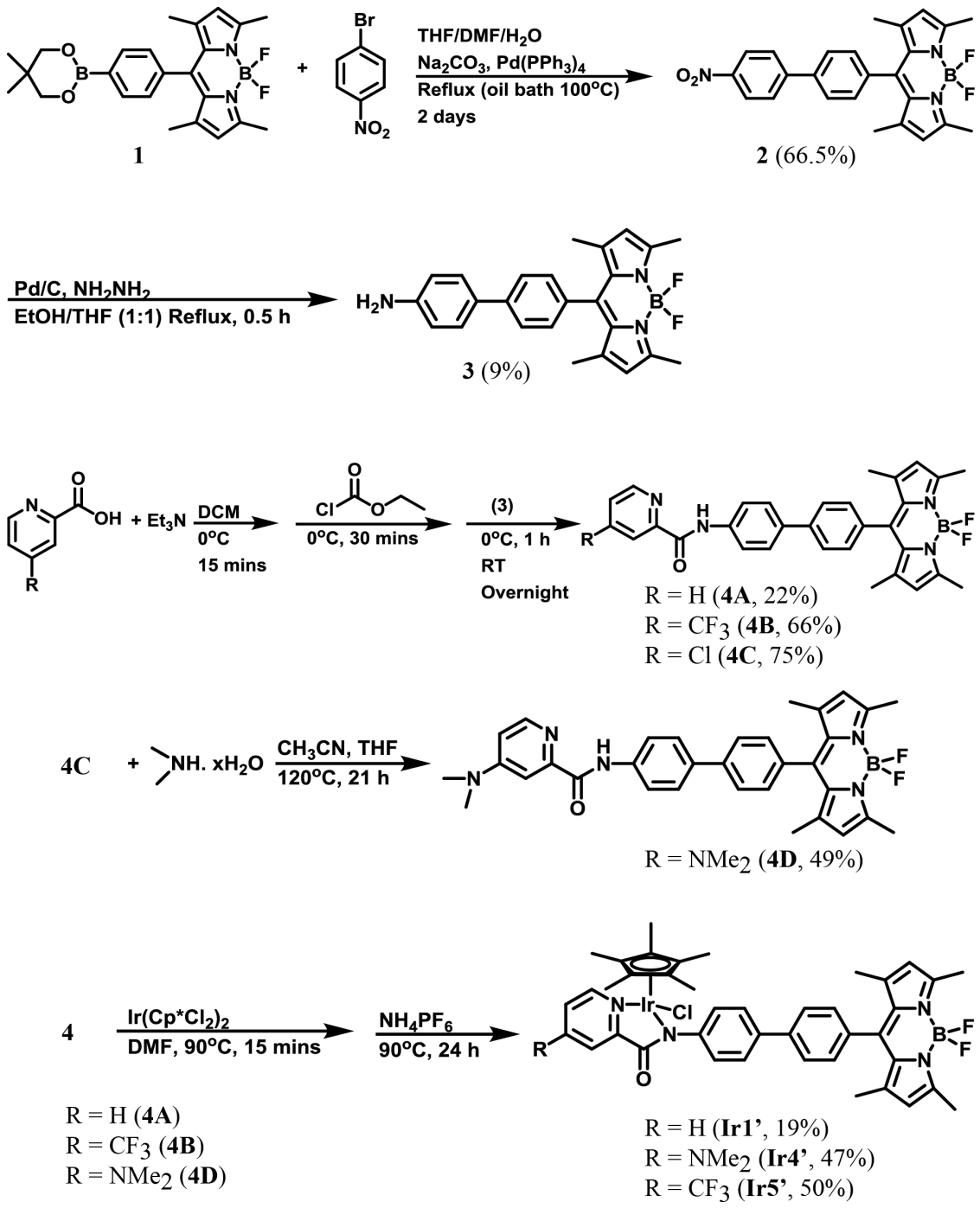

Scheme 2. Synthesis of catalysts **Ir1'**, **Ir4'**, **Ir5'**.

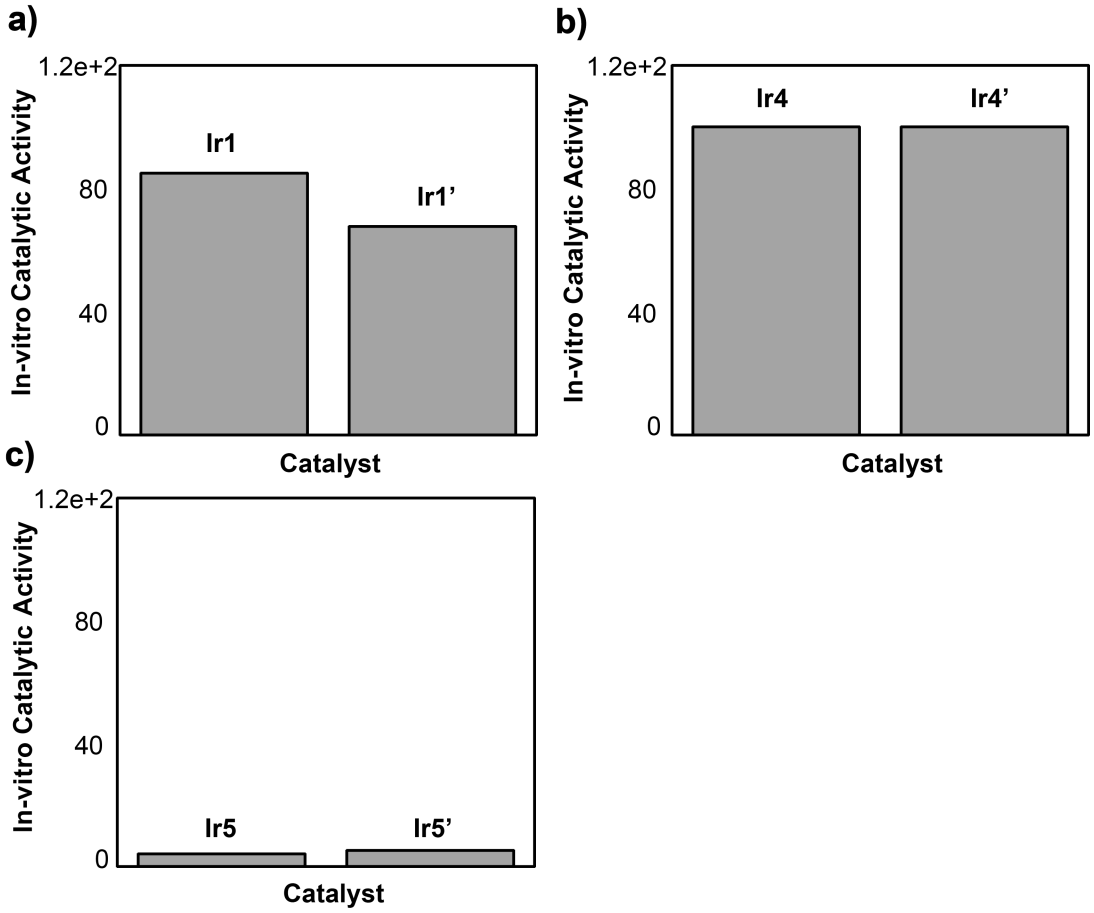

Figure 2. Hydrogenation of benzaldehyde by complexes a) **Ir1** and **Ir1'** b) **Ir4** and **Ir4'** c) **Ir5** and **Ir5'** using HCOONa as the hydride donor. Reaction conditions: a) benzaldehyde (60 μmol), HCOONa (180 μmol), Ir complex (0.60 μmol, 172 μM), H_2O/THF (2.2:1, 3.5 mL), 37 °C, 24 h; b) benzaldehyde (60 μmol), HCOONa (180 μmol), Ir complex (0.60 μmol, 142 μM), H_2O/THF (1.5:1, 4.2 mL), 37 °C, 24 h; c) benzaldehyde (60 μmol), HCOONa (180 μmol), Ir complex (0.60 μmol, 125 μM), H_2O/THF (1:1, 4.8 mL), 37 °C, 24 h. The reaction yields were determined by gas chromatography analysis using biphenyl as an internal standard. Difference in concentrations of catalysts is due their different solubility.

3.2.2. Cell Membrane Permeability of Iridium Catalysts

The ability of a catalyst to cross the cell membrane is an important catalyst property. The cell permeability of the iridium complexes (**Ir1**, **Ir4**, **Ir5**, **Ir1'**, **Ir4'**, **Ir5'**) was determined by measuring the Ir concentration in cells by ICP-MS. To perform these measurements, NIH3T3 cells that were incubated with Ir complexes were lysed with 60% HNO_3 (Figure 3). Because Ir is not a biologically abundant metal ion, the presence of Ir inside cells would indicate the successful cellular entry of the iridium complexes. Cells that were treated with 5 μM of **Ir1**, **Ir4**, **Ir5** catalysts for 2 h retained on average 42, 21, and 104 ng of iridium per 10^6 cells, respectively. Surprisingly, the Ir-bodipy complexes showed a different trend than their parent complexes. Trifluoromethyl substituted catalyst **Ir5** showed maximum accumulation whereas trifluoromethyl substituted **Ir5'** showed the lowest accumulation. Cells that were treated with 5 μM of **Ir1'**, **Ir4'**, **Ir5'** catalysts for 2 h retained on average 179, 111, and 8 ng of iridium per 10^6 cells, respectively. The cellular uptake for **Ir1** and **Ir4** were enhanced by the attachment of fluorophores whereas, the opposite effect was observed for **Ir5**. The Ir complexes reported by Sadler, $[(\eta^5\text{-Cp*})\text{Ir(phen)-Cl}]^+$ (**Ir6**), $[(\eta^5\text{-Cp}^{xph})\text{Ir(phen)-Cl}]^+$ (**Ir7**), $[(\eta^5\text{-Cp}^{xbiph})\text{Ir(phen)-Cl}]^+$ (**Ir8**) (Chart 2) retained 3.9, 23.5, and 88.8 ng of iridium per 10^6 cells, respectively when treated with 5 μM of corresponding iridium complexes for 24 h.[12]

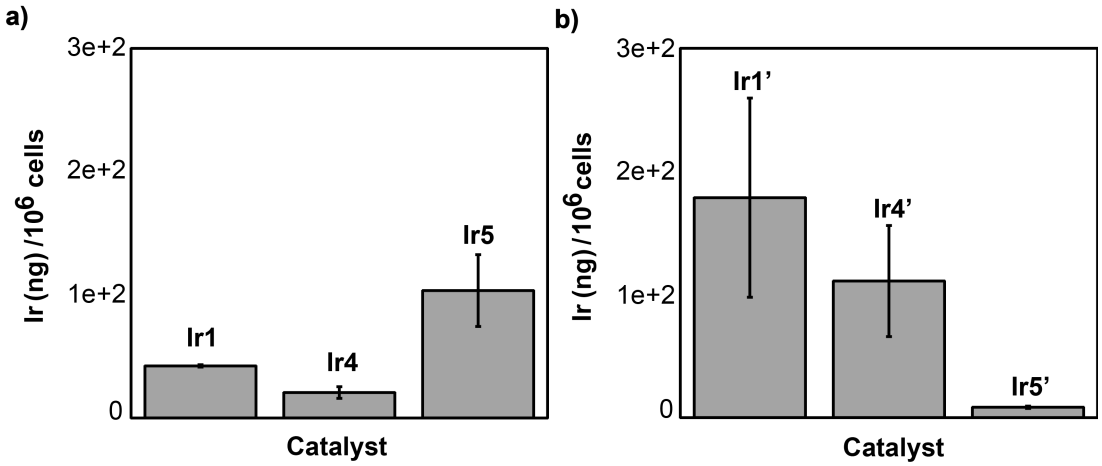

Figure 3. Cellular Uptake of a) **Ir1**, **Ir4**, and **Ir5** b) **Ir1', Ir4'** and **Ir5'** Reaction conditions: NIH-3T3 Cells were treated with 5 μM of iridium catalyst (diluted from 5 mM stock solution in DMSO) for 2 h. ICP-MS analysis was performed on cell lysate of the treated cells. The values shown are the average values from three separate runs.

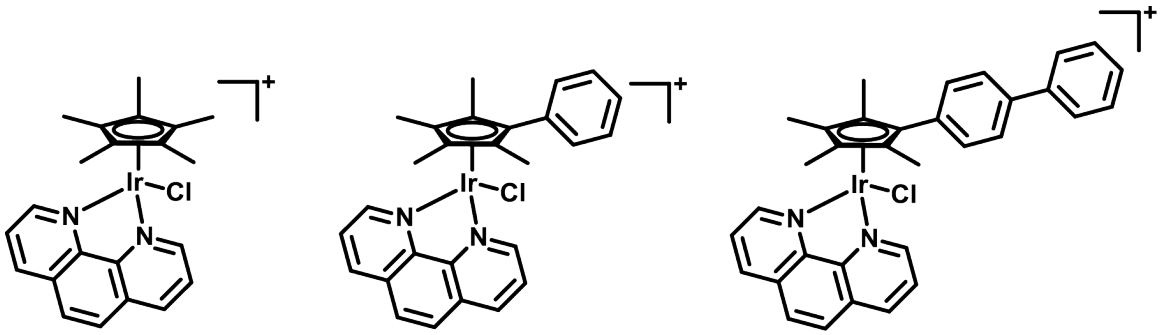

Ir6 **Ir7** **Ir8**

Chart 2. Structures of **Ir6**, **Ir7**, **Ir8**.

Qualitatively, the ICP-MS results were supported by the fluorescent cell imaging studies (Figure 4). Our microscopy experiments showed that **Ir1'** had a higher accumulation than **Ir4'** under similar imaging conditions. Cells that were treated with

Ir5' were hardly visible by fluorescent microscopy even when 100% laser power was used. The low concentration of **Ir5'** in cells is consistent with our ICP-MS analysis results.

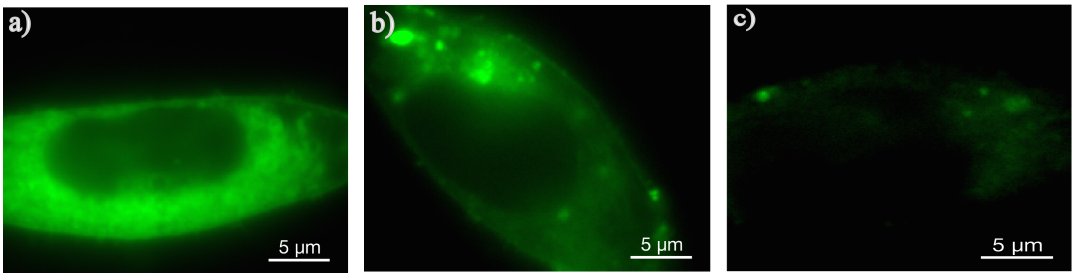

Figure 4. Fluorescence microscopy images (100x oil objectiove) of NIH3T3 treated with a) 5 µM of **Ir1'** for 1 h excited with 10% 488 nm laser for 100 ms b) 5 µM of **Ir4'** for 1 h excited with 10% 488 nm laser for 100 ms c) 5 µM of **Ir5'** for 1 h excited with 100% 488 nm laser for 60 ms.

3.2.3. Spatial Distribution of Iridium Catalysts in Cells

The spatial distribution of iridium catalysts in the cell was studied using the fluorognic catalysts. The Ir-bodipy complexes were co-treated with commercially available organelle specific dyes and imaged by fluorescent microscopy. The Pearson's Correlation Coefficient (PCC) was calculated upon plotting the pixel intensities of the images along two different emission channels. A PCC value of 0.74 was obtained for NIH3T3 cells treated with both Mito-ID and **Ir1'**, indicating excellent ability of **Ir1'** to target mitochondria. **Ir4'** (PCC = 0.69) showed very similar mitochondrial targeting propensity as **Ir1'** whereas the intensity correlation of **Ir5'** with Mito-ID (PCC = 0.54) was found to be slightly lower (Figure 5). Because intracellular NADH is required to facilitate transfer hydrogenation in cells, we hypothesized that catalysts that localize in

the mitochondria would be more catalytically active, since the mitochondria is one of the sources for NADH in cells. When cells were co-treated with iridium-bodipy catalysts and commercially available nuclear dye Hoechst 33342, no signal overlap was observed (Figure 6). In contrast, we found good correlation between Ir-bodipy and lysosome dye Lyso-ID. The PCC for **Ir1'**, **Ir4'** and **Ir5'** with Lyso-ID are 0.77, 0.68, and 0.43z respectively (Figure 7).

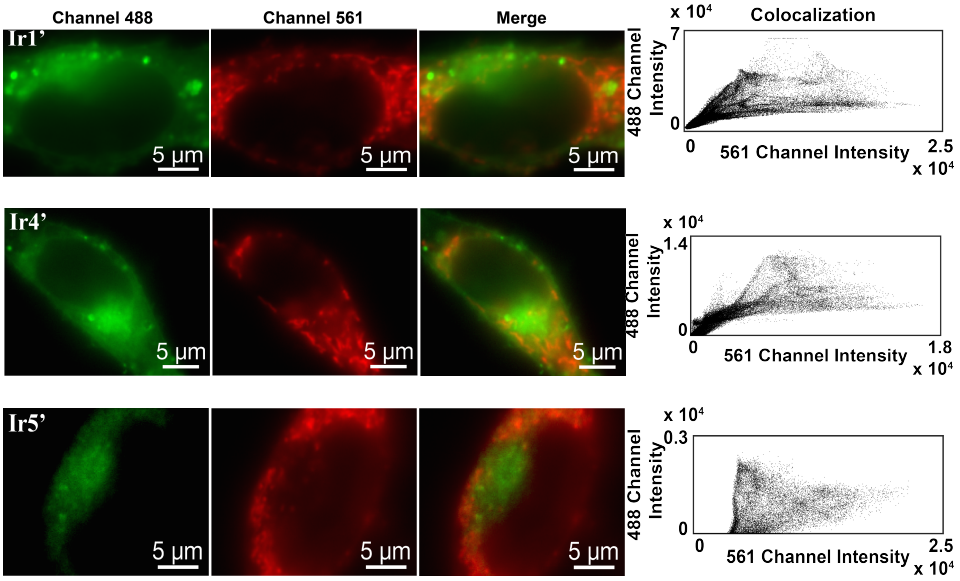

Figure 5. Colocalization images of **Ir1', Ir4'** and **Ir5'** with Mito-ID and intensity correlation plot of two signals. The excitation wavelength for Ir complexes is 488 nm. The excitation wavelength of Mito-ID is 561 nm. Emission filter: 525 ± 25 nm for Ir complexes. Images were acquired using 100× oil objective in Olympus IX83 microscope.

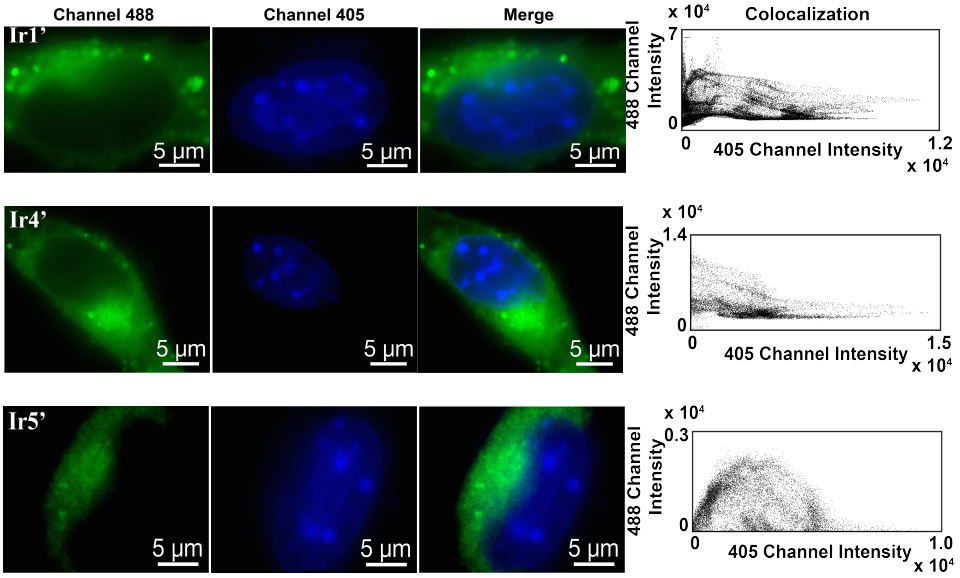

Figure 6. Colocalization images of **Ir1', Ir4'** and **Ir5'** with Hoechst 33342 and intensity correlation plot of two signals. The excitation wavelength for Ir complexes is 488 nm. The excitation wavelength of Hoechst 33342 is 405 nm. Emission filter: 525 ± 25 nm for Ir complexes, 438 ± 12 nm for Hoechst 33342. Images were acquired using 100× oil objective in Olympus IX83 microscope.

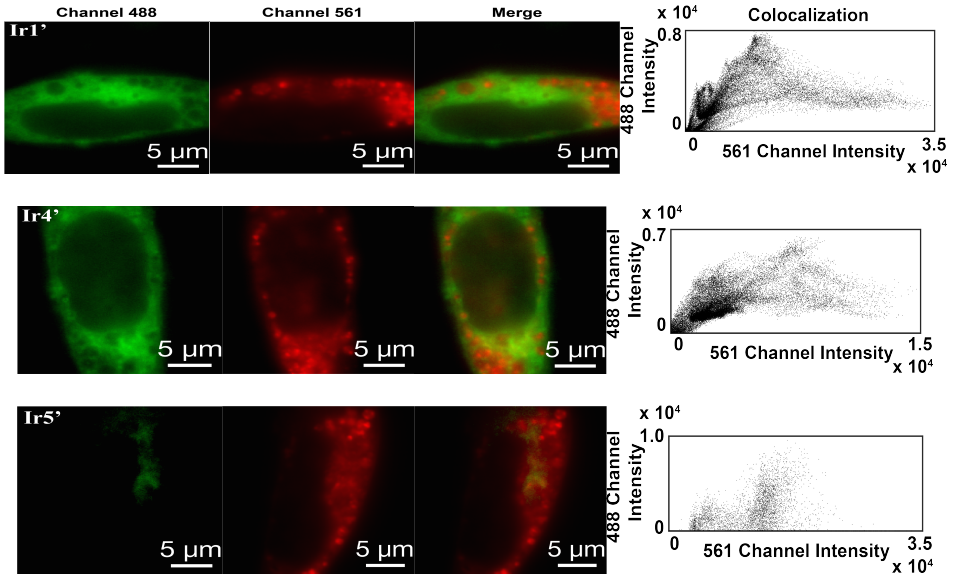

Figure 7. Colocalization images of **Ir1', Ir4'** and **Ir5'** with Lyso-ID and the scatter plot of two signals. The excitation wavelength for Ir complexes is 488 nm. The excitation wavelength of Lyso-ID is 561 nm. Emission filter: 525 ± 25 nm for Ir complexes. Images were acquired using 100× oil objective in Olympus IX83 microscope.

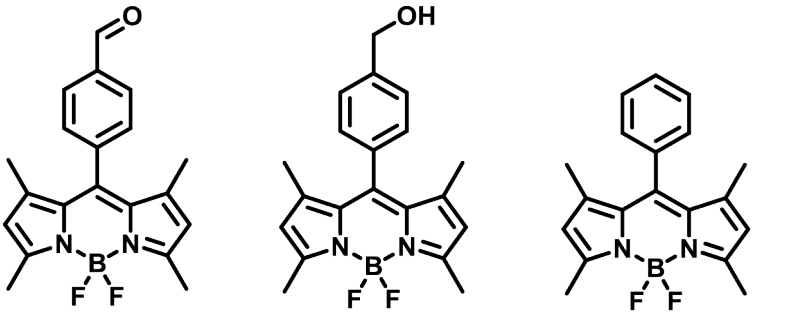

Bodipy-CHO **Bodipy-OH** **Internal Standard (ISTD)**

Chart 3. Fluorescent substrates and internal standard used in LC-ESI-MS study.

3.2.4. Intracellular Reactivity of Iridium Catalysts

Next, we proceeded to determine the efficiency of the Ir catalysts by quantifying the transfer hydrogenation products formed in cells (Scheme 3). For these experiments, NIH3T3 cells were treated with 30 μM of **Bodipy-CHO,** washed with fresh media, and then treated with 10 μM of Ir catalysts. After 2 h, the cells were counted and lysed to extract the transfer hydrogenation products. LC-ESI-MS analysis of the cell lysate was performed to quantify the amount of **Bodipy-OH** formed and **Bodipy-CHO** remaining after the reaction. As low as 100 pg of pure **Bodipy-CHO** or pure **Bodipy-OH** could be detected in cell lysate matrix using a triple quadrupole mass analyzer. Product over starting material ratio for each catalyst treatment was calculated and normalized by the cellular uptake of the catalyst. Turn over numbers (TON) of the catalysts could not be calculated as concentration of iridium was found to be much higher in cell compared to that of substrate.

In control experiments, we observed that aldehyde reduction occurred in the absence of Ir catalyst, which might be due to reaction of our substrate with aldehyde

reductases. However, cells that contained **Ir1** and **Ir4** were found to produce more products than cells that lacked Ir catalysts. The activity of **Ir4** was found to be higher than that of **Ir1** when that data were normalized based on the amount of Ir taken up inside the cells (Table 1).

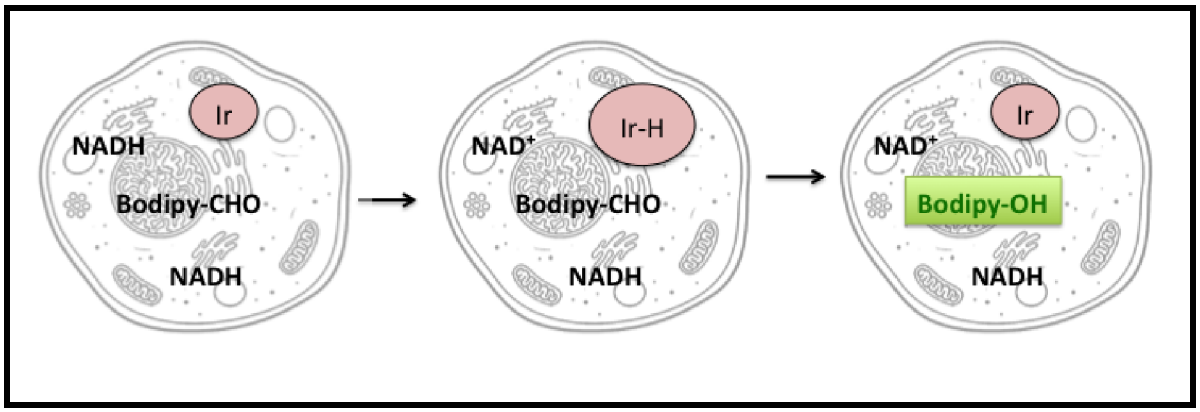

Scheme 3. Reaction of a fluorogenic aldehyde probe inside cells treated with iridium catalysts.

Table 1. Quantitative analysis of transfer hydrogenation reaction in NIH3T3 by iridium catalysts.

Catalyst	[product][a]/[starting Material][b]	Activity[c] (normalized by [Ir])
no catalyst	1.68 ±0.25	-
Ir1	2.25 ±0.21	0.66
Ir4	4.23 ±0.34	1.52
Ir5	1.46 ±0.13	-
Ir1'	1.43 ±0.25	-
Ir4'	1.42 ±0.37	-
Ir5'	1.83 ±0.23	-

[a]Concentration of **Bodipy-OH** = total amount of **Bodipy-OH** in reaction ÷ cell volume (1.7pL); [b]Concentration of **Bodipy-CHO** = total amount of **Bodipy-CHO** in reaction ÷ cell volume (1.7pL); [c]Activity = ([Product]/[Starting Material]) ÷ (Total iridium uptake/cell volume)

It is evident from the LC-ESI-MS data that **Ir1** and **Ir4** could retain their activity in cell whereas, other catalysts could not. **Ir5** and **Ir5'** were expected to be inactive in cells from their poor catalytic performance in ^{t}BuOH/H_2O. Although, **Ir1'** and **Ir4'** showed very similar *in-vitro* activity with that of **Ir1** and **Ir4** in the reaction flask and good cell permeability, they were not active in cells. The loss of catalytic activity of **Ir1'**

and **Ir4'** in cells might be due to their high toxicity (Figure 8).

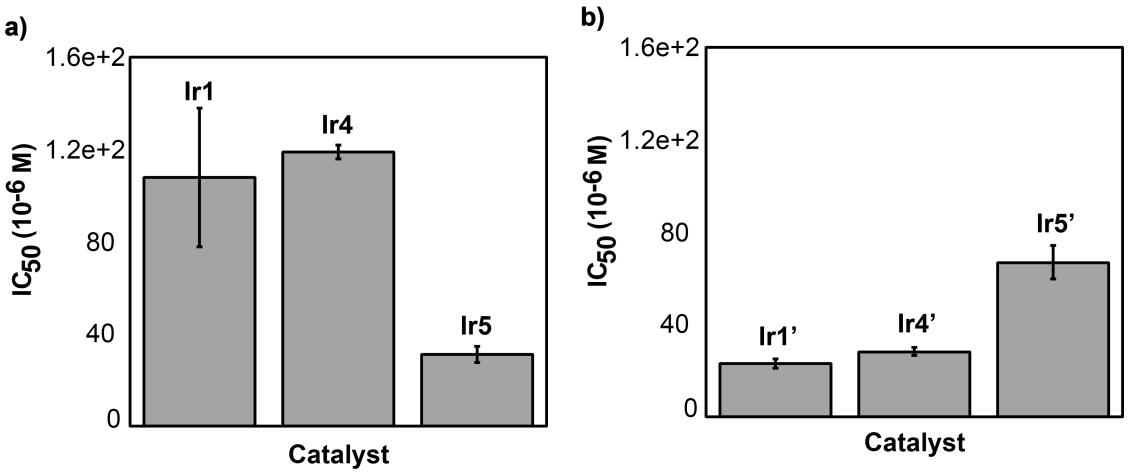

Figure 8. Cytotoxicity data obtained from the treatment of NIH3T3 cells with a) **Ir1**, **Ir4**, and **Ir5** b) **Ir1', Ir4'** and **Ir5'** for 3 h (+1 h incubation with MTS). The cell viability percentage was determined using a colorimetric MTS assay. The values shown are the average values from three separate runs.

Our results indicate that the intracellular activity of the catalysts is affected by many parameters, such as cell permeability, cytotoxicity, and intrinsic reactivity.

3.3. Conclusions

We prepared new Ir(III) catalysts with covalently attached fluorophores. These new fluorogenic probes allowed us to locate the catalysts inside live cells by microscopy. We found that they localize in both the mitochondria and lysosome, but not the nucleus. We have studied the intracellular activity of transfer hydrogenation Ir(III) catalysts for the first time in live mammalian cells. The parent iridium catalysts retained their activity in live cells, whereas, the Ir-bodipy catalyst conjugates lost their activities in cells even

though they showed comparable *in-vitro* activity with the non-fluorogenic catalysts. We have quantified the cellular uptake and cytotoxicity of the Ir complexes. We propose that the high toxicity of the Ir-bodipy catalysts is responsible for their poor activity in cells.

3.4. Experimental Section

3.4.1. General Procedures

Commercial reagents were used as received without further purification. All air- and water-sensitive manipulations were performed using standard Schlenk techniques or under a nitrogen atmosphere using a glovebox. Anhydrous solvents were obtained from an Innovative Technology solvent drying system saturated with Argon. **Bodipy-CHO** and **Bodipy-OH** was synthesized according to literature procedures.[13] **1**[14] and **3**[15] were synthesized according to literature procedures. Iridium complexes **Ir1**,[16] **Ir4**,[11] and **Ir5**[11] were prepared as previously described. NIH-3T3 mouse fibroblast cells was obtained from ATCC.

Physical Methods. NMR spectra were acquired using JEOL spectrometers (ECA-400, 500, and 600) at room temperature and referenced using residual solvent peaks. A Horiba Fluoromax 4 fluorometer was used to record the emission spectra. Gas chromatography-mass spectrometry was performed using an Agilent 7890 GC/5977A MSD instrument equipped with an HP-5MS capillary column. A Varian 810 instrument was used to acquire inductively coupled plasma-mass spectrometry (ICP–MS) analyses. All biological cell images were obtained using Olympus IX-83 inverted microscope equipped with a 100× oil objective. Liquid chromatography was performed on a Kinetex XB-C18 100 Å column (Phenomenex, 50×2.1 mm, 2.6 μm) coupled with an Agilent triple

quadrupole mass spectrometer.

3.4.2. Synthesis

Compound 2: Compound **1** (0.15 g, 0.34 mmol, 1.05 equiv.) and 1-bromo-4-nitrobenzene (0.07 g, 0.33 mmol, 1.0 equiv.) were dissolved in 15 mL of dry THF and 6 mL of dry DMF under N_2. A 1.5 mL solution of 0.26 M aq. solution of Na_2CO_3 was added and the reaction was purged with N_2 for 30 mins before adding $Pd(PPh_3)_4$ (0.02 g, 0.02 mmol, 0.05 equiv.). The reaction was then stirred under reflux for 2 d under N_2. After two days, DMF was removed; 30 mL of water added and the product was extracted into DCM (3×30 mL). The organic layer was separated, filtered through a pad of celite, dried over anhydrous Na_2SO_4, filtered, and then the solvent was removed by rotary evaporation. The crude product was purified by recrystallization from DCM/Hexane to yield a red solid (66.5%, 97 mg, 0.22 mmol). ^{1}H NMR (600 MHz, $CDCl_3$): 8.33 (d, J = 12 Hz, 2H), 7.82 (d, J = 6 Hz, 2H), 7.77 (d, J = 12 Hz, 2H), 7.42 (d, J= 12 Hz, 2H), 6.00 (s, 2H), 2.56 (s, 6H), 1.43 (s, 6H) ppm.

Compound 3: Compound **2** (0.28 g, 0.64 mmol) and hydrazine (1.0 mL, 31.9 mmol, 50 equiv.) along with 10 % Pd/C (0.19 g, 0.18 mmol, 0.28 equiv.) were combined in 40 mL of EtOH and 5 mL THF and refluxed for 5 h. The reaction mixture was cooled to room temperature and filtered through celite to remove the Pd/C. The filtrate was dried over anhydrous Na_2SO_4, filtered, and then the solvent was removed by rotary evaporation. The crude product was purified by recrystallization from DCM/Hexane to

yield a dark red solid (9%, 23 mg, 0.05 mmol) ^{1}H NMR (400 MHz, $CDCl_3$): 7.66 (d, *J* = 8 Hz, 2H), 7.49 (d, *J* = 8 Hz, 2H), 7.27 (d, *J* = 8 Hz, 2H), 6.78 (d, *J*= 8 Hz, 2H), 5.98 (s, 2H), 2.55 (s, 6H), 1.44 (s, 6H) ppm.

General Procedure for the Synthesis of 4A, 4B, and 4C: In a Schlenk flask, 4-R-picolinic acid (1.0 equiv.) and triethylamine (2.0 equiv.) were taken in 15 mL of dry DCM under N_2. The reaction flask was cooled to 0°C and stirred for 30 min. Ethylchloroformate (1.0 equiv.) was added to the flask under an inert atmosphere and stirred at 0°C for another 30 min. Compound **3** (0.57 equiv.) was added to the reaction mixture at 0°C and the reaction was stirred for 1 h. The flask was then allowed to warm to RT and stirred overnight. The next day, the DCM layer was washed with 20 mL of water. The organic layer was separated, dried over anhydrous Na_2SO_4, filtered, and then the solvent was removed by rotary evaporation. The crude product was purified by recrystallization from DCM/Hexane.

4A: yield 22.0% with respect to **3**; ^{1}H NMR (500 MHz, $CDCl_3$): 10.14 (s, 1H), 8.63 (d, *J* = 5 Hz, 1H), 8.32 (d, *J* = 5 Hz, 1H), 7.95-7.91 (m, 3H), 7.76-7.71 (m, 4H), 7.52-7.50 (m, 1H), 7.33 (d, *J*= 10 Hz, 2H), 5.99 (s, 2H), 2.56 (s, 6H), 1.45 (s, 6H) ^{13}C NMR (125 MHz, CDCl3): δ = 162.16, 155.56, 149.77, 148.11, 143.26, 141.56, 141.11, 137.89, 137.68, 135.89, 133.79, 131.56, 128.59, 127.74, 127.38, 126.70, 122.56, 121.32, 120.11, 14.72, 1.13 ppm ^{19}F NMR (400 MHz, $CDCl_3$): δ = -146.13 ppm.

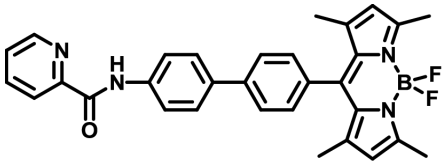

4B: yield 66.0% with respect to **3**; ^{1}H NMR (600 MHz, $CDCl_3$): 10.02 (s, 1H), 8.83 (d, *J* = 6 Hz, 1H), 8.56 (s, 1H), 7.90 (d, *J* = 6 Hz, 2H), 7.75-7.72 (m, 5H), 7.34 (d, *J* = 6 Hz, 2H), 5.98 (s, 2H), 2.55 (s, 6H), 1.44 (s, 6H) ^{13}C NMR (600 MHz, $CDCl_3$: δ = 160.68,

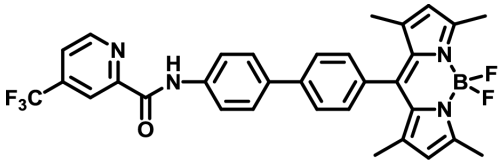

155.59, 151.29, 149.21, 143.22, 141.55, 140.97, 137.19, 136.37, 133.93, 131.54, 128.64, 127.82, 127.40, 122.26, 121.33, 120.25, 118.67, 29.80, 14.70 ppm ^{19}F NMR (400 MHz, $CDCl_3$): δ = -64.67, -146.11 ppm.

4C: yield 75.0% with respect to **3**, ^{1}H NMR (600 MHz, $CDCl_3$): 10.14 (s, 1H), 8.64 (s, 1H), 8.32 (d, *J* = 6 Hz, 1H), 7.91 (d, *J* = 6 Hz, 2H), 7.76-7.71 (m, 4H), 7.51 (s, 1H), 7.33 (d, *J*= 6 Hz, 2H), 5.99 (s, 2H), 2.56 (s, 6H), 1.45 (s, 6H)

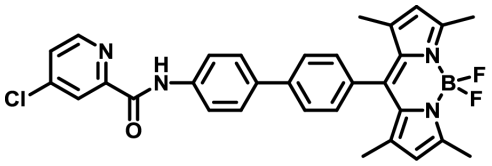

^{13}C NMR (600 MHz, $CDCl_3$): δ = 162.14, 155.55, 149.76, 148.09, 143.25, 141.64, 141.11, 137.88, 137.67, 135.89, 133.79, 131.56, 129.17, 128.59, 127.73, 127.37, 126.69, 122.56, 121.31, 120.11 14.70 ppm. ^{19}F NMR (400 MHz, $CDCl_3$): δ = -146.11 ppm.

Compound 4D: In a closed pressure vessel **4C** (0.03 g, 0.05 mmol, 1.0 equiv.) and dimethyl amine (0.65 mL, 5.14 mmol, 95.0 equiv., 40% aq. solution) were combined and the reaction was stirred at 100°C for 2 d. After two days, the reaction was cooled to RT, 20 mL of water was added, and the product was extracted into DCM (3×30 mL). The organic layer was separated, dried over anhydrous Na_2SO_4, filtered, and then the solvent was removed by rotary evaporation. The crude product was purified by recrystallization from DCM/Hexane to yield a dark red solid (49.0%, 15 mg, 0.03 mmol). ^{1}H NMR (600 MHz, $CDCl_3$): 10.26 (s, 1H), 8.21 (d, *J* = 6 Hz, 1H), 7.89 (d, *J* = 12 Hz, 2H), 7.74 (d, *J* = 6 Hz, 2H), 7.69 (d, *J*= 12 Hz, 2H), 7.56 (d, *J* = 6 Hz, 1H), 7.33 (d, *J* = 6 Hz, 2H), 5.98 (s, 2H), 3.10 (s, 6H), 2.56 (s, 6H) 1.45 (s, 6H), ppm. ^{13}C NMR (600 MHz, CDCl3): δ = 163.26, 155.51, 149.92, 148.17, 143.28, 141.71,

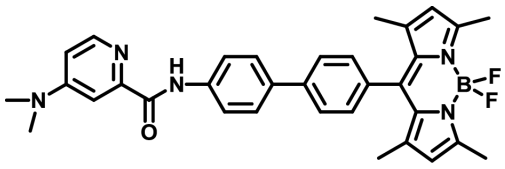

141.19, 137.97, 135.54, 133.66, 131.56, 128.53, 127.66, 127.35, 121.30, 120.02, 108.45, 105.31, 39.45, 14.72 ppm. ^{19}F NMR (400 MHz, $CDCl_3$): δ = -146.13 ppm.

General Procedure for the Synthesis of Ir1', Ir4', and Ir5': In a Schlenk flask, 10 mL of dry DMF was purged with nitrogen for about 30 min. Solid $[Cp^*IrCl_2]_2$ (1.0 equiv.) and **4A**, **4B**, **4D** (2.0 equiv.) were added and stirred for 15 min at 90°C. The reaction mixture was then treated with ammonium hexafluorophosphate (4.7 equiv.) and stirred for another 22 h at 90°C. The DMF solvent was removed by rotary evaporation to yield a brown solid, which was then redissolved in 20 mL of dichloromethane, and washed with water (3×20 mL). The organic phase was separated, dried over sodium sulfate, filtered, and then evaporated to dryness. The crude product was purified by recrystallization from DCM/Hex.

Ir1': yield 19.0%, ^{1}H NMR (500 MHz, $CDCl_3$): 8.59 (d, *J* = 5 Hz, 1H), 8.17 (d, *J* = 5 Hz, 1H), 7.94 (t, *J* = 5 Hz, 1H), 7.79-7.74 (m, 4H), 7.62 (d, *J* = 10 Hz 2H), 7.51 (t, *J*= 5 Hz, 1H), 7.31 (d, *J*= 10 Hz, 2H), 5.99 (s, 2H), 2.56 (s, 6H) 1.47-1.45 (m, 21H) ppm. ^{19}F NMR (400 MHz, $CDCl_3$): δ = -146.15 ppm. $[M+H]^+$ Calc. 883.27430, found 883.27509. *Note:* ***Ir1'*** *is too insoluble in organic solvents to obtain its* ^{13}*C NMR spectrum*

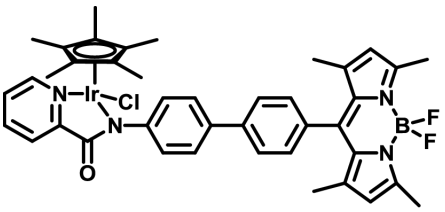

Ir4': yield 46.72%, ^{1}H NMR (400 MHz, $CDCl_3$): 8.08 (d, *J* = 8 Hz, 1H), 7.78-7.74 (m, 4H), 7.60 (d, *J* = 8 Hz, 2H), 7.34-7.30 (m, 3H), 6.60-6.57 (m, 1H), 5.99 (s, 2H), 3.14 (s, 6H), 2.56 (s, 6H), 1.47-1.44 (m, 21H) ^{13}C NMR (125 MHz, $CDCl_3$): δ = 169.67, 155.41, 155.23, 154.21, 148.73, 148.67, 143.39, 142.02, 135.50, 133.21, 131.64, 128.34, 127.71,

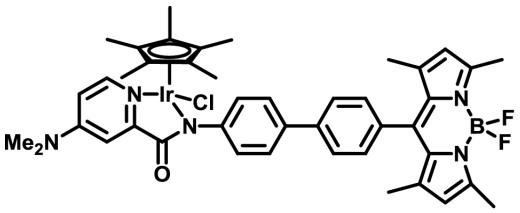

127.44, 126.57, 121.26, 109.45, 108.70, 85.87, 39.63, 14.80, 8.72, 1.12 ppm ^{19}F NMR (400 MHz, $CDCl_3$): δ = -146.13 ppm. $[M+H]^+$ Calc. 926.31540, found 926.31036.

Ir5': yield 50.0%, ^{1}H NMR (500 MHz, $CDCl_3$): 8.76 (d, *J* = 5 Hz, 1H), 8.42 (s, 1H),

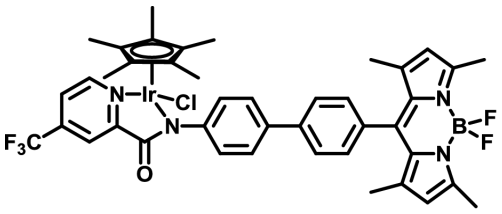

7.76-7.71 (m, 5H), 7.64 (d, *J* = 10 Hz, 2H), 7.32 (d, *J* = 10 Hz, 2H), 5.99 (s, 2H), 2.56 (s, 6H), 1.47 (s, 21H) ^{13}C NMR (125 MHz, $CDCl_3$): δ = 167.71, 157.39, 155.49, 150.74, 147.69, 143.32, 141.83, 141.67, 140.72, 140.44, 136.39, 133.54, 131.60, 128.47, 127.49, 127.33, 126.95, 123.01, 121.30, 87.34, 14.78, 8.71 ppm. ^{19}F NMR (400 MHz, $CDCl_3$): δ = -64.70, -146.12 ppm. $[M+H]^+$ Calc. 951.26168, found 951.26306.

3.4.3. Cytotoxicity Studies

NIH-3T3 mouse fibroblast cells (10000 cells/well) were seeded in a 96-well plate and allowed to attach overnight in a 5% CO_2 humidified incubator. The catalysts were pre-dissolved in sterile DMSO to give a 5 mM stock solution and then diluted using commercial cell growth media (Dulbecco's Modified Eagle Medium (DMEM) supplemented with 5% fetal bovine serum (FB Essence from VWR) and 1% penicillin streptomycin solution (100×)) to give a series of different concentrations (0.1, 1, 25, 50, 100, and 250 μM). The cells were then treated with the catalyst solutions (6 wells per concentration) for 3 h. The solutions were removed by pipette and the cells were washed with fresh DMEM twice before adding DMEM containing 3-(4,5-dimethylthiazol-2-yl)-5-(3-carboxymethoxyphenyl)-2-(4-sulfophenyl)-2H-tetrazolium (MTS) (2 mL MTS/8

mL DMEM). After 1 h, the absorbance of the 96-well plate was measured at 490 nm to determine the amount of orange formazan complex formed. Cell viability was considered to be proportional to the absorbance of the wells. The absorbance value of the wells containing solutions of MTS (background) was subtracted from those of the wells containing treated and control cells. The percentage cell viability was calculated using the following equation: $(A_{conc}/A_{control})\times 100\%$, where A_{conc} is the absorbance at a specific probe concentration and $A_{control}$ is the absorbance of the untreated cells sample. The cell viability data were fit to a single exponential decay function and the IC_{50} value was extracted from this fit at 50% cell viability.

3.4.4. Iridium Accumulation in Live Cell

NIH-3T3 cells were cultured in 100 mm tissue culture plates (Corning) at 37°C under a 5% CO_2 atmosphere. After 100% confluence was achieved, the cells were incubated with either 5 or 10 μM of catalysts for 2 h in DMEM supplemented with 5% fetal bovine serum (FB Essence) and 1% penicillin streptomycin solution (100×) (diluted from 5 mM stock solution in sterile DMSO). After 2 h of incubation the catalyst solutions were removed and the cells were rinsed twice with fresh DMEM. The adhered cells were detached by trypsin and counted using a BIO-RAD TC10 automated cell counter. The sample was then centrifuged and the supernatant was removed. The cell pellet was washed an additional time with phosphate buffered saline (PBS), centrifuged, and then the supernatant was removed. The cell pellets were digested with 0.5 mL of 70% HNO_3 at room temperature overnight. Each sample was diluted with 6.5 mL of HPLC grade H_2O to obtain 5% HNO_3 sample solutions. The cloudy solutions were centrifuged and the clear supernatant was separated and used for analysis by ICP-MS. The total iridium

content per cell was calculated using the solution volume and cell density from each sample preparation.

3.4.5. Cellular Localization study

NIH-3T3 cells were cultured at 37°C under a 5% CO_2 humidified atmosphere in Dulbecco's Modified Eagle Medium (DMEM) supplemented with 10% fetal bovine serum (FB Essence from VWR) and 1% penicillin streptomycin solution (100×). For live cell imaging, cells were plated in μ-Slide 8-well plates (IBIDI) in 200 μL of DMEM in each well. After overnight cell growth, the medium was removed and cells were treated with 5 μM **Ir1'/ Ir4'/ Ir5'** solution in DMEM (diluted from 5 mM stock in sterile DMSO). After an incubation time of 30 mins (37 °C, 5% CO_2), the growth solutions were removed and cells were co-treated with **Ir1'/ Ir4'/ Ir5'** and Mito-ID and Hoechst33342 for another 30 mins (37 °C, 5% CO_2). The cells were rinsed with fresh DMEM (1×200 μL each well), followed by phenol red free DMEM (1×200 μL each well), and then visualized immediately using microscopy (Olympus IX83) with a 100× oil-immersion objective. The excitation wavelength was 488 nm for **Ir1'/ Ir4'/ Ir5'** is 488 nm (emission filter: 500-550 nm), 405 nm for Hoechst33342 (emission filter: 426-450 nm), and 561 nm for Mito-ID. The images were processed by subtracting background emission and emission from control cells using the program ImageJ and PCC values were calculated using MATLAB algorithm for Pearson's Correlation Coefficient.

3.4.6. LC-ESI-MS Analysis of Intracellular Reaction Yields

NIH-3T3 cells were cultured in 100 mm culture dish at 37°C under a 5% CO_2 humidified atmosphere in Dulbecco's Modified Eagle Medium (DMEM) supplemented with 10%

fetal bovine serum (FB Essence from VWR) and 1% penicillin streptomycin solution (100×). After 100% confluence was achieved, cells were treated with 10 mL of 30 μM **Bodipy-CHO** solution in DMEM (diluted from 10 mM stock in sterile DMSO). After an incubation time of 4 h (37 °C, 5% CO_2), the growth solutions were removed. All of the cells were rinsed with fresh DMEM (2×10 mL). The cells were then treated with 10 mL of DMEM solution containing 10 μM of Ir catalyst (diluted from 5 mM stock solution in sterile DMSO) for 2 h. After a 2 h incubation period, the cell growth media were removed and the adhered cells were washed twice with DMEM (5 mL each time) followed by detachment using trypsin. The cell density was determined by treating the cells with Trypan Blue and then counted using a BIO-RAD TC10 automated cell counter.

Finally, the cells were washed with PBS, centrifuged, and then the supernatant was removed by pipette. A 1.0 mL solution of ice-cold water/acetonitrile/methanol (1:2:2) was added to the cell pellets. The cell suspension was transferred to a glass autosampler vial and vortex for 5 min. The sample was snap frozen by immersing in liquid nitrogen and then thawing to RT (3 times). The sample was transferred to a 1.5 mL centrifuge tube and centrifuged at 16000 xg for 15 min at 4°C. A 800 μL solution of the supernatant was collected and freeze dried. Dry cell lysate sample was dissolved in 100 μL of 40% acetonitrile in water with an internal standard (final concentration 92.7 pg/ 20 μL) followed by purification by C18 ziptip. The sample solution was then subjected to LC-ESI-MS analysis. A blank (acetonitrile) was run before every sample analysis.

LC-ESI-MS was performed using an Agilent 6460 tripple quadrupole LC-MS with a Kinetex XB-C18 100 Å column (Phenomenex, 50×2.1 mm, 2.6 μm) eluted with a linear

gradient from 40-93% of mobile phase B (acetonitrile containing 1M formic acid) in mobile phase A (water containing 1M formic acid) for 13 minutes at a flow rate of 200 µL/min. The injection volume was set at 20 µL per sample. The mass spectrometer was set at positive electrospray ionization detection. All other conditions were optimized using Agilent optimizer software and the chromatogram was generated by summing the most intense product ions observed in the full scan MS/MS spectra.

Pure **Bodipy-OH**, **Bodipy-CHO**, and **ISTD** were collected at 6.8, 8, and 8.8 min, respectively on chromatogram (Figure 9, 10). It was possible to separate **Bodipy-CHO** and **Bodipy-OH** from other cell lysate components using the same LC method. (Figure 11)

Calibration curve was obtained by plotting area ratio of analyte over **ISTD** against amount of analyst injected onto column (Figure 10). For the preparation of standard calibration curve, a stock solution containing 1.9 ng/µL of **Bodipy-CHO**/ **Bodipy-OH** was diluted with 40% acetonitrile in water with an internal standard (final concentration 4.6 pg/µL) in dry cell lysate sample (final volume 100 µL) to 5, 10, 15, 25, 35, 50, 125, 250 pg/µL. The standard samples were analyzed after purifying by C18 ziptip in three replicate injections and a blank (acetonitrile) was run before every sample analysis. Correlation coefficient for **Bodipy-CHO** was 0.9932 and for **Bodipy-OH** was 0.9919 over 100 pg to 5 ng on-column.

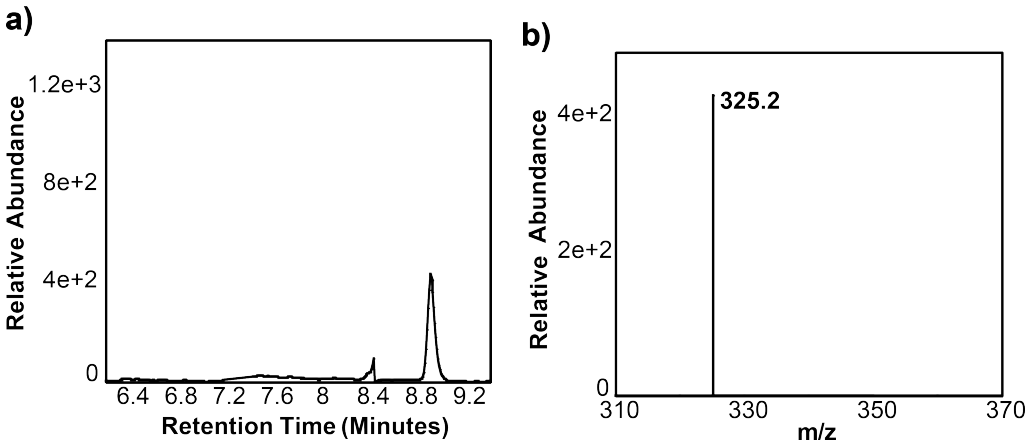

Figure 9. a) LC chromatogram of **ISTD** (100 pg in the column) and b) MS spectra of **ISTD**.

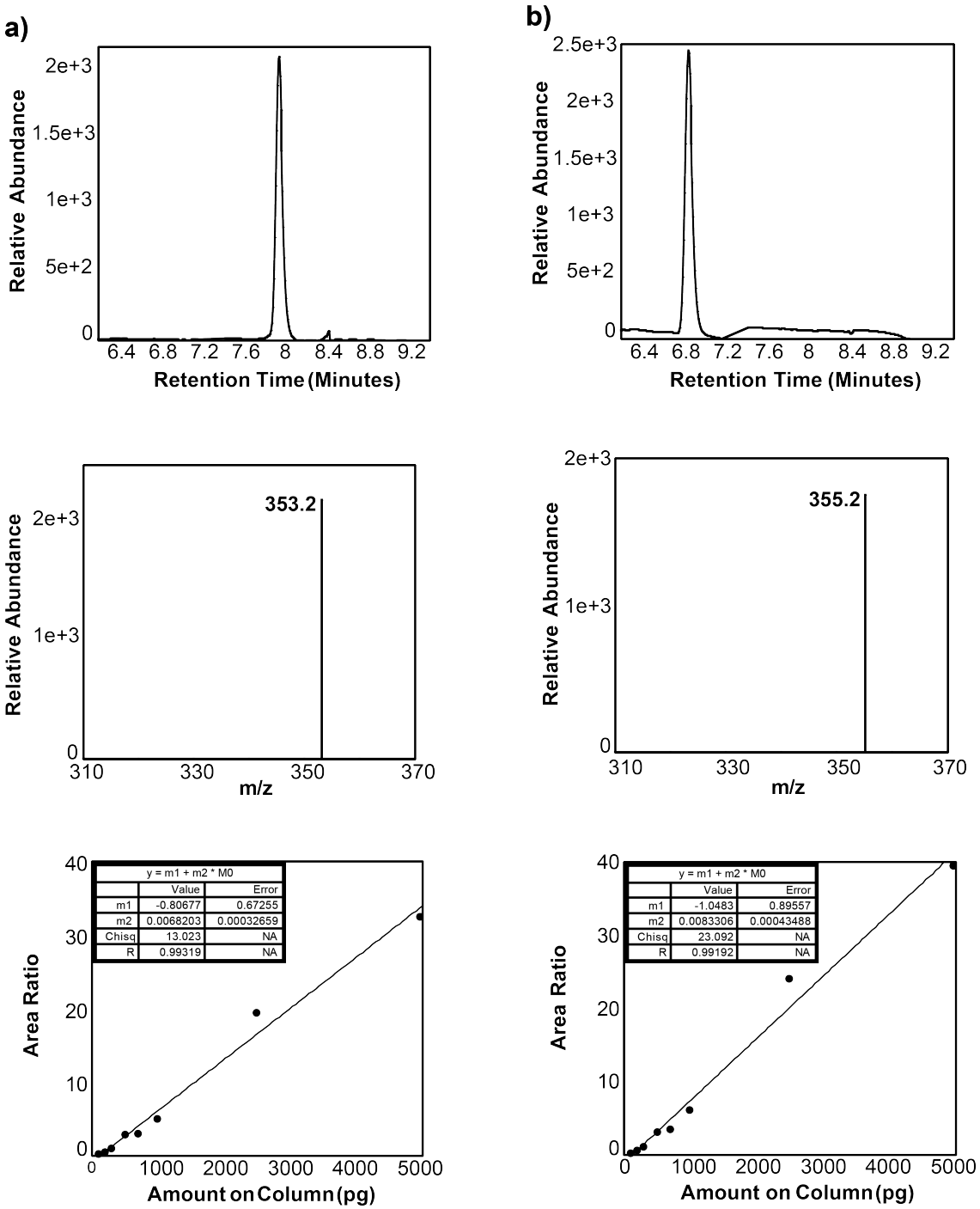

Figure 10. a) LC chromatogram and MS spectra of **Bodipy-CHO** (1 ng in the column); Calibration curve obtained with ISTD for quantification of **Bodipy-CHO** and b) LC chromatogram and MS spectra of of **Bodipy-OH** (1 ng in the column); Calibration curve obtained with ISTD for quantification of **Bodipy-OH**.

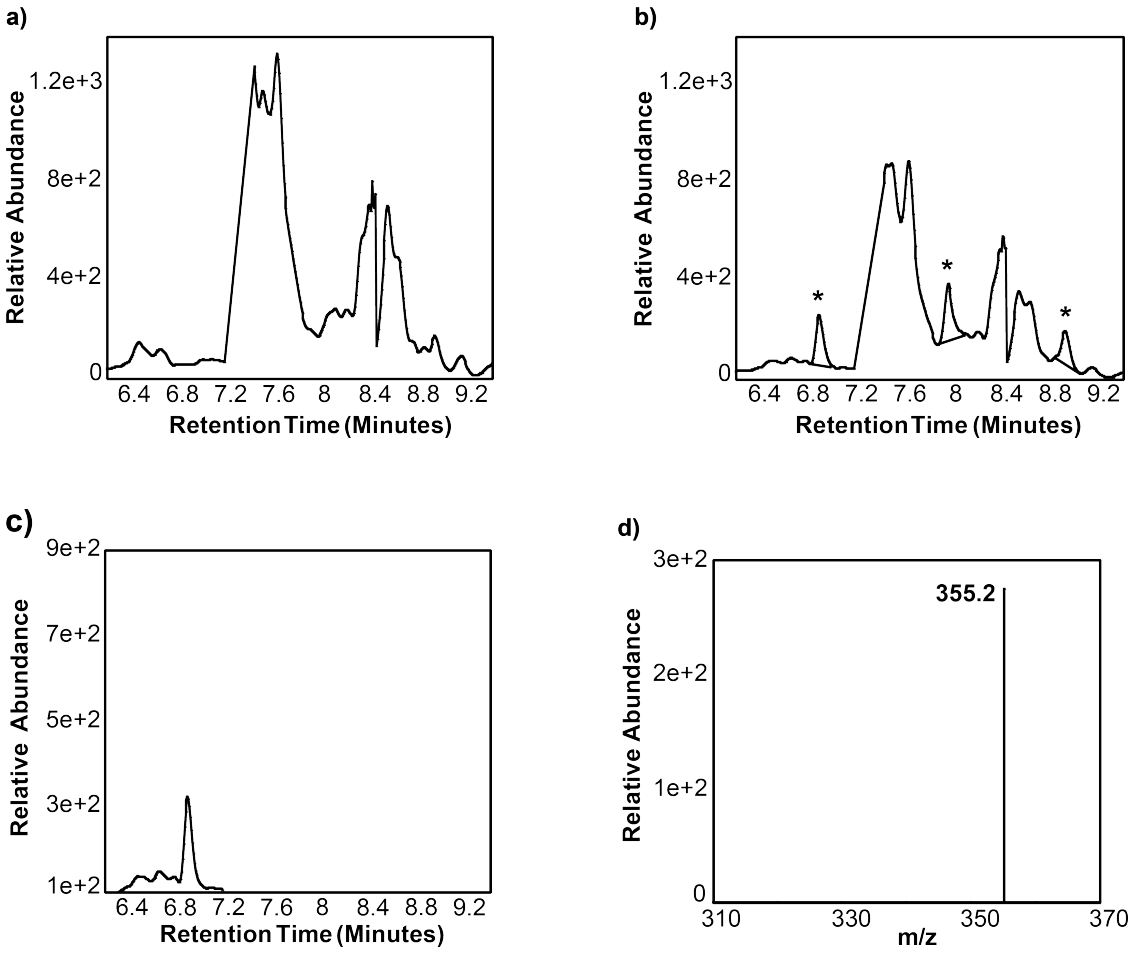

Figure 11. a) LC chromatogram of control cell lysate b) LC chromatogram of cell lysate spiked with 300 pg pure **Bodipy-CHO**, 300 pg pure **Bodipy-OH** and 100 pg **ISTD** (*Peak positions of added pure compounds) c) Extracted LC chromatogram of **Bodipy-OH d)** MS spectra of extracted **Bodipy-OH**.

3.5. References

1. Soldevila-Barreda, J. J.; Romero-Canelón, I.; Habtemariam, A.; Sadler, P. J. *Nat. Commun*. **2015**, *6*, 6582.
2. Li, S.; Wang, L.; Yu, F.; Zhu, Z.; Shobaki, D.; Chen, H.; Wang, M.; Wang, J.; Qin, G.; Erasquin, U. J.; Ren, L.; Wang, Y.; Cai, C. *Chem. Sci.* **2017**, *8*, 2107-2114.
3. Zhao, J.; Rebelein, J. G.; Mallin, H.; Trindler, C.; Pellizzoni, M. M.; Ward, T. R. *J. Am. Chem. Soc.* **2018**, *140*, 13171-13175.
4. Coverdale, J. P. C.; Romero-Canelón, I.; Sanchez-Cano, C.; Clarkson, G. J.; Habtemariam, A.; Wills, M.; J. Sadler, P. J. *Nat. Chem.* **2018**, *10*, 347-354.
5. Hirschhaeuser, F.; Sattler, U. G. A.; Mueller-Klieser, W. *Cancer Res*. **2011**, *71*, 6921-6925.
6. Doherty, J. R.; Cleveland, J. L. J. *Clin. Invest*. **2013**, *123*, 3685-3692.
7. Koukourakis, M. I.; Giatromanolaki, A.; Winter, S.; Leek, R; Sivridis, E.; Harris, A. L. *Oncology* **2009**, *77*, 285-292.
8. Koukourakis, M. I. Giatromanolaki, A.; Sivridis, E.; Bougioukas, G.; Didilis, V.; Gatter, K. C.; Harris, A. L. Br. J. *Cancer* **2003**, *89*, 877-885.
9. Pennington, J. D.; Wang, T. J.; Nguyen, P.; Sun, L.; Bisht, K.; Smart, D.; Gius, D. *Drug Resist. Update* **2005**, *8*, 322-330.
10. Bose, S.; Ngo, A. H.; Do, L. H. *J. Am. Chem. Soc.* **2017**, *139*, 8792-8795.
11. Ngo, A. H. Iridium Complexes for Intracellular Transfer Hydrogenation and Their Potential Biological Applications. Ph.D. Dissertation, University of Houston, Houston, TX, 2019.
12. Liu, Z.; Habtemariam, A.; Pizarro, A. M.; Fletcher, S. A.; Kisova, A.; Vrana, O.; Salassa, L.; Bruijnincx, P. C. A.; Clarkson, G. J.; Brabec, V.; Sadler, P. J. *J. Med. Chem.* **2011**, *54*, 3011-3026.
13. Yue, Y.; Guo, Y.; Xu, J.; Shao, S. *New J. Chem.* **2011**, *35*, 61-64.
14. DiCesare, N.; Lakowicz, J. R. *Tetrahedron Lett.* **2001**, *42*, 9105-9108.
15. Shin, J. –Y.; Patrick, B. O.; Dolphin, D. *Tetrahedron Lett.* **2008**, *49*, 5515-5518.
16. Ngo, A. H.; Ibañez, M.; Do, L. H. *ACS Catal*. **2016**, *6*, 2637-2641.

Chapter 3 Appendix

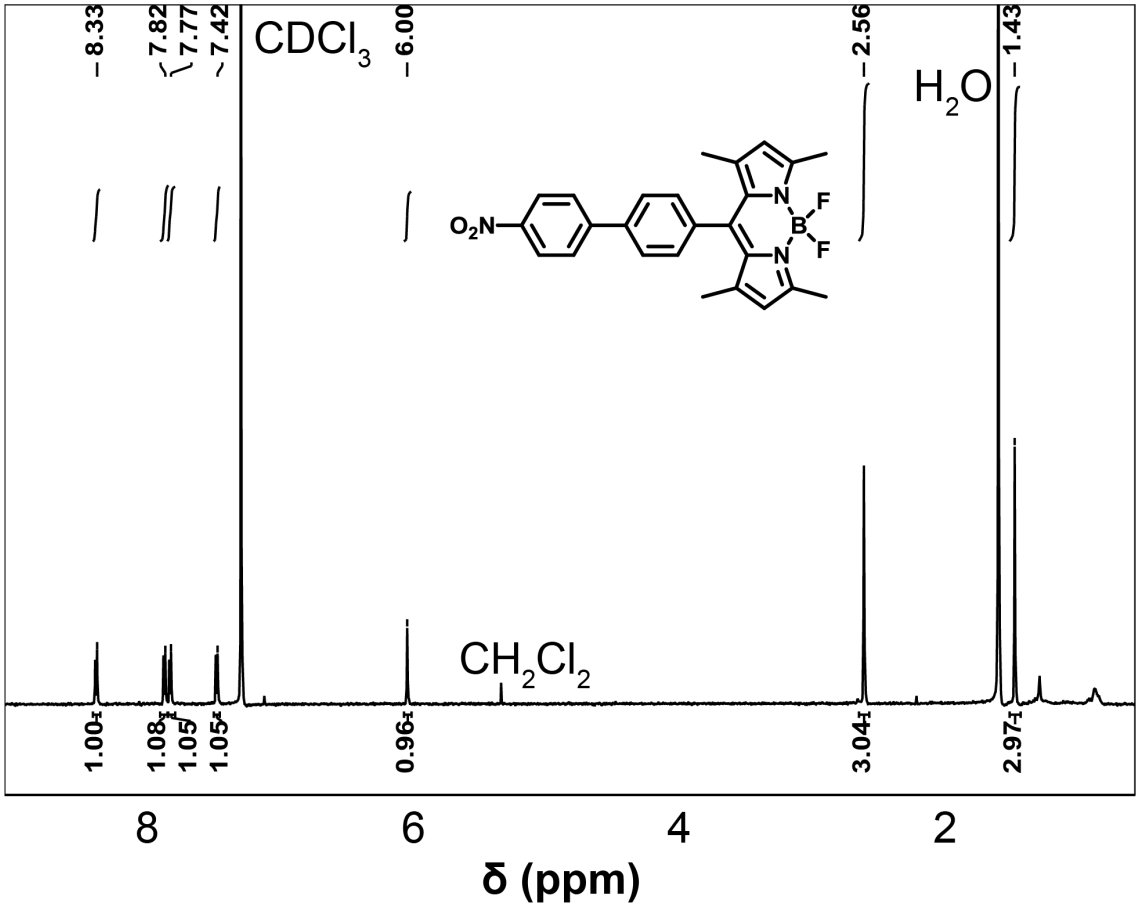

Figure S1. ^{1}H NMR spectrum (600 MHz, $CDCl_3$) of compound **2**.

- Vertical axis represents the abundance.

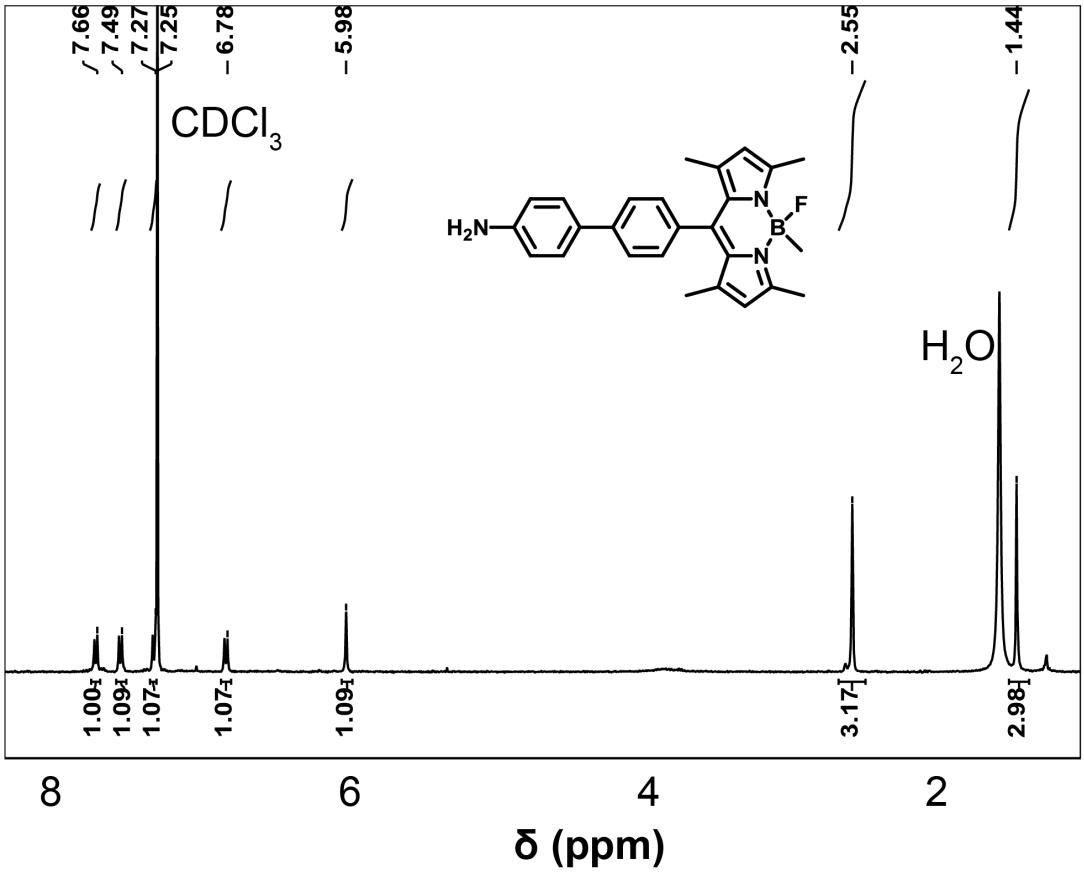

Figure S2. ^{1}H NMR spectrum (400 MHz, $CDCl_3$) of compound **3**.

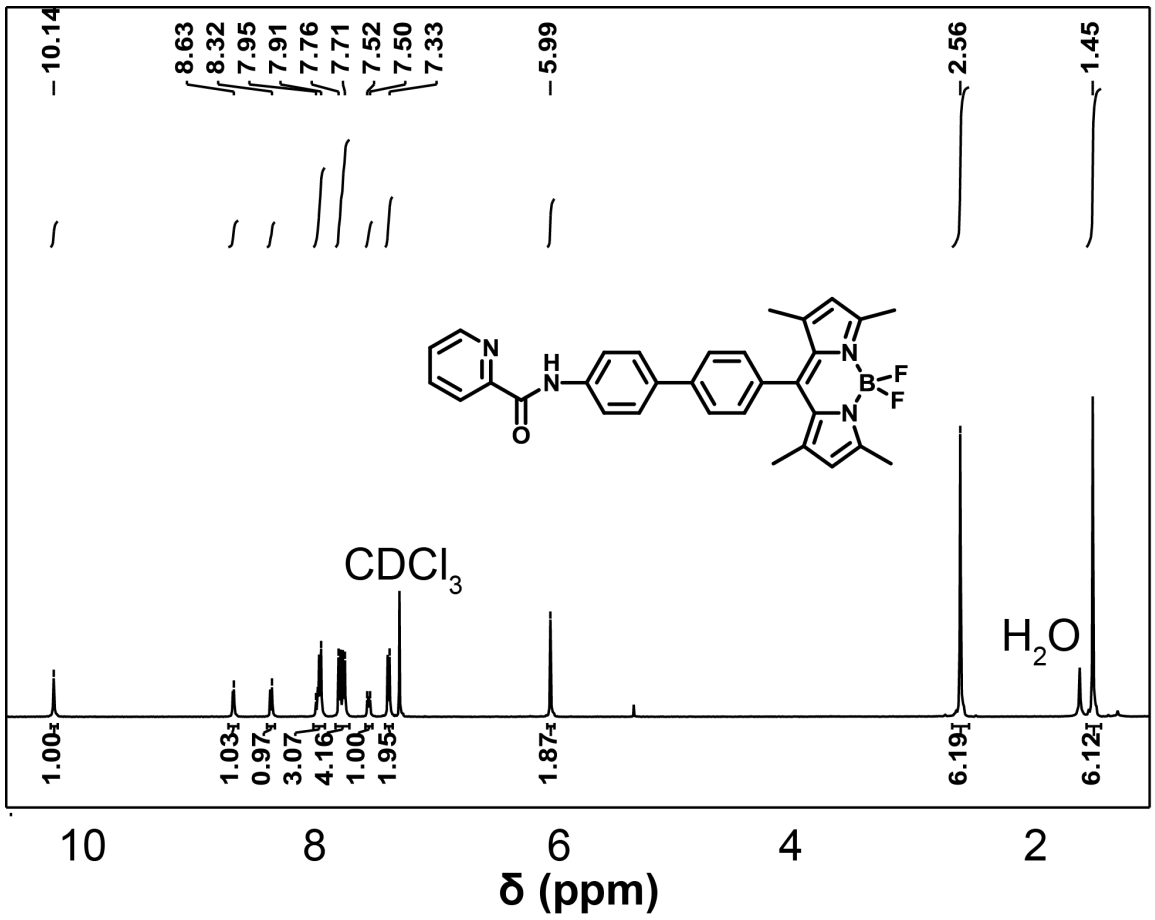

Figure S3. ^{1}H NMR spectrum (500 MHz, $CDCl_3$) of compound **4A.**

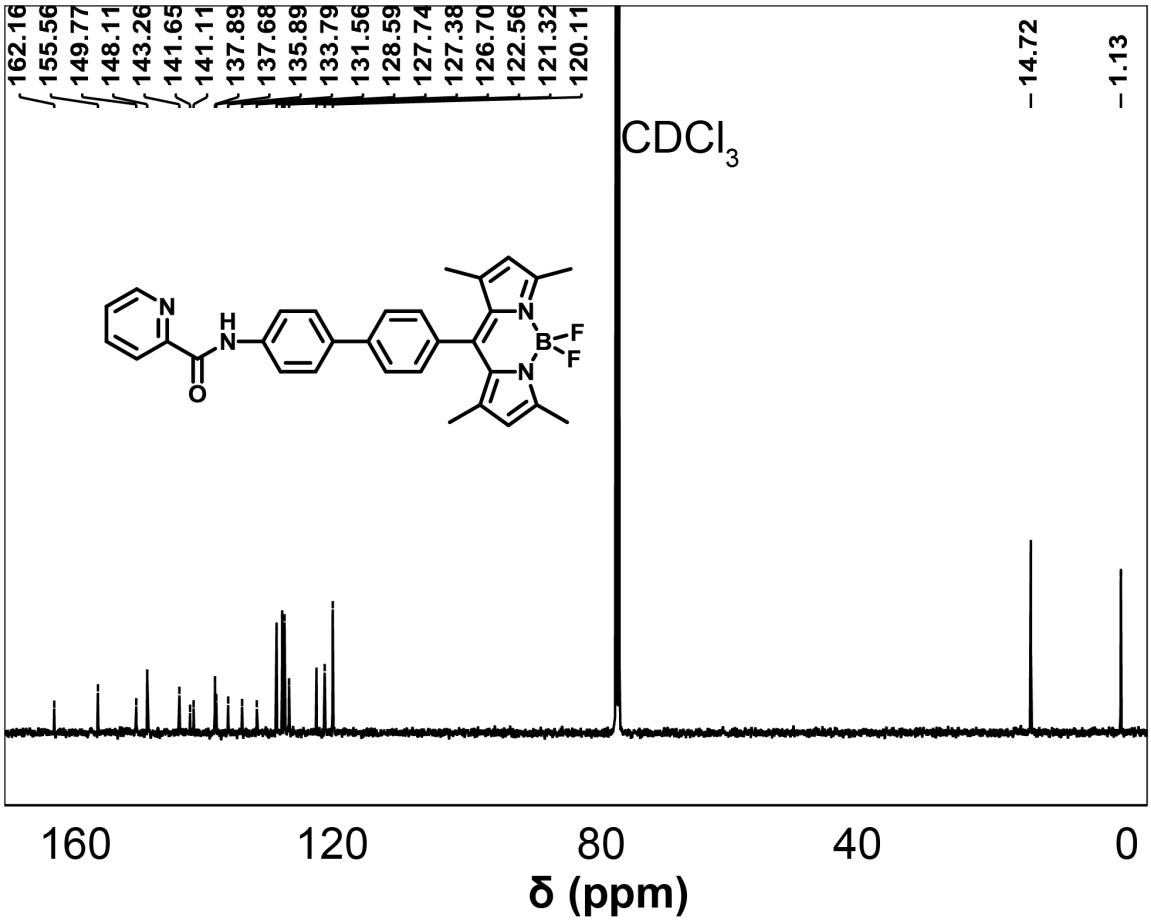

Figure S4. ^{13}C NMR spectrum (125 MHz, $CDCl_3$) of compound **4A**.

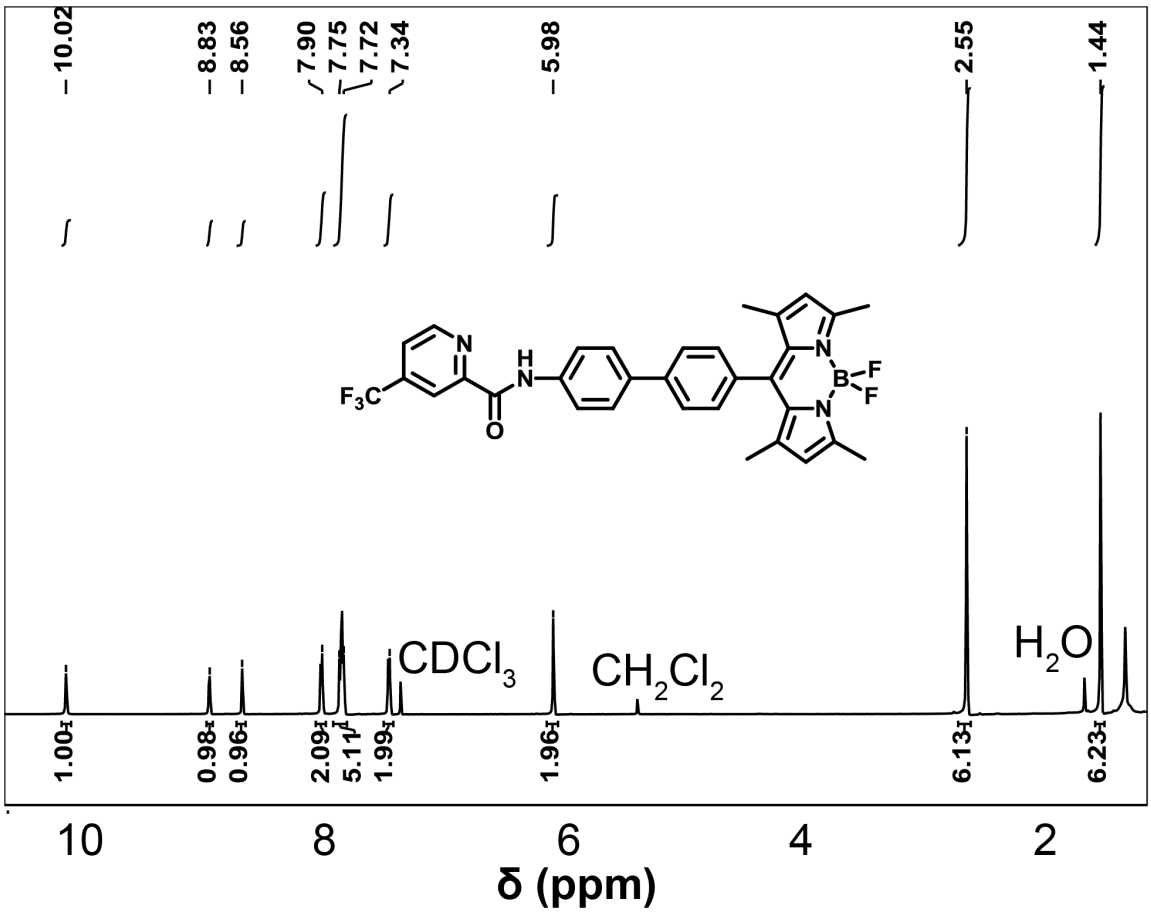

Figure S5. ^{1}H NMR spectrum (600 MHz, $CDCl_3$) of compound **4B**.

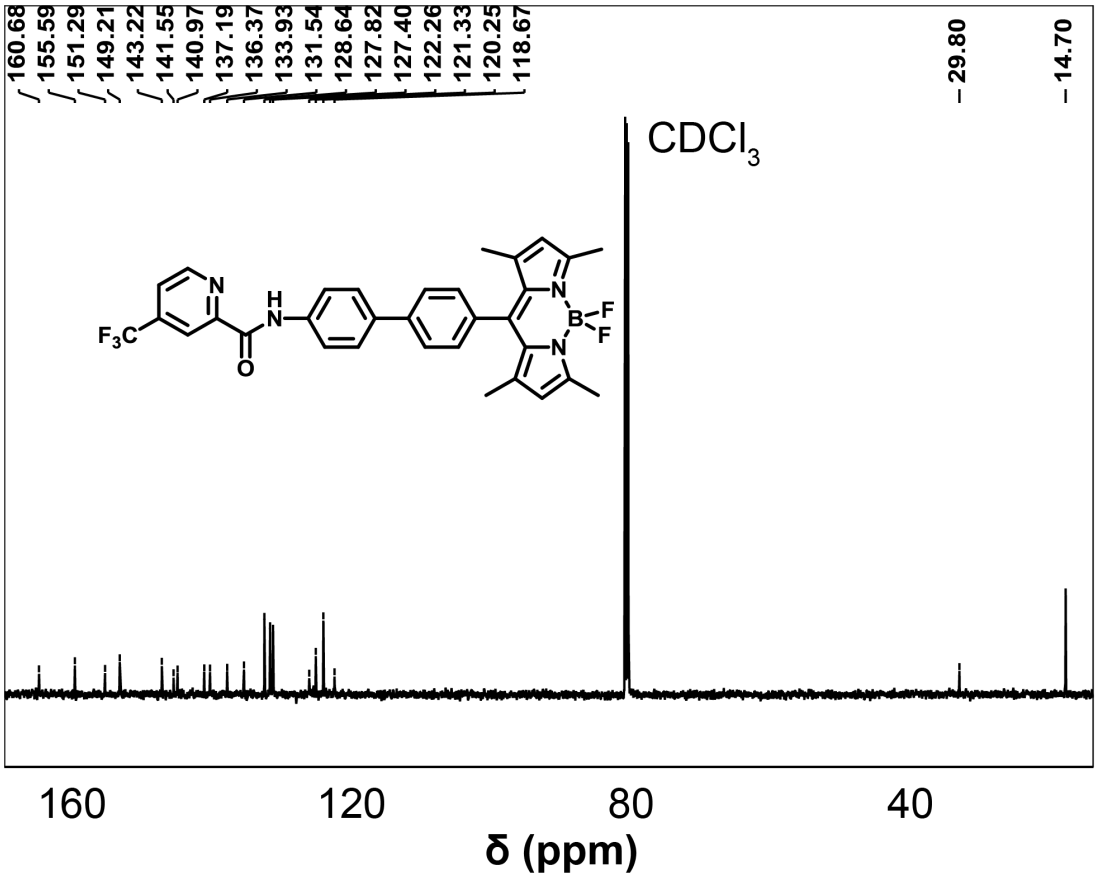

Figure S6. ^{13}C NMR spectrum (600 MHz, $CDCl_3$) of compound **4B**.

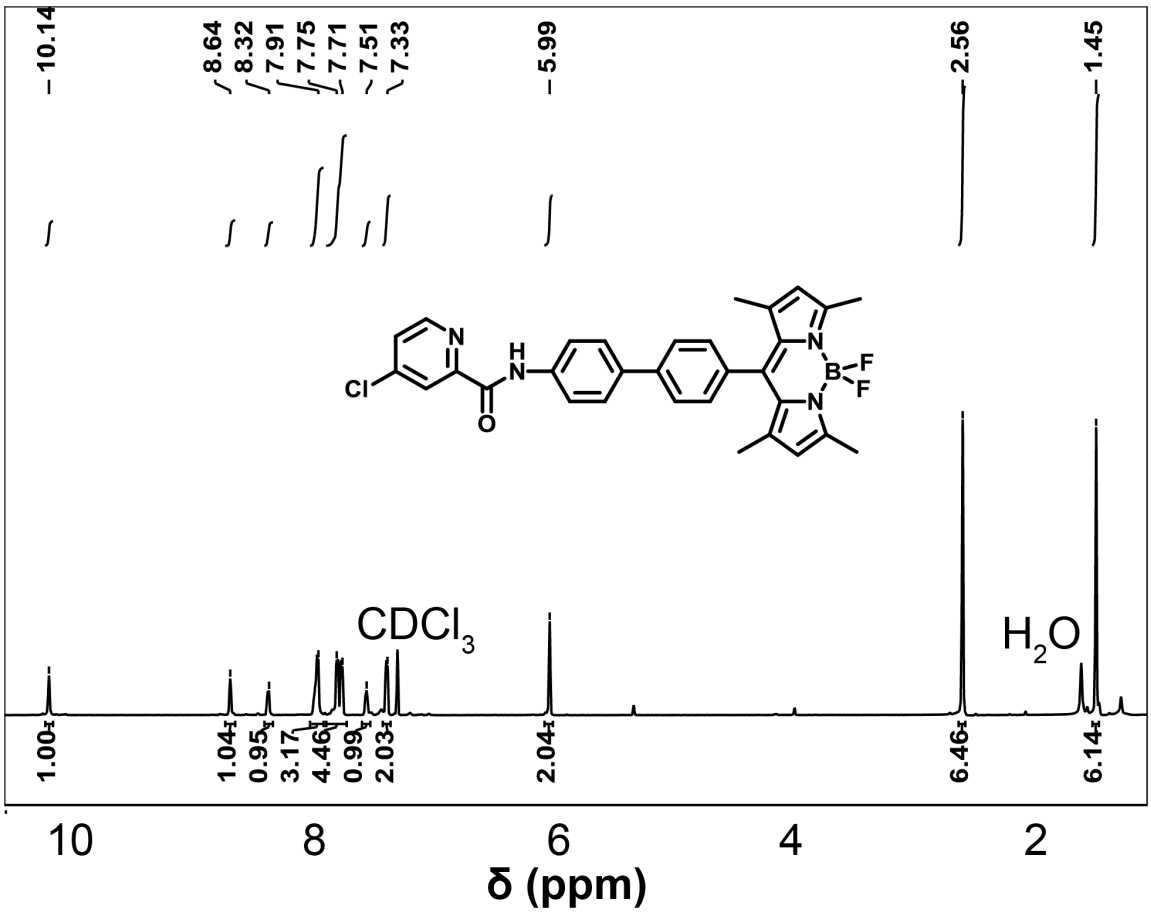

Figure S7. ^{1}H NMR spectrum (600 MHz, $CDCl_3$) of compound **4C**.

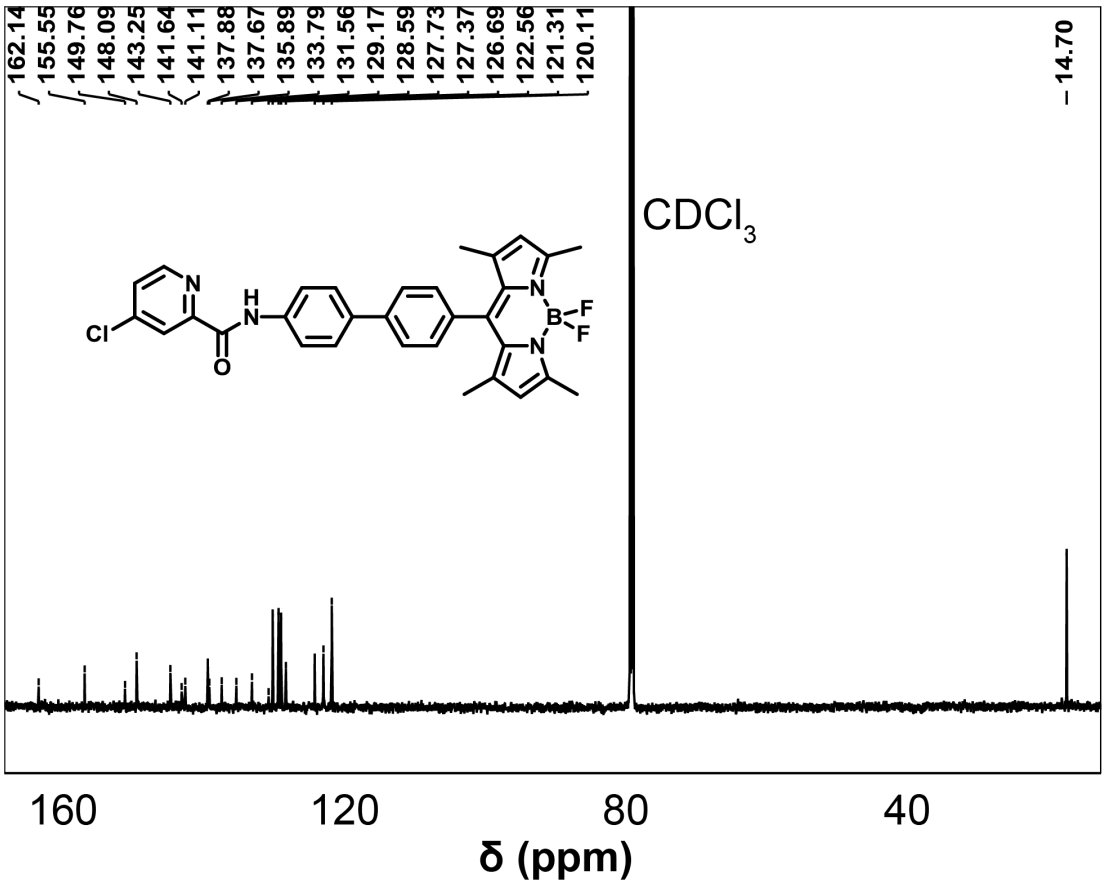

Figure S8. ^{13}C NMR spectrum (600 MHz, $CDCl_3$) of compound **4C**.

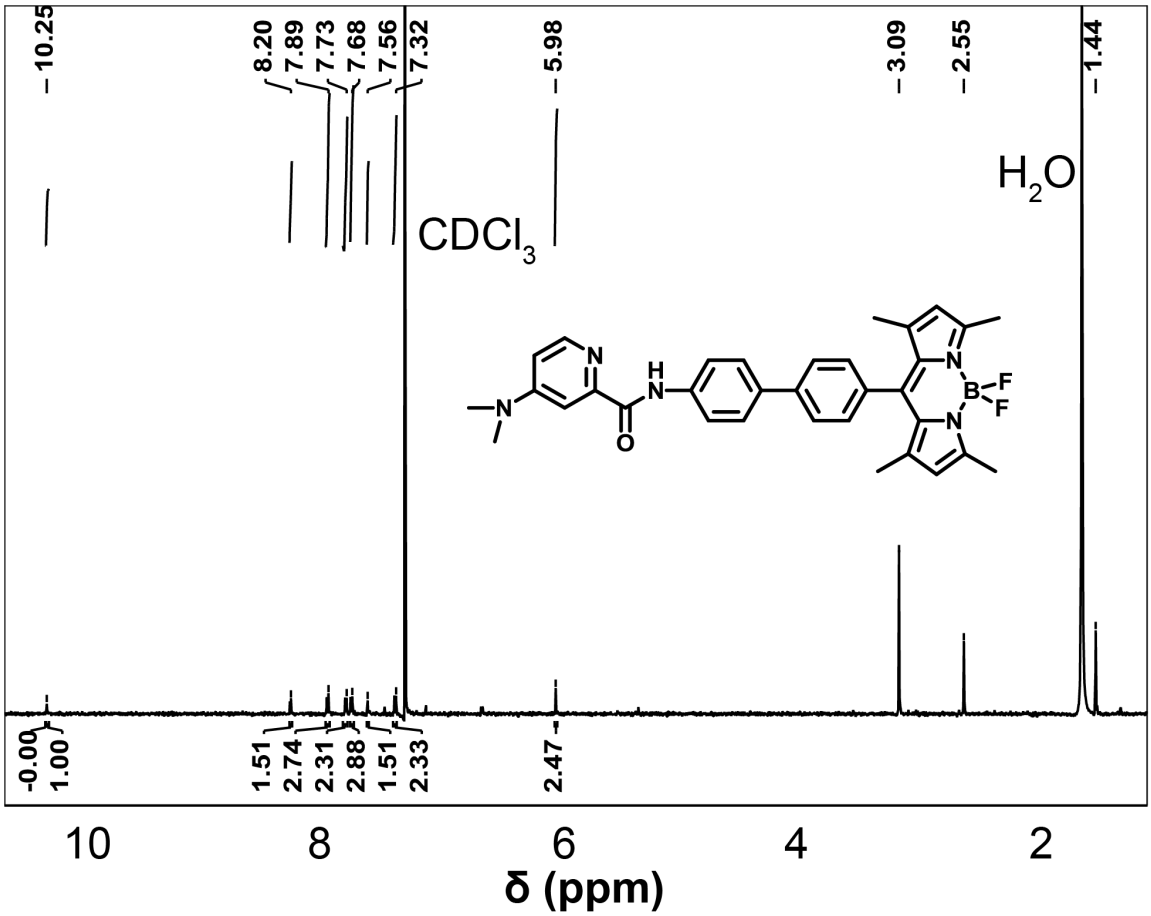

Figure S9. ^{1}H NMR spectrum (600 MHz, $CDCl_3$) of compound **4D**.

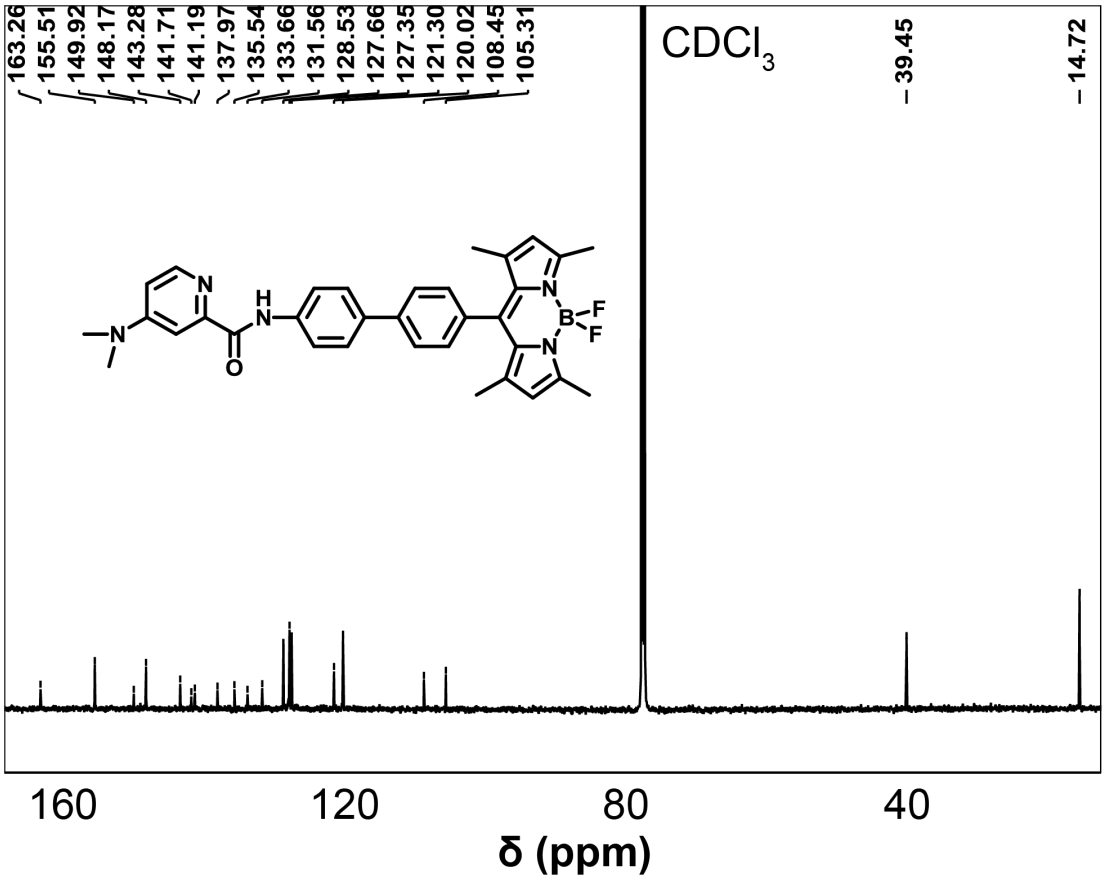

Figure S10. ^{13}C NMR spectrum (600 MHz, $CDCl_3$) of compound **4D**.

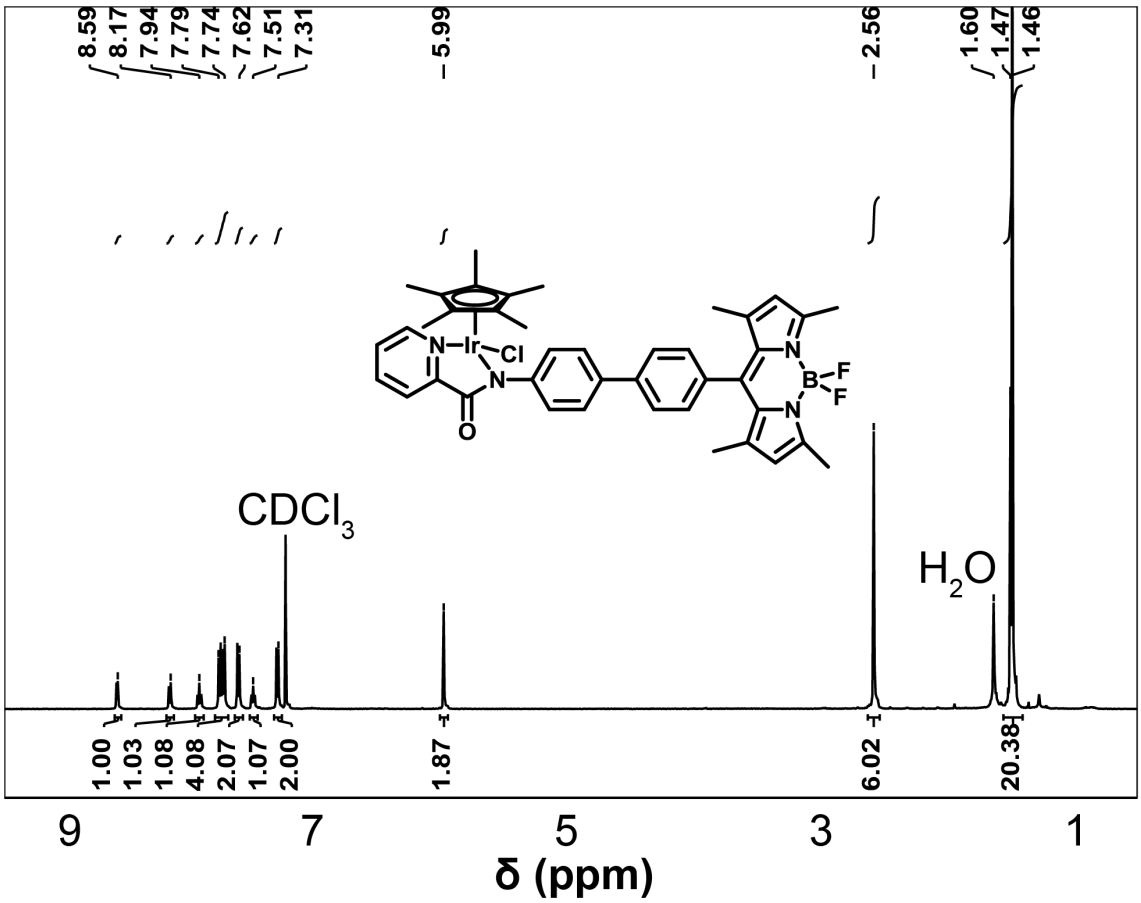

Figure S11. ^{1}H NMR spectrum (500 MHz, $CDCl_3$) of **Ir1'**.

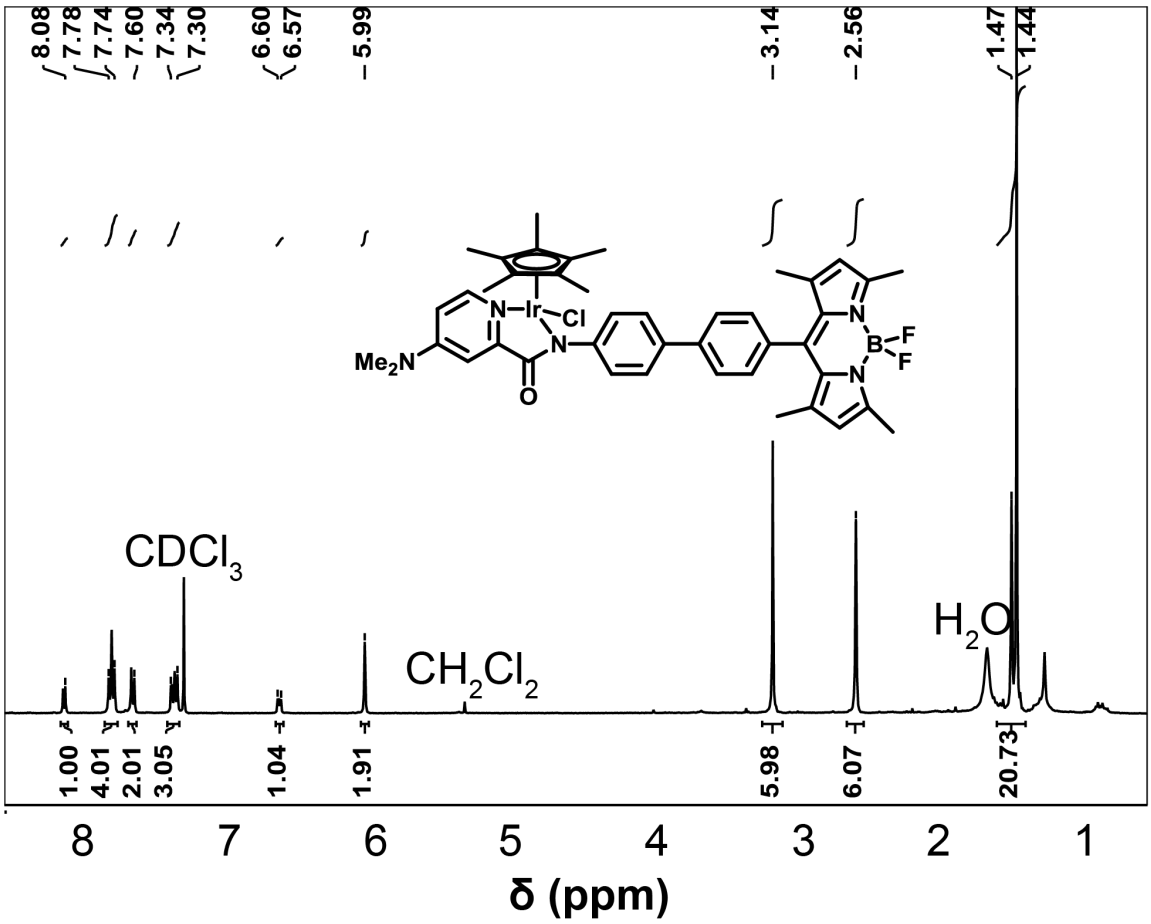

Figure S12. ^{1}H NMR spectrum (400 MHz, $CDCl_3$) of **Ir4'**.

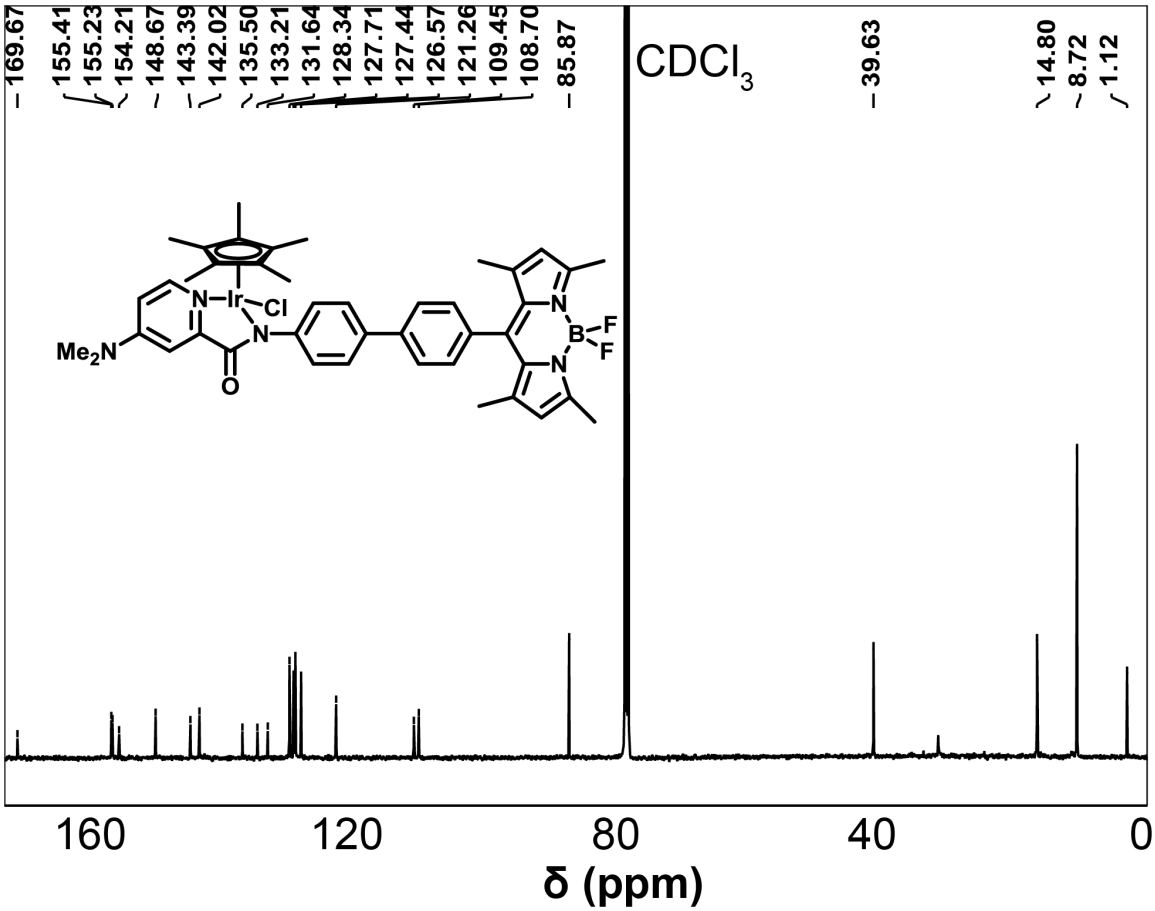

Figure S13. ^{13}C NMR spectrum (125 MHz, $CDCl_3$) of **Ir4'**.

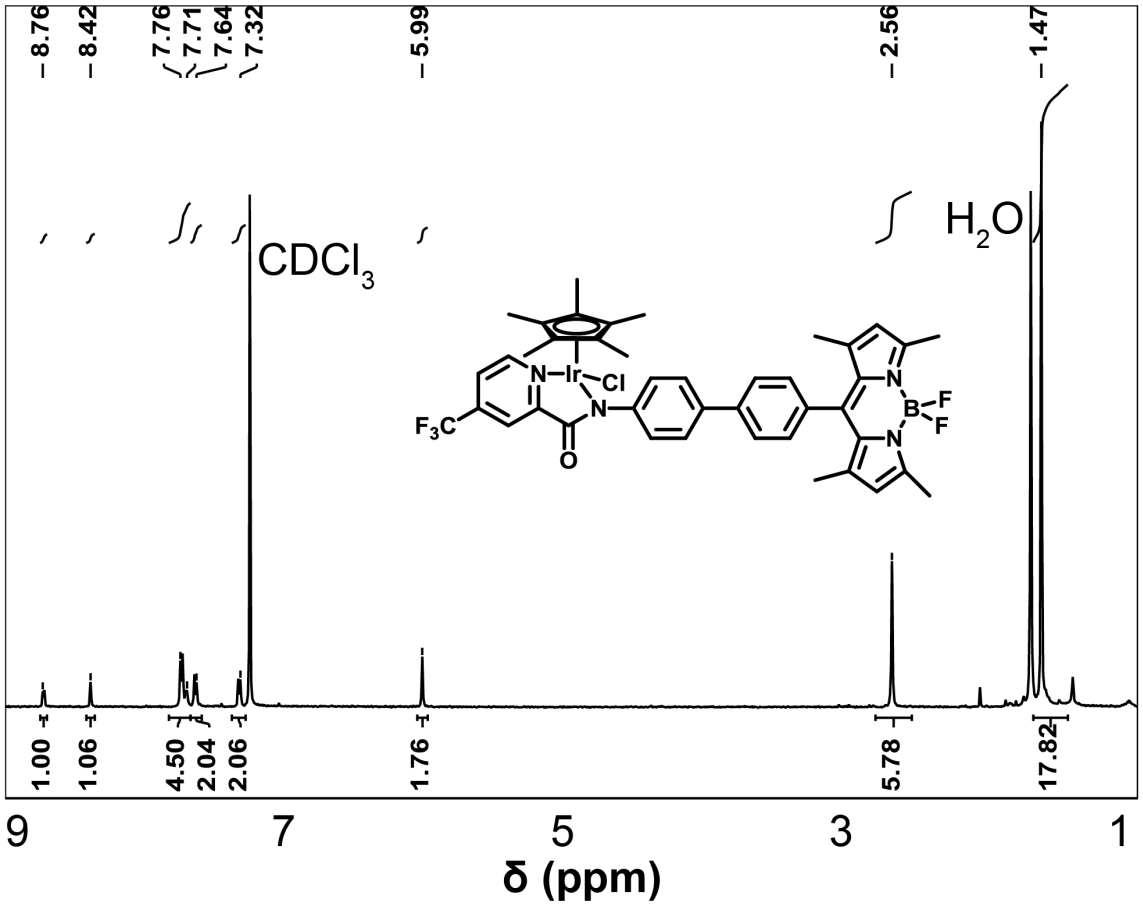

Figure S14. ^{1}H NMR spectrum (500 MHz, $CDCl_3$) of **Ir5'**.

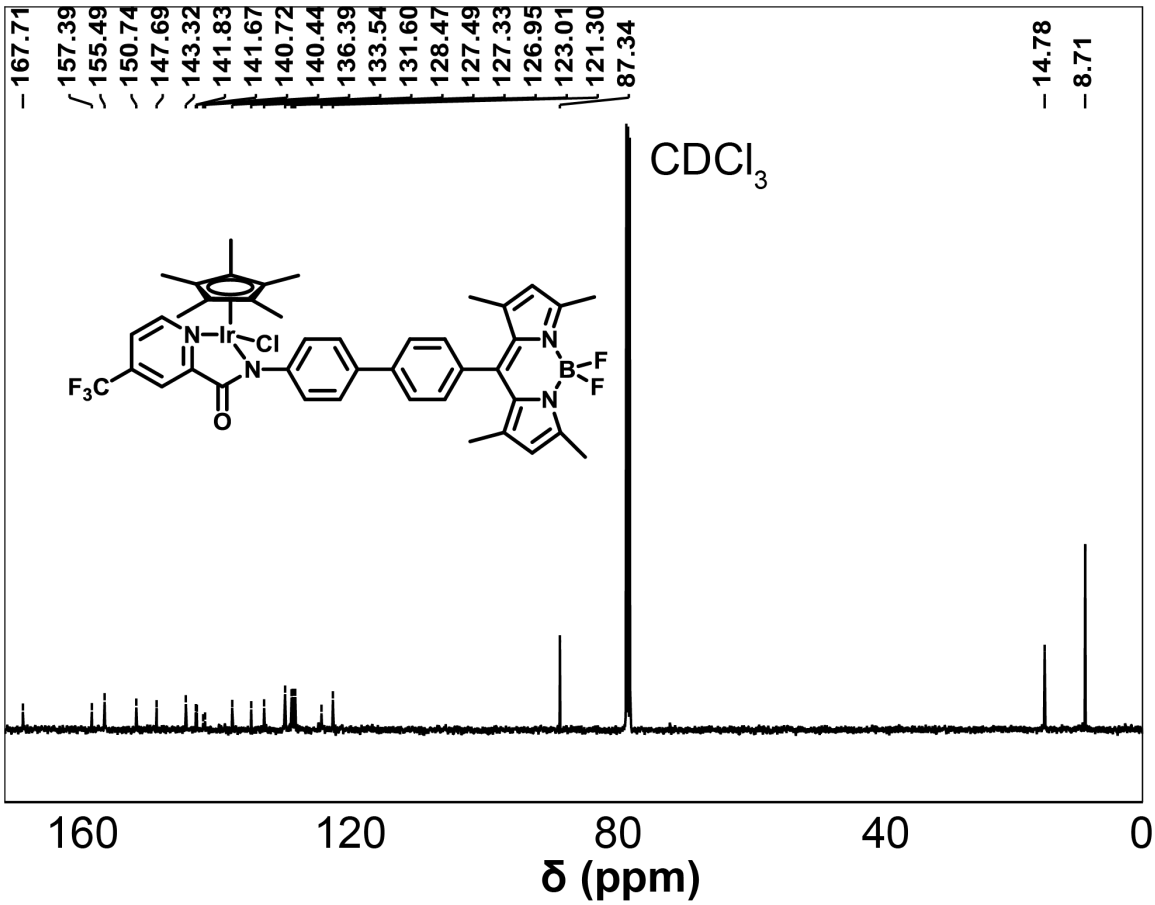

Figure S15. ^{13}C NMR spectrum (125 MHz, $CDCl_3$) of **Ir5'**.

CHAPTER 4. Toward the Discovery of Biocompatible Cobalt Transfer Hydrogenation Catalysts and New Off-On Probe for Reaction-Based Detection

4.1. Introduction

Most catalytic transfer hydrogenation reactions performed in air rely on precious metal catalysts comprising metals such as rhodium, ruthenium, and iridium.[1,2] unfortunately, these metal are typically more expensive and less abundant than first row transition metals. For example, there is 1000 times more cobalt in the earth's crust than all of the metals combined.[3] Additionally, cobalt can access multiple oxidation and spin states so it could potentially achieve different reactivity than that of the precious metals.

Homogeneous Co complexes have been shown to be capable of catalyzing a variety of chemical transformations.[4-12] Co is also an important element in human health,[13] since it's present in the cofactor vitamin B_{12}.[14] Due to its biocompatibility, Co complexes have been used in imaging agents,[15] drug-delivery scaffold,[16] anti-cancer agents,[17] enzyme inhibitors[18] and anti-viral drugs.[19] Co has also been explored in catalytic transfer hydrogenation for the conversion of aldehydes or ketones to alcohols. Co catalyzed transfer hydrogenation to reduce ketones was first reported by Lemaire *et. al.* in 1997.[20] Reduction of acetophenone was achieved by a diamine Co(II) dichloride complex (**Co1**) in isopropanol as a hydride donor at RT. The catalytic reaction produced the desired product only in 8% yield after 6 d in the presence of 20 mol% KOtBu. In 2013 Hanson *et. al*. reported transfer hydrogenation involving a series of aldehydes and ketones at RT using isopropanol as the hydride source in THF by Co(II) complexes (**Co2**) supported by PNP ligands.[21] The corresponding alcohols were obtained in more than 90% yield after 24 h in base free reaction conditions. The same catalyst **Co2** was also reported to catalyze acceptorless alcohol dehydrogenation in toluene at 120°C yielding the corresponding aldehyde or ketone in moderate to good yield in 24 h.[22] To the best of our

knowledge, there are no reports of a Co catalyst that can promote transfer hydrogenation for the reduction of aldehyde or ketone at physiologically relevant temperature 37°C in aqueous media using formate or other biologically compatible molecule as the hydride source.

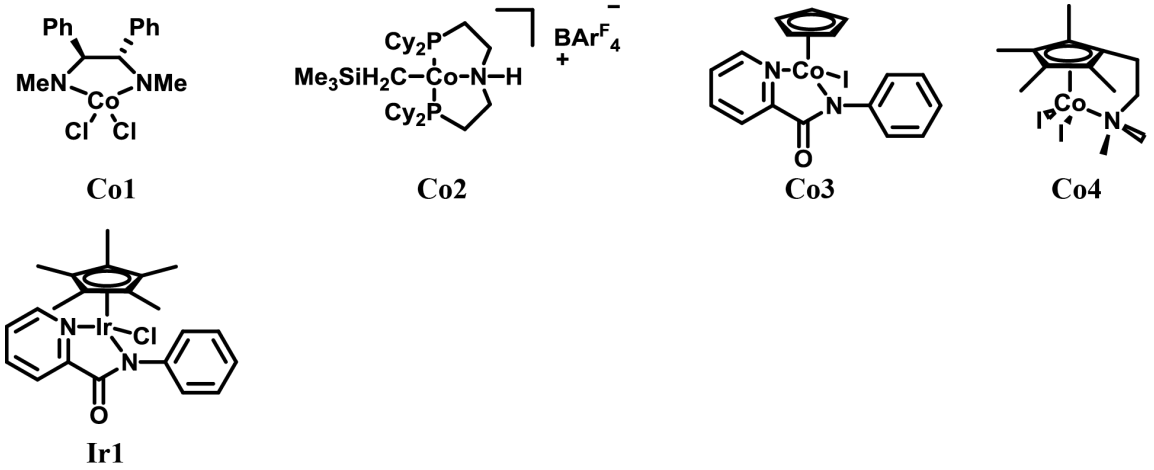

Chart 1. Structure of **Co1**, **Co2**, **Co3**, **Co4**, and **Ir1**.

Here we describe our efforts to design and synthesize a biocompatible Co(III) transfer hydrogenation catalyst, which necessitates that it must be active at 37°C in heterogeneous aqueous environments. Formate will be tested first as the hydride source but we will also evaluate the use of nicotinamide adenine dinucleotide phosphate (NADH) for biological studies. We have chosen Co(III) as a substitute for Ir(III) because it belongs in the same group in the periodic table and might exhibit similar reactivity. However, since Co(III) is more substitutionally labile than Ir(III), we anticipate hat strongly chelating bonds are needed to stabilize Co(III) in aqueous media.

We will also develop new off-on substrate probes for intracellular studies to visualize transfer hydrogenation reactions take place inside living cells in real time.

These fluorogenic compounds will enable us to map the cellular localization of the alcohol products. Toward this goal, we have synthesized a bodipy based off-on probe due to the excellent spectroscopic properties of bodipy dyes; (narrow Gaussian-shaped absorption and emission bands, high molar extinction coefficients and quantum yield values, excellent photostability).[23-25]

4.2. Results and Discussion

4.2.1. Synthesis of Co(III) Complexes

The Co(III) analogue of **Ir1** was synthesized using Cp ligand (**Co3**) (Scheme 1). This dark green Co(III) complex was characterized by IR and NMR spectroscopy (Figure S1). The N-H stretch (≈ 3300 cm^{-1}) of the ligand was absent in the complex suggesting the formation of Co(III) species. **Co3** is insoluble in water but is stable in methanol for several days as observed by ^{1}H NMR spectroscopy. **Co3** also shows excellent thermal stability since it was intact even after heating at 100°C for 20 min in MeOH-d_4 (Figure S2). **Co3** was initially evaluated for transfer hydrogenation of benzophenone in methanol in the presence of 0.3 equiv. of KOH at 100°C. Unfortunately, no products were detected by GC-FID after 3 h of reaction with 1 mol% of catalyst (250 μM concentration). **Co3** was also tested for transfer hydrogenation of 3-methyl-2-cyclohexenone in ^{i}PrOH/MeOH (4:1) methanol in the presence of 0.5 equiv. of KOH at 100°C. No product was detected by GC-FID after 3 h of reaction with 1 mol% of catalyst (360 μM concentration). **Co3** was tested for transfer hydrogenation of benzaldehyde (5 mM) in aqueous media with 20% acetonitrile as co-solvent at 40°C using 3 equiv. of sodium formate as the hydride donor. No benzyl alcohol product was detected in GC-FID after 24 h of reaction with 2

mol% (100 μM) or 8 mol% (400 μM) catalyst **Co3** (Figure 3). Because the **Co3** solution became colorless after several hours, it appeared that the complex had decomposed during this time period.

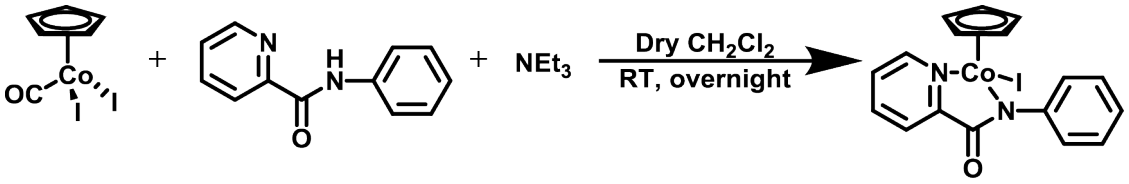

L3 **Co3**

Scheme 1. Synthesis of **Co3**.

Co3 was also tested for acceptorless dehydrogenation of secondary alcohol 3-methyl-2-cyclohexene-1-ol to the corresponding ketone. 3-methyl-2-cyclohexene-1-ol was treated with 10 mol% of catalyst in acetone at 40°C for 24 h. No product was formed as confirmed by GC-FID (Figure 4).

To enhance the structural stability of **Co3**, we considered adding a pendant donor such as alkenes,[26] phosphenes,[27] ethers, thioethers, and ester groups[28] to the Cp ring that can also bind to cobalt.

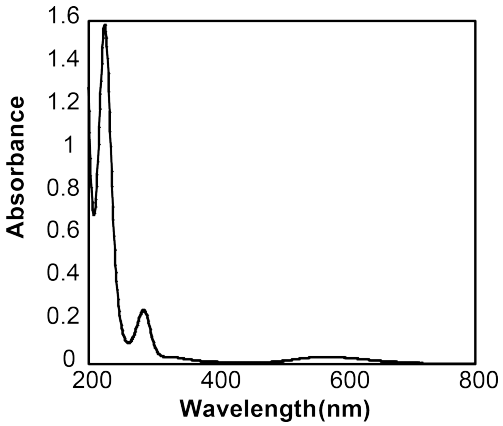

Figure 1. UV-Vis spectrum of **Co4** (200 μM) in water.

We selected to test the catalytic activity of a previously reported **Co4** complex.[29] The Co(III) center in **Co4** is stabilized by Cp* attached with a dimethyl amino pendant side chain. **Co4** forms purple solution in most of the solvents (dichloromethane, acetonitrile, water) indicating the displacement of dimethyl amino group by solvent molecule[29] and the purple solution shows absorbance at 286, 332 and 569 nm in water (Figure 1). **Co4** was evaluated for transfer hydrogenation of benzaldehyde using 3 equiv. of HCOONa in aqueous media with 20% acetonitrile as co-solvent at 40°C. The reaction products were analyzed by GC-FID but no benzyl alcohol product was detected after 24 h with 2 mol% (100 μM) or 8 mol% (400 μM) catalyst **Co4** (Figure 3).

Co4 was also tested for acceptorless dehydrogenation of secondary alcohol 3-methyl-2-cyclohexene-1-ol to the corresponding ketone. 3-methyl-2-cyclohexene-1-ol (89.15 mM) was treated with 2 mol% of catalyst at 1.78 mM concentration at 40°C for 20 h in different solvent systems. The same reaction was repeated in 100% acetone, 100% water and H_2O/^{t}BuOH (1:1). No products were formed under any of these reaction conditions (Figure 4).

4.2.2. Proposed Structure for Stable Co(III) Complex in Solution

The binding strength between Co(III) and the donor atom of pendant side chain depends on the electron donating ability of the coordinating atom.[29] Here we propose a new ligand design for Co(III) complex with a pendant amine chain with more electron donating groups, which we expect to impart more electron density on N atom, thereby increasing Co(III)-N bond stability in solution due to the higher σ donation ability of the coordinating N atom (**Co5**) (Chart 2). It has been reported that Co(III)-N bond lengths are shorter for unsubstituted cyclopentadienyl Co(III) complexes than those of substituted cyclopentadienyl Co(III) complexes.[30] As we intend to apply these complexes in cells to carry out aldehyde reduction and hydrophobicity of complexes enhance their cellular uptake, we chose to design complex with methyl substituted cyclopentadienyl ligand. This new Co(III)complex will be tested for transfer hydrogenation to reduce aldehyde *in-vitro* using formate and NADH as the hydride donor and subsequently be used in live cells for aldehyde reduction using intracellular NADH.

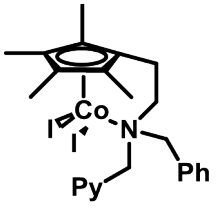

Co5

Chart 2. Proposed structure of **Co5**.

4.2.3. Evaluation of an Off-On Probe

To visualize the formation and localization of the transfer hydrogenation products in cells, an off-on probe was synthesized. This turn on fluorescent probe was designed

such a way that the substrate probe (functionalized with aldehyde) would be non-emissive and would start emitting upon reduction to alcohol, which would allow us to detect product selectively over starting material in cells. A bodipy aldehyde probe **Pr1** was synthesized with aldehyde group according to a literature procedure.[31] The reduced derivative **Pr2**, which contains an alcohol group, was also prepared.[32] **Pr1** showed absorbance at 512 nm and gave no emission when excited with 480 nm in ^{t}BuOH/H_2O (1:4). **Pr2** showed absorbance at 514 nm and gave strong emission at 532 nm when excited with 480 nm in ^{t}BuOH/H_2O (1:4) (Figure 2a). Due to such difference in the photophysical properties between **Pr1** and **Pr2**, this system could be used as an off-on probe for monitoring transfer hydrogenation in live cell using intracellular NADH as hydride donor.

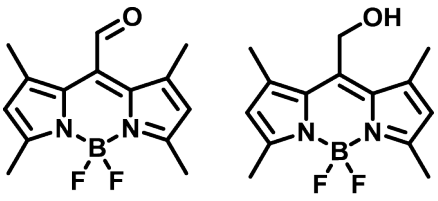

Pr1 **Pr2**

Chart 3. Structure of **Pr1** and **Pr2**.

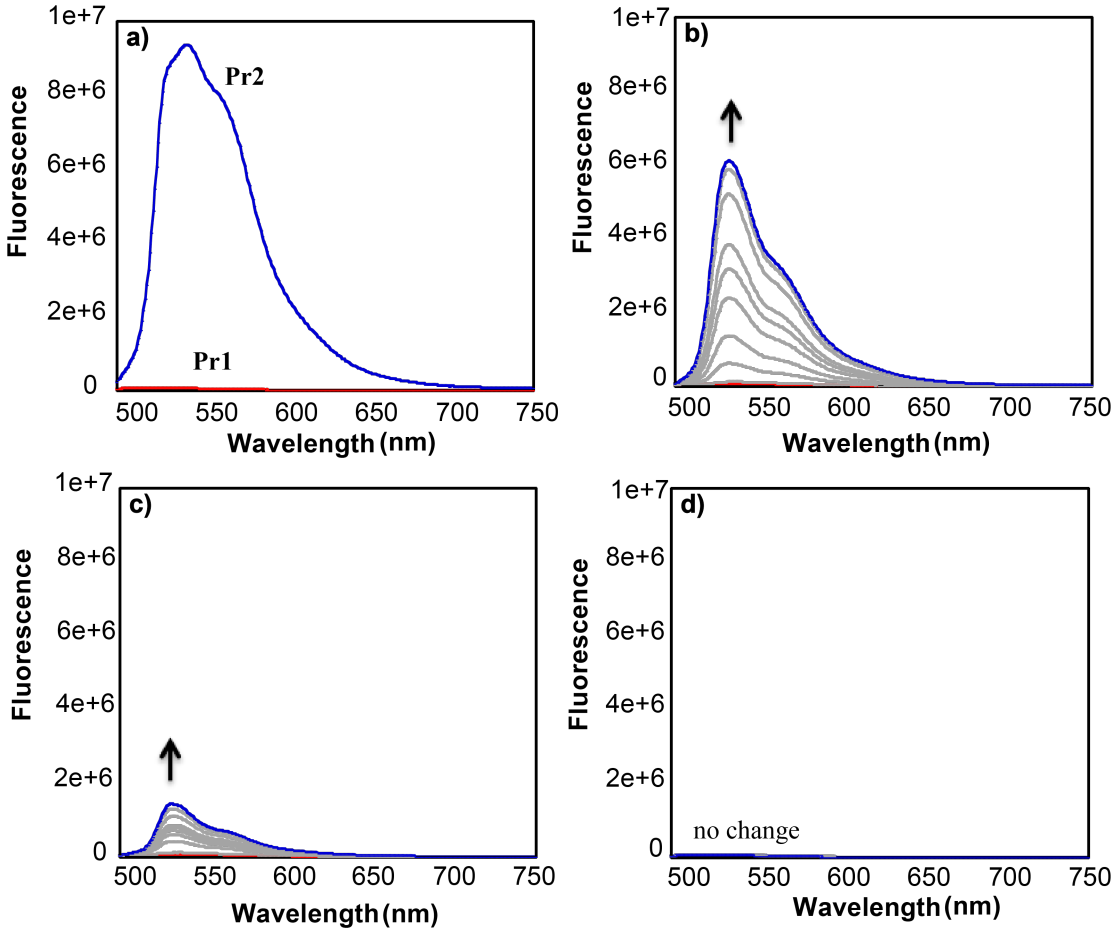

Figure 2. a) Emission spectra (λ_{ex} = 480 nm) of 30 μM **Pr1** (red) and **Pr2** (blue) in ^{t}BuOH/H_2O (1:4); Fluorescence spectra (λ_{ex} = 480 nm) obtained from the reaction of **Pr1** (30 μM) and NADH (100 μM) in the presence of either b) 1 μM **Ir1** c) 1 μM **Ir3** d) 30 μM $IrCl_3$. 3H2O in ^{t}BuOH/H_2O (1:4) at RT under air. The spectral changes were recorded at different time intervals from 0 h (red trace) to 4 h (blue trace).

Pr1 was evaluated as a possible substrate for transfer hydrogenation. When **Pr1** was treated with 2 mol% **Ir1** (20 μM) in ^{t}BuOH/H_2O (2:3) at 40°C in the presence of 2 equiv. of NADH as the hydride donor, around 2.5% of product and 3% of remaining starting material were detected in GC-MS after 20 h. Higher detection limit of GC-MS could be the reason for inefficient detection of very low concentration of product and

substrate, which necessitates to switch to a different analytical method with much lower detection limit to analyze reaction products of very low concentration efficiently. A calibration curve of emission was prepared using different concentration of **Pr2** in fluorometer (Figure 5a) and the curve was fit into a single exponential rise (Figure 5b). Several cuvette studies were performed to determine the amount of **Pr2** formed when 30 μM **Pr1** was treated with different concentration of **Ir1** in presence of physiological NADH concentration (100 μM) in ^{t}BuOH/H_2O (1:4) at RT in air (Figure 2b) (Table 1).

Table 1. Maximum amount of **Pr2** formed at the corresponding time for different concentration of **Ir1**.

[**Ir1**] (μM)	Time	Yield of **Pr2** (μM)
0	4 h	0
1	4 h	7.56
2	4 h	6.24
10	45 min	7.91
20	30 min	5.54
30	45 min	6.21

It is evident from the above result that limited amount of **Pr2** (≈ 22%) was formed irrespective of **Ir1** concentration (Table 1). Different concentration of **Ir1** only changed the rate of the reaction but could not improve the yield; this may be due to the limiting concentration of the substrate. Control studies were performed with Iridium precursor **Ir3** and iridium salt $IrCl_3$. $3H_2O$ to confirm the effect of **Ir1** in **Pr1** reduction. No change in

emission spectra was observed with 30 μM of $IrCl_3$. $3H_2O$ even after 4 h (Figure 2d). Lower concentration of **Pr2** (≈ 10%) was formed at a much slower rate with **Ir3** compared to **Ir1** (Table 2) (Figure 2c), confirming the effect of **Ir1** as catalyst in hydride transfer from NADH.

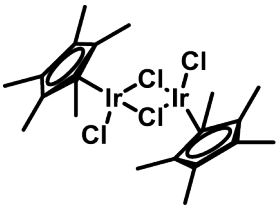

Ir3

Chart 4. Structure of **Ir3**.

Table 2. Maximum amount of **Pr2** formed at the corresponding time for different concentration of **Ir3**.

[**Ir3**] (μM)	Time	Yield of **Pr2** (μM)
1	4 h	1.28
5	4 h	3.94
10	4 h	3.79
15	4 h	4.06

Biocompatibility of these probes was measured in terms of IC_{50} before applying them in living systems. **Pr1** has already been reported to be non-toxic.[39] The IC_{50} of **Pr2** was found to be more than 250 μM when NIH3T3 cells were treated with **Pr2** for 3 h. The reactions of **Pr1** with **Ir1** were carried out on live NIH-3T3 mouse embryo fibroblast cells. NIH3T3 cells were treated with **Pr1**, washed with fresh media and then treated with

Ir1. After treating the cells with **Ir1**, cells were washed twice with fresh media and PBS before subjected to lysis with cold solvent mixture of acetonitrile/methanol/water (2:2:1). The fluorescence of the cell lysate was believed to be directly proportional to the formation of **Pr2** as **Pr1** and **Ir1** are non-emissive. No fluorescence was detected in cell lysate when NIH3T3 cells were incubated with 30 μM of **Pr1** for 4 h and then exposed to a solution containing 2 μM of **Ir1** for 2 h. Treatment of NIH3T3 with higher concentration of **Pr1** (100 μM, 2 h)/**Ir1** (5 μM, 2 h), **Pr1** (100 μM, 2 h)/**Ir1** (10 μM, 2 h), **Pr1** (100 μM, 2 h)/**Ir1** (20 μM, 2 h) did not enhance fluorescence intensity. To our surprise, cell lysate of NIH3T3 cells those were treated with 30 μM of **Pr2** didn't emit at all. Further investigation revealed that only 1.36% and 5.8% of total **Pr2** in culture media could only permeate through NIH3T3 cell membrane when cells are treated with 100 μM and 200 μM **Pr2** for 2 h, respectively.

Furthermore, to evaluate the cellular retention of **Pr2**, cells were treated with 100 μM of **Pr2** for 2 h and then the culture media was subjected to fluorescence analysis every 30 min. Amount of **Pr2** in culture media was found to be same as the amount of **Pr2** that permeated through cell membrane in one hour, which indicates poor cell retention of **Pr2**. Although, **Pr2** showed higher permeability (15.8%) through A549 cell membrane and higher cellular retention in A549 cells, no product was detected in the cell lysate from the reaction **Pr1** (200 μM)/**Ir1** (30 μM) on live A549. Steric congestion of aldehyde group in **Pr1** by two neighboring methyl groups makes **Pr1** a bad substrate for transfer hydrogenation. Decomposition of the probe **Pr1** from the reaction of intracellular cysteine or homocystein could be the reason for **Pr1**/**Ir1** system to not work in live cells.

4.3. Conclusions

We have synthesized several Co(III) catalysts and evaluated their abilities as transfer hydrogenation catalysts. Both catalysts failed to reduce aldehyde/ketone to corresponding alcohol or to oxidize alcohol to corresponding aldehyde/ketone. We believe that these complexes are susceptible to decomposition in polar solvents. A stronger σ donor ligand is expected to form stronger coordination bond with Co(III), thereby, stabilizing the complex in solution. We have proposed a new ligand design, which we expect to impart more electron density on metal center and overcome the problem of dissociation of complex in solution. We have also evaluated one off-on probe as a possible substrate for transfer hydrogenation in living system. The sterically hindered position of the aldehyde group makes this probe a poor substrate even in the reaction flask. Furthermore, this bodipy-aldehyde compound does not appear to be readily taken up by cells and have poor cell retention.

4.4. Experimental Section

4.4.1. General Procedures

Commercial reagents were used as received without further purification. All air- and water-sensitive manipulations were performed using standard Schlenk techniques or under a nitrogen atmosphere using a glovebox. Anhydrous solvents were obtained from an Innovative Technology solvent drying system saturated with Argon. **L3** was synthesized according to literature procedures.[33] $CoCp(CO)I_2$[34], **Ir1**,[35] and **Ir3**[36] were synthesized according to literature procedures. NIH-3T3 mouse fibroblast and A549 human epithelial cells were obtained from ATCC.

Physical Methods. NMR spectra were acquired using JEOL spectrometers (ECA-400, 500, and 600) at room temperature and referenced using residual solvent peaks. A Horiba Fluoromax 4 fluorometer was used to record emission spectra. Gas chromatography-mass spectrometry was performed using an Agilent 7890 GC/5977A MSD instrument equipped with an HP-5MS capillary column. IR spectra were measured using a Thermo Nicolet iS10 FT-IR spectrometer.

4.4.2. Synthesis

[CpCo(N-phenyl-2-pyridinecarboxamidate)Cl] (Co3)

In a schlenk flask, **L3** (0.01 g, 0.06 mmol, 1.0 equiv.) and $CpCo(CO)I_2$ (0.03 g, 0.03 mmol, 1.0 equiv.) were com bined in dry DCM (15 mL) at RT under N_2. Triethylamine (0.01 mL, 0.07 mmol, 1.2 equi v.) was added and the reaction mixture was stirred overnight under N_2 at RT. Ether was added to yield a dark green precipitate, which was then isolated by filtration, and then washed with ether for three times to yield pure product. ^{1}H NMR (400 MHz, CD_3OD): 9.97 (d, J = 4 Hz, 1H), 8.08 (td, J = 16 Hz, 1H), 7.92 (d, J = 4 Hz, 2H), 7.84 (d, J = 8 Hz, 1H), 7.70 (td, J = 12 Hz, 1H), 7.44 (t, J = 8 Hz, 2H), 7.26 (t, J = 8 Hz, 1H), 5.39 (s, 4H) IR: v (cm^{-1}) = 3000, 1617, 1595, 1584, 1387, 850, 830, 761, 752, 704, 695, 679, 594.

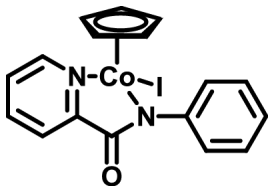

4.4.3. General Procedure for Transfer Hydrogenation of Ketone by Co3 (GC Yield)

The appropriate volumes of the following stock solutions were combined in a 20 mL scintillation vial: ketone, KOH, and **Co3**. The mixture was then diluted with the desired solvent. The reaction vial was tightly sealed with a screw cap and allowed to proceed at

100 °C for 3 h. The solution was then filtered through a pipette plug containing celite and the sample was analyzed by GC.

4.4.4. General Procedure for Transfer Hydrogenation of Aldehyde by Co3 and Co4 (GC Yield)

The appropriate volumes of the following stock solutions were combined in a 20 mL scintillation vial: aldehyde, sodium formate, and [**Co**]. The mixture was then diluted with the desired solvent. The reaction vial was tightly sealed with a screw cap and allowed to proceed at 40°C for 24 h. After 24 h, biphenyl (0.55 equiv. relative to the aldehyde) was added and the reaction mixture was further diluted with 5 mL of acetonitrile. Sample was then analyzed by GC.

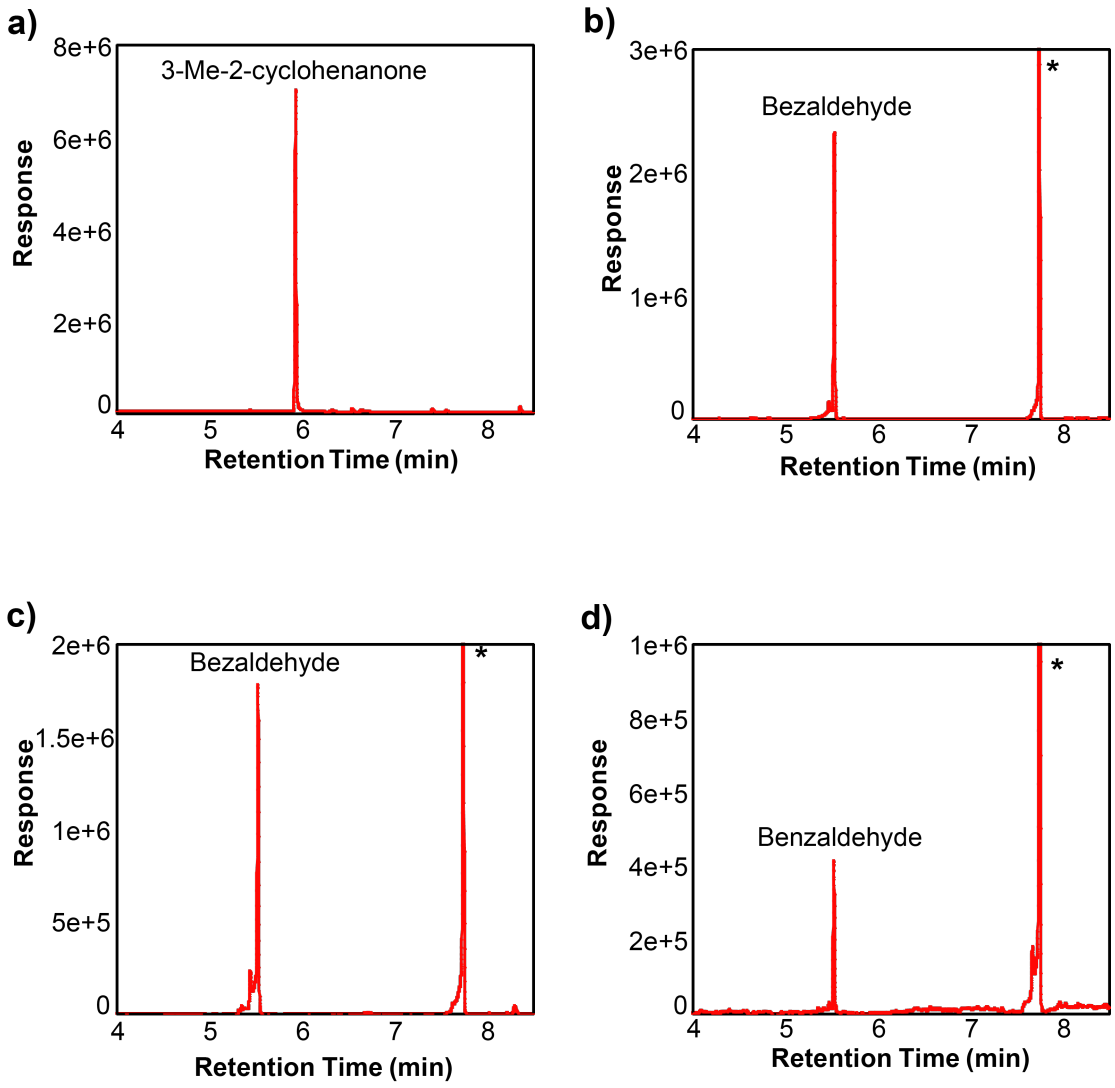

Figure 3. GC-FID analysis of transfer hydrogenation reaction of a) 3-methyl-2-cyclohexenone in ^{i}PrOH/MeOH (4:1) in presence of 0.5 equiv. KOH at 100°C with **Co3** (1 mol%, 360 μM) b) benzaldehyde in H_2O/acetonitrile (4:1) at 40°C in presence of 3 equiv. of sodium formate with **Co3** (2 mol%, 100 μM) c) benzaldehyde in H_2O/acetonitrile (4:1) at 40°C in presence of 3 equiv. of sodium formate with **Co3** (8 mol%, 400 μM) d) benzaldehyde in H_2O/acetonitrile (4:1) at 40°C in presence of 3 equiv. of sodium formate with **Co4** (2 mol%, 100 μM) (* internal standard biphenyl).

4.4.5. General Procedure for Acceptorless Dehydrogenation of Secondary Alcohol by Co3 and Co4 (GC Yield)

The appropriate volumes of the following stock solutions were combined in a 20 mL scintillation vial: alcohol, and [**Co**]. The mixture was then diluted with the desired solvent. The reaction vial was tightly sealed with a screw cap and allowed to proceed at 40°C. After allotted time of reaction, the solution was then filtered through a pipette plug containing celite and the sample was analyzed by GC.

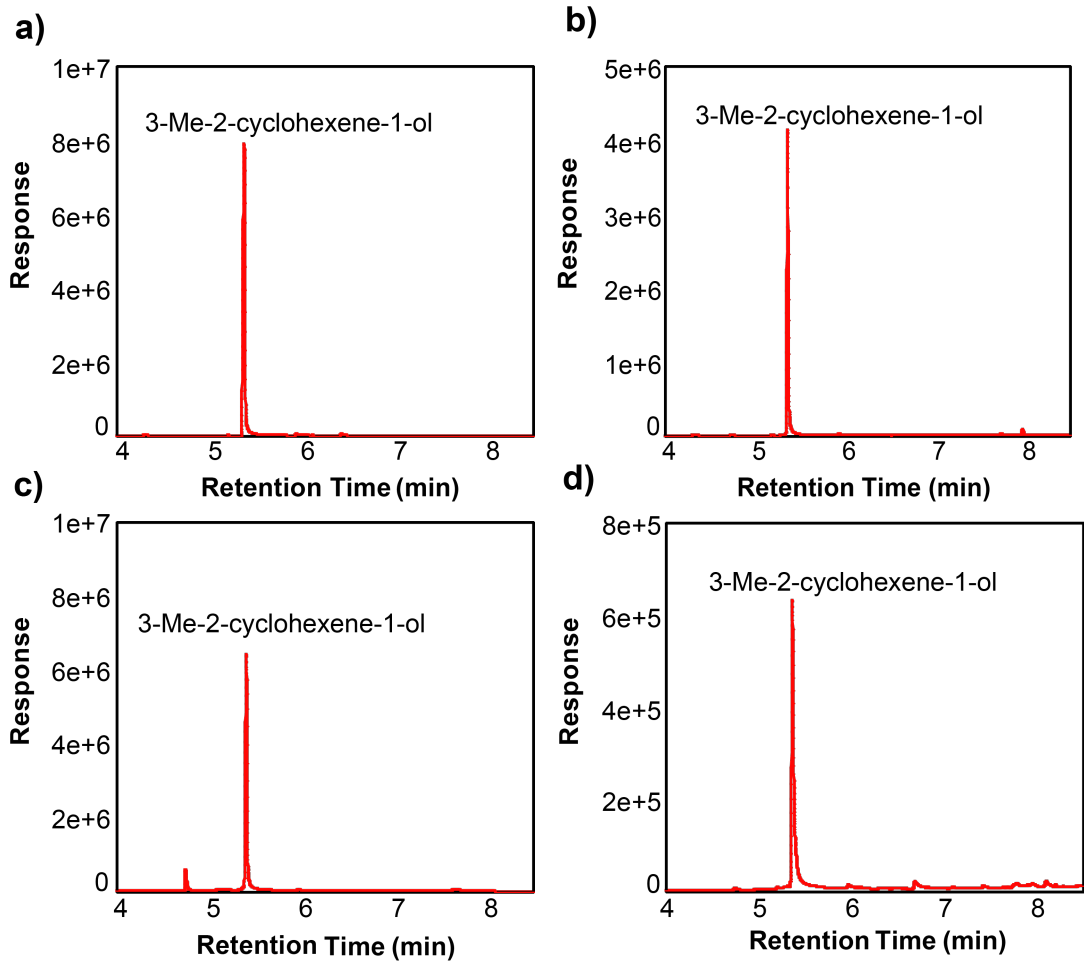

Figure 4. GC-FID analysis of acceptorless dehydrogenation reaction of 3-methyl-2-cyclohexene-1-ol at 40°C a) with 10 mol% **Co3** in acetone b) with 2 mol% **Co4** (1.78 mM) in acetone c) with 2 mol% **Co4** (1.78 mM) in 100% water, c) with 2 mol% **Co4** (1.78 mM) in $H_2O/^tBuOH$ (1:1). (* internal standard biphenyl).

4.4.6. Transfer Hydrogenation of Pr1 by Ir1 in Presence of NADH (GC Yield)

Pr1 (0.30 mL from 5.0 mM stock in ^{t}BuOH/H_2O (12:1), 1.5 μmol, 1.0 equiv.), NADH (2.3 mg, 3.0 μmol, 2.0 equiv.), and iridium catalyst **Ir1** (6.0 μL from 5.0 mM stock solution in ^{t}BuOH/H_2O (4:1), 0.03 μmol, 2 mol%.) were combined in total 1.5 mL of ^{t}BuOH/H_2O (2:3) in a 20 mL scintillation vial. The final concentration of the **Ir1** was 20 μM. The vial was sealed with a screw cap and the reaction mixture was stirred at 40°C for 20 h. After 20 h, 5 mL of water added to the reaction, the organic products were extracted into DCM. The organic layer was separated, dried over Na_2SO_4, filtered, and then evaporated to dryness under vacuum. The reaction products were then analyzed by GC-MS with biphenyl as internal standard.

4.4.7. Calibration Curve for Using Fluorescence Spectroscopy

Solid **Pr2** was pre-dissolved in 2.15 mL of ^{t}BuOH/DMSO (13:1) to give a 5 mM stock solution and then diluted using ^{t}BuOH/H2O (1:4) to give a series of different concentrations (5, 10, 15, 20, 25, 30, 35, 40 μM). The integrated fluorescence at 490–650 nm for the diluted solutions was measured (λ_{ex} = 480 nm). Integrated fluorescence at 490–650 nm was plotted against concentration. The curve was fit a single exponential function.

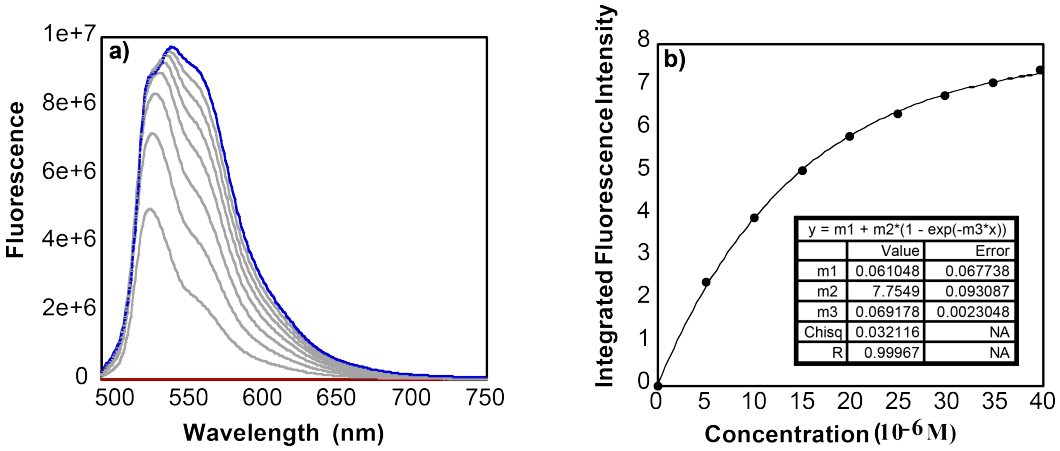

Figure 5. a) Fluorescence spectra (λ_{ex} = 480 nm) of **Pr2** at different concentration (5, 10, 15, 20, 25, 30, 35, 40 µM); 0 µM (red trace) to 40 µM (blue trace) b) Integrated fluorescence at 490–650 nm (λ_{ex} = 480 nm) for **Pr2** solutions were plotted against concentration. The curve was fit into a single exponential rise.

4.4.8. Procedure for Fluorescence Studies in the Cuvette

A stock solution containing 30 µM of **Pr1** and 100 µM of NADH was prepared in ^{t}BuOH/H_2O (1:4). A 3.0 mL aliquot of this solution was transferred to a quartz cuvette and the initial fluorescence spectrum was recorded at RT. An appropriate volume of 5 mM iridium catalyst/iridium salt in ^{t}BuOH/H_2O (4:1) was added to the cuvette to yield the desired iridium catalyst/ iridium salt concentration. This solution was left unstirred at RT under air and the fluorescence spectra were recorded every fifteen minutes for the first hour and then every hour for an additional four hours.

4.4.9. Cell Cytotoxicity Studies

NIH-3T3 mouse fibroblast cells (10000 cells/well) were seeded in a 96-well plate and allowed to attach overnight in a 5% CO_2 humidified incubator. Solid **Pr2** was pre-dissolved in 1.5 mL of DMSO to give a 5 mM stock solution and then diluted using commercial cell growth media (Dulbecco's Modified Eagle Medium (DMEM) supplemented with 5% fetal bovine serum (FBS) and 1% antibiotic (100×)) to give a

series of different concentrations (0.1, 1, 25, 50, 100, and 250 μM). The cells were then treated with the **Pr2** solutions (6 wells per concentration) for 3 h. The solutions were removed by pipette and the cells were washed with fresh DMEM twice before adding DMEM containing 3-(4,5-dimethylthiazol-2-yl)-5-(3-carboxymethoxyphenyl)-2-(4-sulfophenyl)-2H-tetrazolium (MTS) (2 mL MTS/8 mL DMEM). After 2 h, the absorbance of the 96-well plate was measured at 495 nm to determine the amount of purple formazan complex formed. Cell viability was considered to be proportional to the absorbance of the wells. The absorbance value of the wells containing solutions of MTS (background) was subtracted from those of the wells containing treated and control cells. Percentage cell viability was calculated using the following equation: $(A_{conc}/A_{control})\times 100\%$, where A_{conc} is the absorbance at a specific probe concentration and $A_{control}$ is the absorbance of the untreated cells sample. The cell viability data were fit to a single exponential decay function and the IC_{50} value was extracted from this fit at 50% cell viability.

4.4.10. Fluorescence Analysis of Lysate from Cell Experiments

NIH-3T3 cells were cultured in 100 mm tissue culture plates (Corning) at 37°C under a 5% CO_2 humidified atmosphere and allowed to reach 100% confluence. Cells were treated with appropriate concentration of **Pr1** (diluted from 5 mM stock solution in DMSO) for allotted time in DMEM. After incubation with **Pr1** (37 °C, 5% CO_2), the solutions were removed and the adhered cells were rinsed twice with DMEM. A solution containing appropriate amount of complex **Ir1** (diluted from 5 mM stock solution in DMSO) was added. After a 2 h incubation period, the cell growth media were removed and the adhered cells were washed once with DMEM followed by detachment using

trypsin. The cell density was determined by treating the cells with Trypan Blue and then counted using a BIO-RAD TC10 automated cell counter. Finally, the cells were washed with PBS, centrifuged, and then the supernatant was removed by pipette. A 1.0 mL solution of ice-cold water/acetonitrile/methanol (1:2:2) was added to the cell pellets. The cell suspension was transferred to a glass autosampler vial and vortex for 5 min. The samples were snap frozen by immersing in liquid nitrogen and then thawing to RT (3 times per sample). Each sample was transferred to a 1.5 mL centrifuge tube and centrifuged at 16000 xg for 15 min at 4°C. A 500 µL solution of the supernatant was collected and diluted to a total volume of 3.0 mL with water/acetonitrile/methanol (1:2:2). The integrated fluorescence at 490-650 nm for the diluted lysate solution was measured (λ_{ex} = 480 nm).

4.4.11. Fluorescence Analysis of Lysate from Control Experiments

NIH-3T3 cells were cultured in 100 mm tissue culture plates (Corning) at 37°C under a 5% CO_2 humidified atmosphere and allowed to reach 100% confluence. Cells were treated with 30 µM concentration of **Pr2** (diluted from 5 mM stock solution in DMSO) for 4 h in DMEM. After 4 h of incubation (37 °C, 5% CO_2), the solutions were removed and the adhered cells were rinsed twice with DMEM. A solution containing 2 µM DMSO was added. After a 2 h incubation period, the cell growth media were removed and the adhered cells were washed once with DMEM followed by detachment using trypsin. The cell density was determined by treating the cells with Trypan Blue and then counted using a BIO-RAD TC10 automated cell counter. Finally, the cells were washed with PBS, centrifuged, and then the supernatant was removed by pipette. A 1.0 mL solution of ice-cold water/acetonitrile/methanol (1:2:2) was added to the cell pellets. The cell

suspension was transferred to a glass autosampler vial and vortex for 5 min. The samples were snap frozen by immersing in liquid nitrogen and then thawing to RT (3 times per sample). Each sample was transferred to a 1.5 mL centrifuge tube and centrifuged at 16000 xg for 15 min at 4°C. A 500 µL solution of the supernatant was collected and diluted to a total volume of 3.0 mL with water/acetonitrile/methanol (1:2:2). The integrated fluorescence at 490-650 nm for the diluted lysate solution was measured (λ_{ex} = 480 nm).

4.4.12. Cellular Uptake of Pr2

NIH-3T3/A549 cells were cultured in 100 mm tissue culture plates (Corning) at 37°C under a 5% CO_2 humidified atmosphere and allowed to reach 100% confluence. Cells were treated with 10 mL of 100 µM/200 µM of **Pr2** for NIH3T3 and with 100 µM of **Pr2** for A549 (**Pr2** diluted from 5 mM stock solution in DMSO) for 2 h in DMEM. After 2 h of incubation (37 °C, 5% CO_2), the solutions were removed and the adhered cells were rinsed twice with DMEM. The adhered cells were detached using trypsin. The cells were washed with PBS, centrifuged, and then the supernatant was removed by pipette. A 1.0 mL solution of ice-cold water/acetonitrile/methanol (1:2:2) was added to the cell pellets. The cell suspension was transferred to a glass autosampler vial and vortex for 5 min. The samples were snap frozen by immersing in liquid nitrogen and then thawing to RT (3 times per sample). Each sample was transferred to a 1.5 mL centrifuge tube and centrifuged at 16000 xg for 15 min at 4°C. A 500 µL solution of the supernatant was collected and diluted to a total volume of 3.0 mL with water/acetonitrile/methanol (1:2:2). The integrated fluorescence at 490-650 nm for the diluted lysate solution was measured (λ_{ex} = 480 nm). Concentration of **Pr2** in diluted lysate solution was calculated

from the calibration curve. Concentration of **Pr2** in lysate solution was calculated using dilution correction.

[**Pr2**] in lysate = ([**Pr2**] in diluted lysate × 3000) / 500

% of Cellular uptake was calculated using: [(mols of **Pr2** extracted in cell lysate) ÷ (Total mols of **Pr2** used for incubation)] × 100

For example, Total μmols of **Pr2** used for 10 mL 100 μM incubation = (100 × 10) ÷ 1000 = 1 μmol

μmols of **Pr2** extracted in cell lysate = ([**Pr2**] in lysate in μM ÷1000)

4.4.13. Cellular Retention of Pr2

NIH-3T3/A549 cells were cultured in 100 mm tissue culture plates (Corning) at 37°C under a 5% CO_2 humidified atmosphere and allowed to reach 100% confluence. Cells were treated with 10 mL of 100 μM of **Pr2 (**diluted from 5 mM stock solution in DMSO) for 2 h in DMEM. After 2 h of incubation (37 °C, 5% CO_2), the solutions were removed and the adhered cells were rinsed twice with DMEM. 5 mL fresh DMEM was added to the culture plate. DMEM was collected after 30 min and another 5 mL of fresh DMEM was added to the culture plate. Same step was repeated for 2 h in every 30 min. The integrated fluorescence at 490–650 nm for the 5 mL DMEM collected every 30 min after incubation was measured (λ_{ex} = 480 nm). Concentration of **Pr2** in DMEM was calculated from the calibration curve.

μmols of **Pr2** in DMEM = [([**Pr2**] in DMEM in μM ÷1000) ×5]

4.5. References

1. Noffke, A. N.; Habtemariam, A.; Pizarro, A. M.; Sadler, P. J. *Chem. Comm.* **2012**, *48*, 5219-5246.
2. Zhe Liu, Z.; and Peter J. Sadler, P. J. *Acc. Chem. Res*. **2014**, *47*, 1174-1185.
3. Jefferson Lab. It's Elemental: The Periodic Table of Elements. https://education.jlab.org/itselemental/ (accessed May 31st, 2019).
4. Chirik, P. J. *Acc. Chem. Res.* **2015**, *48*, 1687-1695.
5. Li, Y.-Y.; Yu, S.-L.; Shen, W.-Y.; Gao, J.-X. *Acc. Chem. Res.* **2015**, *48*, 2587-2598.
6. Gao, K.; Yoshikai, N. *Acc. Chem. Res.* **2014**, *47*, 1208-1219.
7. Filonenko, G. A.; Van Putten, R.; Hensen, E. J. M.; Pidko, E. A. *Chem. Soc. Rev*. **2018**, *47*, 1459-1483.
8. Sun, J.; Deng, L. *ACS Catal.* **2016**, *6*, 290-300.
9. Du, X.; Huang, Z. *ACS Catal*. **2017**, *7*, 1227-1243.
10. Obligacion, J. V.; Chirik, P. J. *Nat. Rev. Chem*. **2018**, *2*, 15-34.
11. Zuo, Z.; Wen, H.; Liu, G.; Huang, Z. *Synlett* **2018**, *29*, 1421-1429.
12. Chen, J.; Lu, Z. *Org. Chem. Front.* **2018**, *5*, 260-272.
13. Banerjee, R. *Chemistry and Biochemistry of B12* 1999, Wiley, New York, NY.
14. Brown, K. L. *Chem. Rev.* **2005**, *105*, 2075-2150.
15. a) Tsitovich, P. B.; Cox, J. M.; Benedict, J. B.; Morrow, J. R. *Inorg. Chem*. **2016**, *55*, 700–716. b) Yu, M.; Xie, D.; Phan, K. P.; Enriquez, J. S.; Luci, J. J.; Que, E. L. *Chem. Comm*. **2016**, *52*, 13885-13888.
16. a) Ware, D. C.; Palmer, B. D.; Wilson, W. R.; Denny, W. A. *J. Med. Chem*. **1993**, *36*, 1839-1846. b) Ware, D. C.; Palmer, H. R.; Pruijn, F. B.; Anderson, R. F.; Brothers, P. J.; Denny, W. A.; Wilson, W. R. *Anti-Cancer Drug Des*. **1998**, *13*, 81-103. c) Yamamoto, N.; Renfrew, A. K.; Kim, B. J.; Bryce, N. S.; Hambley, T. W. *J. Med. Chem*. **2012**, *55*, 11013-11021. d) Karnthaler-Benbakka, C.; Groza, D.; Kryeziu, K.; Pichler, V.; Roller, A.; Berger, W.; Heffeter, P.; Kowol, C. R. *Angew. Chem. Int. Ed*. **2014**, *53*, 12930-12935. e) Renfrew, A. K.; Bryce, N. S.; Hambley, T. *Chem. - Eur. J.* **2015**, *21*, 15224-15234. f) de Souza, I. C. A.; Faro, L. V.; Pinheiro, C. B.; Gonzaga, D. T. G.; de C. da Silva, F.; Ferreira, V. F.; da S. Miranda, F.; M. Scarpellini, M.; Lanznaster, M. *Dalton Trans.* **2016**, *45*, 13671-13674. g) King, A. P.; Gellineau, H. A.; Ahn, J. -E.; MacMillan, S. N.; Wilson, J. J. *Inorg. Chem.* **2017**, *56*, 6609–6623. h)

O'Neill, E. S.; Kaur, A.; Bishop, D. P.; Shishmarev, D.; Kuchel, P. W.; Grieve, S. M.; Figtree, G. A.; Renfrew, A. K.; Bonnitcha, P. D.; New, E. J. *Inorg. Chem*. **2017**, *56*, 9860-9868.

17. a) Schmidt, K.; Jung, M.; Keilitz, R.; Schnurr, B.; Gust, R. *Inorg. Chim. Acta* **2000**, *306*, 6-16. b) Ott, I.; Schmidt, K.; Kircher, B.; Schumacher, P.; Wiglenda, T.; Gust, R. J. *Med. Chem.* **2005**, *48*, 622-629. c) Gust, R.; Ott, I.; Posselt, D.; Sommer, K. *J. Med. Chem*. **2004**, *47*, 5837-5846. d) Saghatforoush, L.; Moeini, K.; Hosseini-Yazdi, S. A.; Mardani, Z.; Hajabbas-Farshchi, A.; Jameson, H. T.; Telfer, S. G.; Woollins, J. D. *RSC Adv.* **2018**, *8*, 35625-35639. e) Smolko, L.; Černák, J.; Kuchár, J.; Sabolová, D.; Boča, R. *Chem. Pap*. **2018**, *72*, 877-882.

18. a) Böttcher, A.; Takeuchi, T.; Hardcastle, K. I.; Meade, T. J.; Gray, H. B.; Cwikel, D.; Kapon, M.; Dori, Z. Inorg. Chem., 1997, 36, 2498-2504. b) Takeuchi, T.; Böttcher, A.; Quezada, C. M.; Simon, M. I.; Meade, T. J.; Gray, H. B. *J. Am. Chem. Soc.* **1998**, *120*, 8555-8556. c) Harney, A. S.; Lee, J.; Manus, L. M.; Wang, P.; Ballweg, D. M.; LaBonne, C.; Meade, T. *J. Proc. Natl. Acad. Sci. U. S. A.* **2009**, *106*, 13667-13672. d) Tomco, D.; Schmitt, S.; Ksebati, B.; Heeg, M. J.; Dou, Q. P.; Verani, C. N. *J. Inorg. Biochem.* **2011**, *105*, 1759-1766. e) Hurtado, R. R.; Harney, A. S.; Heffern, M. C.; Holbrook, R. J.; Holmgren, R. A.; Meade, T. J. *Mol. Pharm.* **2012**, *9*, 325-333. f) Verani, C. N. *J. Inorg. Biochem.* **2012**, *106*, 59-67. g) Heffern, M. C.; Kurutz, J. W.; Meade, T. J. *Chem. - Eur. J.* **2013**, *19*, 17043-17053 h) Pierroz, V.; Joshi, T.; Leonidova, A.; Mari, C.; Schur, J.; Ott, I.; Spiccia, L.; Ferrari, S.; Gasser, G. *J. Am. Chem. Soc.* **2012**, *134*, 20376-20387. i) Peterson, M. D.; Holbrook, R. J.; Meade, T. J.; Weiss, E. A. *J. Am. Chem. Soc.* **2013**, *135*, 13162-13167. j) Holbrook, R. J.; Weinberg, D. J.; Peterson, M. D.; Weiss, E. A.; Meade, T. J. *J. Am. Chem. Soc.* **2015**, *137*, 3379-3385.

19. a) Asbell, P. A.; Epstein, S. P.; Wallace, J. A.; Epstein, D.; Stewart, C. C.; Burger, R. M. *Cornea* **1998**, *17*, 550-557. b) Burger, R. M.; Stewart, C. C.; Winicov, I.; Bourne, N.; Stanberry, L. R.; Bonnez, W.; Weislow, O. S. *AIDS* **2001**, *15*, 1. c) Schwartz, J. A.; Lium, E. K.; Silverstein, S. J. *J. Virol*. **2001**, *75*, 4117-4128. d) Epstein, S. P.; Pashinsky, Y. Y.; Gershon, D.; Winicov, I.; Srivilasa, C.; Kristic, K. J.; Asbell, P. A. *BMC Ophthalmol*. **2006**, *6*, 1-14.

20. Halle, R.; Bréhéret, A.; Schulz, E.; Pinel, C.; Lemaire, M. *Tetra: Asym.* **1997**, *8*, 2101-2108.

21. Zhang, G.; Hanson, S. K. *Chem. Comm*. **2013**, *49*, 10151-10153.

22. Zhang, G.; Hanson, S. K. *Org. Lett.* **2013**, *15*, 650-653.

23. Loudet, A.; Burgess, K. *Chem. Rev*. **2007**, *107*, 4891-4932.

24. Boens, N.; Leen, V.; Dehaen, W. *Chem. Soc. Rev.* **2012**, *41*, 1130-1172.

25. Lu, H.; Mack, J.; Yang, Y.; Shen, Z. *Chem. Soc. Rev*. **2014**, *43*, 4778-4823.

26. a) Zimmermann, K. H.; Pilato, R. S.; Horvath, I. T.; Okuda, J. *Organometallics* **1992**, *11*, 3935-3937. b) Nesmeyanov, A. N.; Rybinskaya, M. I.; Krivykh, V. V.; Kaganovich, V. S. *J. Organomet. Chem.* **1975**, *93*, C8-C10.

27. a) Nesmeyanov, A. N.; Krivykh, V. V.; Rybinskaya, M. I.; *J. Organomet. Chem.* **1979**, *164*, 159-165. b) Nesmeyanov, A. N.; Krivykh, V. V.; Panosyan, G. A.; Retrovskh, P. V.; Rybinskaya, M. I. *J. Organomet. Chem.* **1979**, *164*, 167-175. c) Nesmeyanov, A. N.; Struchkov, Y. T.; Andrianov, V. G.; Krivykh, V. V.; Rybinskaya, M. I. *J. Organomet. Chem.* **1979**, *166*, 211-215.

28. Yeh, P. –H.; Pang, Z.; Johnston, R. F. *J. Organomet. Chem.* **1996**, *509*, 123-129.

29. Jutzi, P.; Kristen, M. O.; Dahlhaus, J.; Neumann, B.; Stammler, H. –G. *Organometallics* **1993**, *12*, 2980-2985.

30. Li, L.; Han, S.; Li, Q.; Chen, Z.; Pang, Z. *Eur. J. Inorg. Chem.* **2007**, *32*, 5127-5137.

31. Krumova, K.; Cosa, G. *J. Am. Chem. Soc.* **2010**, *132*, 17560-17569.

32. Zhu, H.; Fan, J.; Li, M.; Cao,. J.; Wang, J.; Peng, X. *Chem. Eur. J.* **2014**, *20*, 4691-4696.

33. Nadres, E. T.; Daugulis, O. *J. Am. Chem. Soc.* **2012**, *134,* 7-10.

34. Frith S. A.; Spencer, J. L. *Inorg. Synth*. **1990**, *28*, 273-280.

35. Almodares, Z.; Lucas, S. J.; Crossley, B. D.; Basri, A. M.; Pask, C. M.; Hebden, A. J.; Phillips, R. M.; McGowan, P. C. *Inorg. Chem.* **2014**, *53*, 727-736.

36. Kang, J. W.; Moseley, K.; Maitlis, P. M. *J. Am. Chem. Soc.* **1969**, *91*, 5970-5977.

Chapter 4 Appendix

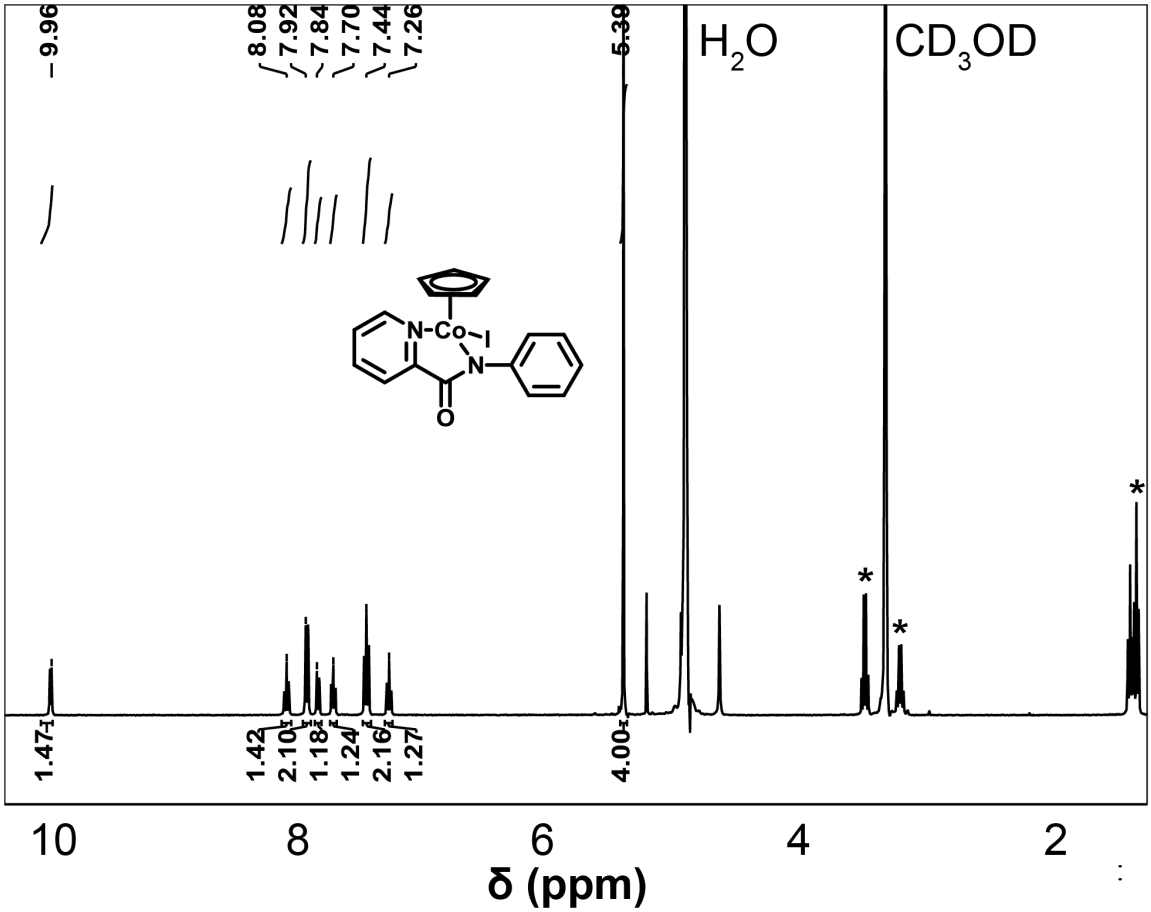

Figure S1. ^{1}H NMR spectrum (400 MHz, CD_3OD) of compound **Co3** (* solvent impurities).

- Vertical axis represents the abundance.

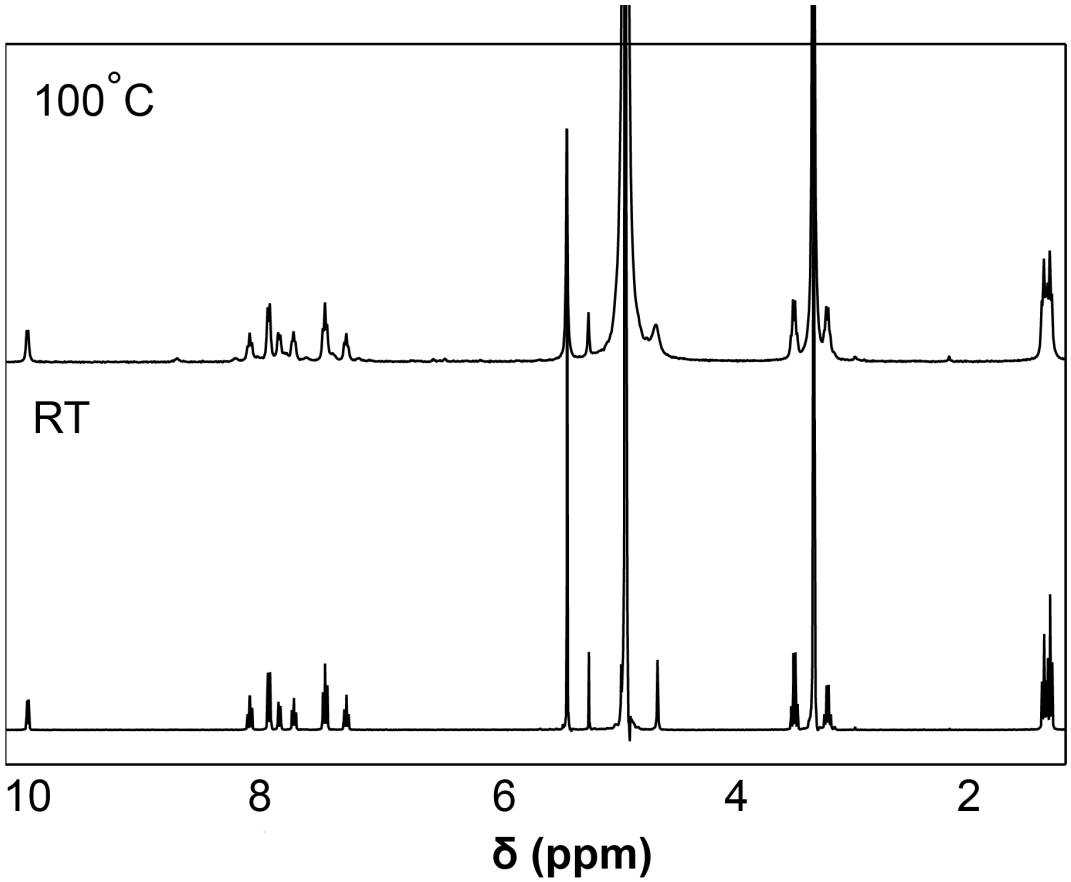

Figure S2. ^{1}H NMR spectrum (400 MHz, CD_3OD) of compound **Co3** at room temperature (RT) and at 100°C.